CONTACT LAWS FOR LARGE DEFORMATION UNCONFINED AND CONFINED COMPRESSION OF SPHERICAL PLASTIC PARTICLES WITH POWER-LAW HARDENING

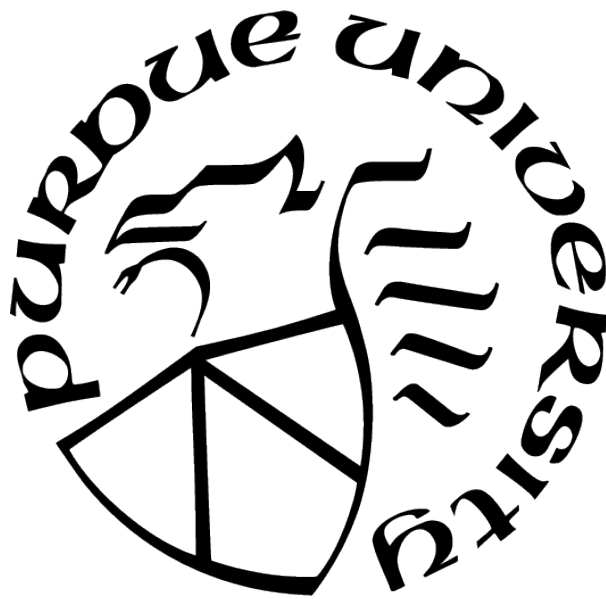by

Muhammad B. Shahin

A Thesis

Submitted to the Faculty of Purdue University

In Partial Fulfillment of the Requirements for the degree of

Master of Science

School of Mechanical Engineering

West Lafayette, Indiana

May 2021

THE PURDUE UNIVERSITY GRADUATE SCHOOL
STATEMENT OF COMMITTEE APPROVAL

Dr. Marcial Gonzalez, Chair

School of Mechanical Engineering

Dr. Carl Wassgren

School of Mechanical Engineering

Dr. Adrian Buganza Tepole

School of Mechanical Engineering

Approved by:

Dr. Nicole Key

To my beloved family

ACKNOWLEDGMENTS

First and foremost, I would like to thank my advisor, Professor Marcial Gonzalez, for his support and encouragement throughout my research work. I am thankful for the undergraduate research opportunity he provided me which gave me the insight I needed to make the decision of pursuing graduate school. I will forever be grateful for the amazing opportunities he provided me. He has been a very motivational advisor and I look forward to continue working alongside him for my PhD.

I would like to thank Professor Carl Wassgren and Professor Adrian Buganza Tepole for serving in my advisory committee and providing feedback to assist me in improving my research work.

A very special thank you to my colleague, Dr. Ankit Agarwal, who helped me tremendously throughout my research work. Thank you for being very patient with me and always willing to help. He took leadership in completing Chapter 2 of this thesis and his leadership was very inspirational.

Finally, I would like to thank my parents for their unconditional love and support. If it was not for their support, I would not be where I am today. I am very thankful to have such wonderful parents that continuously motivate me to do better and pursue my dreams.

TABLE OF CONTENTS

LIST OF TABLES

LIST OF FIGURES

9

ABSTRACT

Confined particulate systems, particularly powder compacts, are widely used in various applications in industries such as pharmaceutical, automotive, agriculture, and energy production. Due to their extensive applications, characterization of these materials is of great importance for optimizing their performance and manufacturing processes. Modeling approaches capable of capturing the heterogeneity and complex behavior are effective at predicting the macroscopic behavior of granular systems. These modeling approaches utilize information about the microstructure evolution of these materials during compaction processes at the mesoscale (particle-scale). Using these types of modeling depend on accurate contact formulation between inter-particle contacts. The challenge comes in formulating these contact models that accurately predict force-area-deformation relationships. In this work, contact laws are presented for elastic-ideally plastic particles and plastic particles with power-law hardening under unconfined (simple compression) and confined (die and hydrostatic compaction) compression. First, material properties for a set of finite element simulations are obtained using space-filling design. The finite element simulations are used for verification and building an analytical framework of the contact radius and contact pressure which allows for efficient determination of the contact force. Semi-mechanistic contact laws are built for elastic-ideally plastic spherical particles that depend on material properties and loading configuration. Then, rigid-plastic assumption is used to modify the contact laws to consider power-law hardening effects while keeping loading configuration dependency. Finally, after building and verifying the contact laws, they are used to estimate hardening properties, contact radius evolution, and stress response of micro-crystalline cellulose particles under different loading configurations using experimental data from simple compression.

1. INTRODUCTION

1.1 Motivation

Confined particulate systems have a wide range of applications in many industries such as pharmaceutical, automotice, agriciulture, ceramic, construction, and energy production. The applicability of these materials makes them of great interest in research, particularly predicting and modeling the mesoscopic and macroscopic behavior under confinement. Developing these predictive models allows for more efficient manufacturing processes and the optimization of performance in all applications.

1.2 Background

Confined granular systems and powder compacts experience heterogenous behavior (Majmudar & Behringer, 2005) which greatly affects their macroscopic behavior. Mechanistic continuum modeling, on a macroscopic scale, has proved to be capable of describing microstructure evolution during powder compaction (Puri, Tripodi, Manbeck, and Messing, 1995; Sun and Kim, 1997, Chtourou, Guillot, and Gakwaya, 2002, Cunningham, Sinka, and Zavaliangos, 2004; DiMaggio and Sandler, 1971; Han et al., 2008; Sinha, Curtis, Hancock, and Wassgren, 2010; Sinka, Cunningham, and Zavaliangos, 2004, and A. Bakhshiani, Khoei, and Mofid, 2004, 2002; Khoei, Mofid, and Bakhshiani, 2002). The issue with these models is they consider the materials to be homogeneous, negelecting crucial behavior present at the mesoscale (or particle-scale). A dynamic modeling approach called Discrete Element Method (DEM) can accurately predict behavior at the mesoscale during compaction (Belheine, Plassiard, Donzé, Darve, and Seridi, 2009; Harthong, Jérier, Dorémus, Imbault, and Donzé, 2009; Jerier et al., 2011; C.L. Martin and Bouvard, 2003; C.L Martin, Bouvard, and Shima, 2003; C. L. Martin, Bouvard, and Delette, 2006; Rojek et al., 2016; Sheng, Lawrence, Briscoe, and Thornton, 2002; Skrinjar and Larsson, 2004). Recently, another discrete modeling approach called discrete particle mechanics (M. Gonzalez and Cuitiño, 2016; Marcial Gonzalez, 2019; Marcial Gonzalez, Poorsolhjouy, Thomas, Liu, and Balakrishnan, 2018; Poorsolhjouy and Gonzalez, 2018; Yohannes et al., 2016, 2017) has been proposed that is more computationally

efficient. Because discrete modeling considers the significant heterogeity of the materials, it is the superior method for predicting behavior of powder compacts. The use of discrete modeling requires the development of contact formulation between inter-particles contacts. These contact formulations describe the force-area-deformation relationship of the particles during confinement.

1.3   Research Goals

As mentioned in the previous section, the use of discrete modeling requires the development of contact formulation. For discrete modeling to be effective, the contact formulation must accurately determine force-area-deformation relationships during compaction. Contact laws have been proposed for elasto-plastic spheres assuming rigid-plastic power-law (Biwa & Storåkers, 1995; Tabor, 1951) and contact of inelastic solids of revolution (B. Storåkers, Biwa, & Larsson, 1997). These contact models are only effective at small deformations and are unable to capture complex behavior such as softening and confinement effects at large deformations. There has been contact models that are predictive for small-moderate-large deformations (Frenning, 2013, 2015; Harthong et al., 2009; Harthong et al., 2012; E. Olsson and Larsson, 2016; Erik Olsson and Larsson, 2013a, 2013b, however, these contact models lack consistent loading condition dependency, prediction of contact radius, or wide range of material properties.

Finding predictive mechanistic contact formulation for large deformation contact behavior of elasto-plastic particles under general loading conditions remains an issue. In this thesis, efforts are made towards the development of such contact formulation. In chapter 2 (Agarwal, Shahin, & Gonzalez, 2021), a semi-mechanistic contact law for elastic-ideally plastic spherical particles under confined and unconfined loading configurations is introduced. In chapter 3 (Shahin, Agarwal, & Gonzalez, 2021), the contact law is extended to capture power-law hardening behavior of plastic spherical particles. Both contact laws are verified using finite element simulations. Finally, in chapter 4, concluding remarks and future work are presented.

2. SEMI-MECHANISTIC CONTACT LAW FOR LARGE DEFORMATION UNCONFINED AND CONFINED COMPRESSION OF ELASTO-PLASTIC PARTICLES

The content of this chapter and associated appendices A, B, C, and D will be submitted to Journal of the Mechanics and Physics of Solids.

2.1 Introduction

Compacted granular systems, particularly powder compacts, are one of the most commonly used types of materials, with extensive applications in manufacturing processes of critical industries like pharmaceuticals, ceramics, energy, automotive, construction, food, and metallurgy. The versatility and wide application of these materials have made them a subject of active research in the scientific community, particularly in the area of predictive modeling of meso and macroscopic behavior of these materials under confinement. In these applications, confined granular media typically consist of a disordered blend of powder particles with different properties and size distributions. During compaction, these particles deform by coming into contact with neighboring particles as forces get transmitted throughout the system, essentially forming a heterogeneous contact network of force chains (Majmudar & Behringer, 2005). The significant heterogeneity of these systems at the granular scale has, therefore, a fundamental impact on their macroscopic behavior.

Conventionally, the macroscopic behavior of confined granular systems has been described by continuum models, such as Cam-Clay (Puri et al., 1995; Sun & Kim, 1997), Cap (Chtourou et al., 2002), Drucker-Prager Cap (DPC) (Cunningham et al., 2004; DiMaggio & Sandler, 1971; Han et al., 2008; Sinha et al., 2010; Sinka et al., 2004), and endochronic (A. Bakhshiani et al., 2004, 2002; Khoei et al., 2002) plasticity models, which consider granular media as homogeneous materials, thereby neglecting the critical behavior at meso-scale (or particle-scale), such as particle rearrangement and non-affine deformations. More recently, macroscopic discrete models have been proposed. The capability of these models to incorporate microstructural evolution and properties of the granular system into its global behavior has increased their popularity and usage in recent years. A commonly used numerical method in this category

is the Discrete Element Method (DEM) proposed by (Cundall & Strack, 1979), which is a dynamic modeling approach that has been employed extensively to successfully study and predict densification due to particle rearrangement and particle-particle elasto-plastic deformation during powder compaction (Belheine et al., 2009; Harthong et al., 2009; Jerier et al., 2011; C.L. Martin & Bouvard, 2003; C.L Martin et al., 2003; C. L. Martin et al., 2006; Rojek et al., 2016; Sheng et al., 2002; Skrinjar & Larsson, 2004). The discrete particle mechanics approach (M. Gonzalez & Cuitiño, 2016; Marcial Gonzalez, 2019; Marcial Gonzalez et al., 2018; Poorsolhjouy & Gonzalez, 2018; Yohannes et al., 2016, 2017) is another computationally efficient numerical technique for modeling of highly confined granular systems. This approach models the compaction process as a sequence of quasi-static loading steps, where a set of nonlinear equations for the equilibrium configuration of each particle is formulated and solved during each loading step, thus avoiding the limitations imposed on the time step by the conditional stability of any time integration scheme used in DEM.

While the superiority of discrete models over continuum models in describing the macroscopic behavior of confined granular systems is evident, it is worth mentioning that the predictability of discrete models relies heavily on the employed contact formulation to describe the contact force-area-deformation relationship between inter-particle contacts formed before and during the compaction process. Understanding the contact mechanics between deformable particles has been a problem of interest for several decades. While contact of elastic particles within the regime of small deformations is fairly understood, thanks to the classical work of (Hertz, 1882), the problem becomes more involved and complex with consideration of large deformations and inelastic material behavior. As an initial step towards formulating an analytical contact law for elasto-plastic particles under large deformations, we attempt to understand the deformation mechanisms that govern the particle response under large compression. Figure 2.1 presents the normalized contact pressure-deformation, contact radius-deformation and contact force-deformation responses derived from finite element (FE) simulations of a single spherical particle, with elasto-plastic von Mises type power-law hardening behavior, under three types of loading configurations in a simple cubic cell, namely simple axial compression, die compression (axial compression and lateral confinement between four rigid walls) and hydrostatic compression (isostatic axisymmetric loading). Schematics of

these loading configurations are depicted in Fig. 2.2. The material's yield surface evolves according to the following power law (Ludwik, 1909)

$$\sigma = \sigma_y + K \epsilon_{\text{pl}}^{1/n} \tag{2.1}$$

where σ is the current stress, σ_y is the yield stress, K is a representative strength, n is the hardening exponent, and ϵ_{pl} is the plastic strain calculated as

$$\epsilon_{\text{pl}} = \epsilon - \frac{\sigma}{E} \tag{2.2}$$

where ϵ is the current strain and E is the Young's modulus. To perform the simulations, material properties corresponding to those reported by (Chen, Imbault, & Dorémus, 2007) for lead were used, i.e., $K = 15.5$ MPa, $n = 2.857$, $E = 10$ GPa and $\nu = 0.435$. To ensure consistency with the assumption of rigid-plastic power law hardening behavior by previous works on contact models for spherical indentation (Biwa & Storåkers, 1995; Tabor, 1951) and contact of inelastic solids of revolution (B. Storåkers et al., 1997), the Hollomon's power law (Hollomon, 1945) is additionally considered

$$\sigma = \kappa \epsilon^{1/m} \tag{2.3}$$

where κ is a representative strength and m is the hardening exponent. By equating power laws given by Eqs. (2.1) and (2.3) and adjusting the coefficient values to obtain similar response curves, (Harthong et al., 2009) obtained $\kappa = 20.5$ MPa and $m = 4.167$ for lead. This value of κ was used to normalize the contact force and the contact pressure in Fig. 2.1.

(a)

(b)

(c)
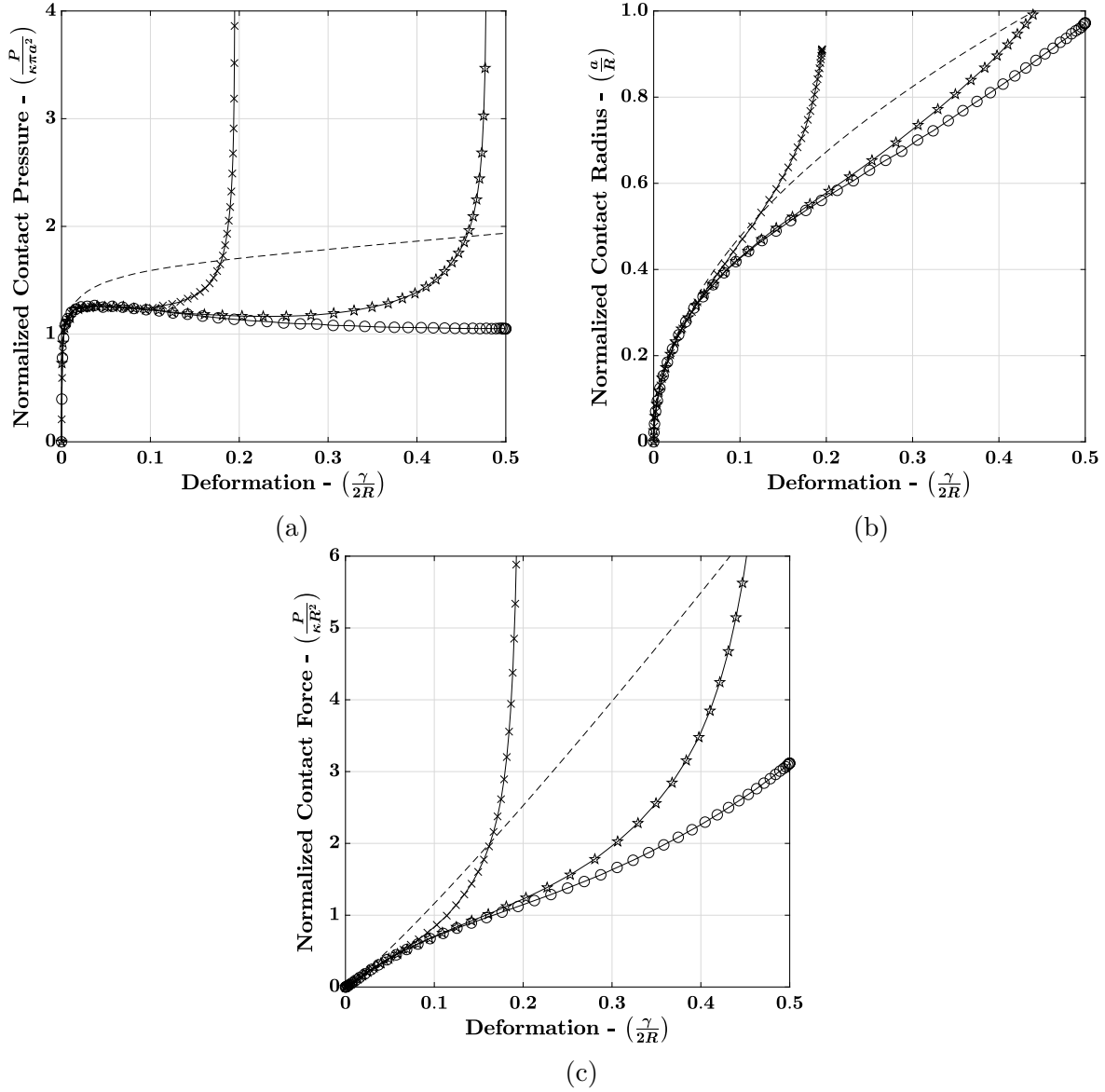
Fig.2.1. Finite element simulation results of normalized (a) contact pressure-deformation, (b) contact radius-deformation, and (c) contact force-deformation behavior of an elastic-plastic power law hardening sphere of radius $R = 10$ mm under three types of loading configurations, namely simple compression (solid curve with circle markers), die compaction (solid curve with pentagram markers) and hydrostatic compaction (solid curve with cross markers). The similarity solution proposed by (Biwa & Storåkers, 1995) is also plotted for comparison, and is shown as dashed curve in all the plots. The material properties used here correspond to lead (Chen, Imbault, & Dorémus, 2007; Harthong, Jérier, Dorémus, Imbault, & Donzé, 2009), with Young's modulus $E = 10$ GPa, Poisson's ratio $\nu = 0.435$, representative strength $\kappa = 20.5$ MPa and hardening exponent $m = 4.167$.

(a) Simple Compression (b) Die Compression (c) Hydrostatic Compression
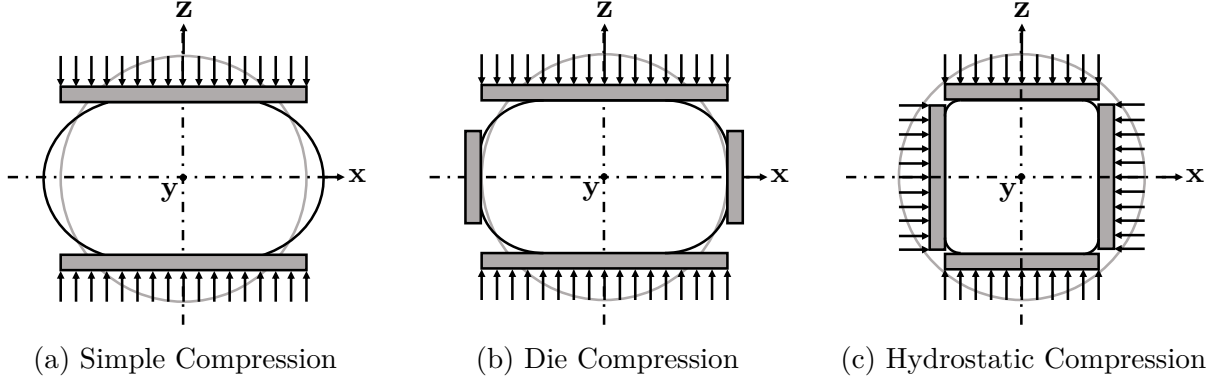
Fig.2.2. Schematics of loading configurations considered in this study.
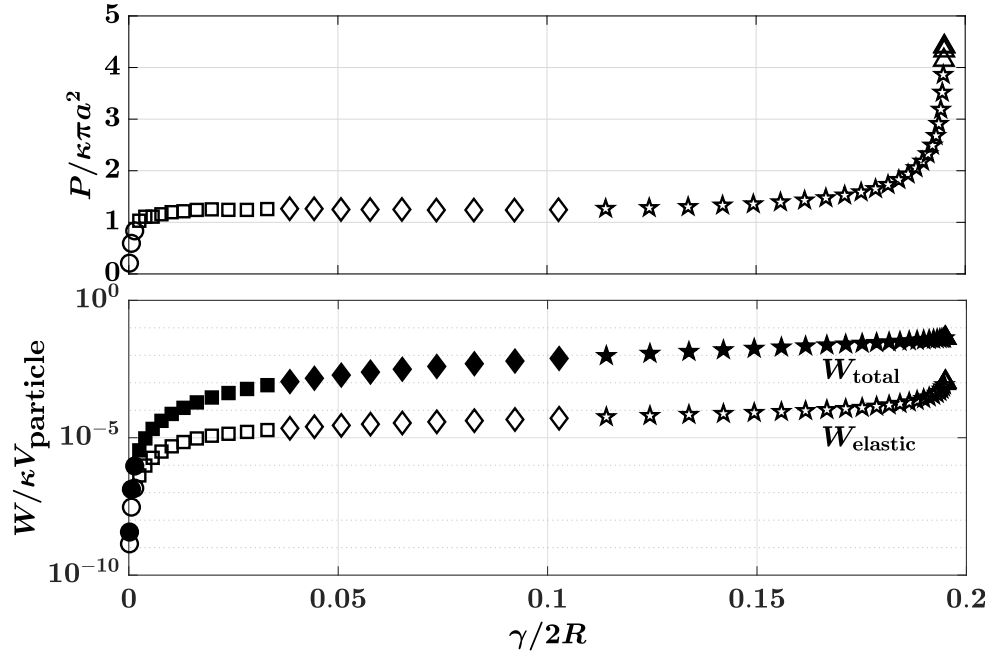
Fig.2.3. Comparison of the evolution of normalized contact pressure (top) with the evolution of normalized energy (bottom) versus deformation during FE simulation of the hydrostatic compaction of a lead sphere. The various deformation stages are depicted by different symbols as follows: elastic ($\bigcirc$), 'contained' or elastic-plastic ($\square$), 'uncontained' or plastic ($\lozenge$), 'low compressibility' ($\star$), and elastic volumetric ($\triangle$) deformations. In the bottom plot, the total work done, W_{total}, is depicted by filled symbols while the elastic strain energy, W_{elastic}, is depicted by empty symbols.
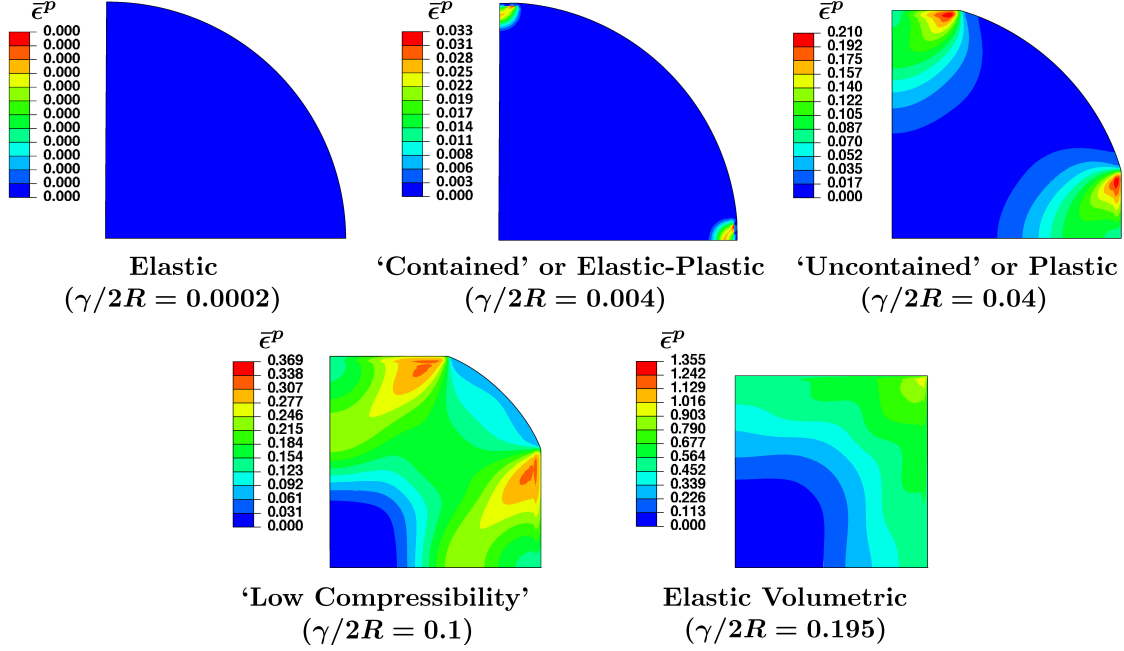
Fig.2.4. Contour plots of the equivalent plastic strain ($\bar{\epsilon}^p$) for hydrostatic compaction of a lead sphere obtained from FE simulation of $(1/8)^{\text{th}}$ of the sphere. The different plots represent different stages of particle compression with increasing deformation or $\gamma/2R$.

It is evident from Fig. 2.1 that the contact behavior is strongly dependent on the loading configuration, especially at moderate-to-large deformations. Further insight into the deformation mechanisms governing such contact behavior is obtained by the analysis of the evolution of external work and stored energy (Fig. 2.3 for hydrostatic compaction) as well as the equivalent plastic strain (Fig. 2.4 for hydrostatic compaction) in the particle during compression. It is observed that during intial compression, deformations are purely elastic and total external work is stored as strain energy in the particle. With further compression, local plastic deformation is observed at the vicinity of each contact where yielding occurs for the first time. Initially, the plastic zone is fully contained within the surrounding material which remains elastic. Therefore, the contact deformation mode within this regime is termed as a 'contained' or elastic-plastic deformation mode (K. L. Johnson, 1987, 1970; Stronge, 2018). On the onset of this deformation mode, the contact pressure and energy curves become non-linear with a decreasing slope, and the external work and strain energy curves start to diverge due to plastic dissipation. The plastically deforming

zone quickly expands and breaks out to the free surface, resulting in plastic flow of the material surrounding the contact area. This is called an 'uncontained' or plastic mode of deformation (K. L. Johnson, 1987, 1970; Stronge, 2018), and it is designated by a slight softening or a reduction in the contact pressure and a lowering of the rate of increase in stored energy with further deformation. It is worth mentioning that this deformation regime has been previously studied by Frenning and co-workers (Frenning, 2013; Jonsson, Gråsjö, & Frenning, 2017) and (Tsigginos, Strong, & Zavaliangos, 2015), who attribute the softening effect to the full mergence of plastically deforming zones around the contacts. A different interpretation is offered by Jackson, Green, and co-workers (Jackson & Green, 2005, 2006; Quicksall, Jackson, & Green, 2004), who postulate that the flattening or indentation of a sphere onto a surface causes its geometry to approach that of a compressed column and its contact pressure to approach the material's yield or representative strength. Until this point, contacts can be assumed independent of each other, yielding similar force, area and pressure evolution regardless of the loading configuration (see Fig. 2.1 for deformations under 10%). With further deformation, the void volume around the particle gets increasingly filled by the material displaced by plastic deformation. For simple compression, the void volume is infinitely large and material displacement in the lateral direction does not affect the contact pressure which, in turn, continues to reduce and approach the representative strength of the material. However, for die and hydrostatic loading conditions, the void volume is finite and the contact pressure increases with increasing particle deformation. This phenomenon, termed 'geometrical hardening' by (Sundstrom & Fischmeister, 1973) and 'low compressibility' regime by (Tsigginos et al., 2015), is characterized by a rising rate of increase in the elastic strain energy of the particle, indicating that further particle deformation is predominantly governed by the elastic response of the material. Finally, at very large deformations, when the local relative density of the particle is close to 1, deformations are purely elastic volumetric, requiring a very high compaction pressure to achieve a small volumetric reduction. Due to the higher degree of confinement, void filling occurs at a faster rate during hydrostatic loading as compared to the die loading condition, resulting in the contact pressure rising at a smaller contact deformation for the hydrostatic as compared to the die configuration (see Fig. 2.1).
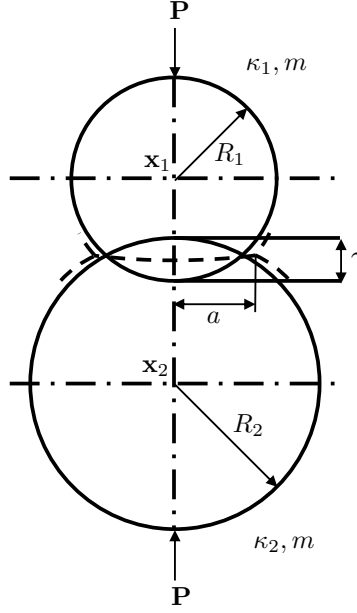
Fig.2.5. Schematic of the two-particle contact problem, depicting the contact between two spherical particles of radii R_1 and R_2. The particles are made of rigid-plastic power law hardening material with strengths κ_1 and κ_2 and a common power-law hardening exponent m. A displacement γ of the centers of mass of the particles located at positions $\mathbf{x}_1$ and $\mathbf{x}_2$ results in a contact force P and contact area of radius a.

For deformations in the 'contained' mode, spherical cavity expansion models of elasto-plastic indentation of a half space have been proposed for both small (Gao, Jing, & Subhash, 2006; Hardy, Baronet, & Tordion, 1971; K. L. Johnson, 1987; Mata, Casals, & Alcalá, 2006; Studman, Moore, & Jones, 1977) and large deformations (Liu et al., 2014). For materials undergoing negligible elastic deformations and predominant 'uncontained' plastic deformations (i.e., for materials described by a rigid-plastic power law hardening), Biwa and Storåkers (Biwa & Storåkers, 1995; B. Storåkers et al., 1997) formulated a contact model by reduction of a moving boundary contact problem to a self-similar stationary one. The model was derived by first solving the fundamental contact problem of a curved rigid indenter in contact with a deformable half space (Hill, Storåkers, & Zdunek, 1989), from which the solution of two contacting spheres of different radii and strengths, but same hardening exponent, could be

obtained. Specifically, the contact force P between two spheres (Fig. 2.5) of radii R_1 and R_2, strengths κ_1 and κ_2, and plastic power-law hardening exponent m, is given by

$$P = \eta_{\mathrm{P}} a^{2+1/m} \tag{2.4}$$

and the contact radius a is given by

$$a = \left(\frac{2c^2}{\mathbb{A}}\right)^{1/2} \gamma^{1/2} \tag{2.5}$$

where γ is the relative displacement of the particles

$$\gamma = R_1 + R_2 - ||\mathbf{x}_1 - \mathbf{x}_2|| \tag{2.6}$$

In the above equation the geometric parameter $\mathbb{A}$ and the plastic law coefficient η_{P} are given by

$$\mathbb{A} = \frac{1}{R_1} + \frac{1}{R_2} \tag{2.7}$$

$$\eta_{\mathrm{P}} = \pi k \mathbb{A}^{1/m} \left(\frac{1}{\kappa_1^m} + \frac{1}{\kappa_2^m}\right)^{-1/m} \tag{2.8}$$

with $k = 3 \times 6^{-1/m}$ and $c^2 = 1.43\mathrm{e}^{-0.97/m}$ (Bertil Storåkers & Larsson, 1994). Figure 2.1 illustrates that this solution is independent of the loading configuration and diverges from the response curves at small deformations ($\sim 3\%$). This behavior stems from the simplifying assumption of small-strain kinematics and independent contacts.

The formulation of a mechanistic contact law capable of describing the contact behavior at large deformation regimes of particle compression is particularly challenging, since it involves relaxing the assumptions of independent contacts and small-strain kinematics. The contact formulation must also account for complex phenomena such as softening at moderate strains and the significant increase in contact pressure in confined loading conditions at large strains. (Harthong et al., 2009; Harthong et al., 2012) made initial progress in this regard and proposed a semi-mechanistic DEM contact law for spherical particles with rigid plastic

power-law hardening material behavior through curve fitting of force-deformation FE data of particle compression under simple, die and hydrostatic loading conditions. The model employs a local relative density dependent stiffness to capture the rise in contact force for confined loading conditions due to plastic incompressibility at large deformations. While the model is highly predictive at large deformations, it does not provide an estimation of the contact radius and it neglects elastic deformations, leading to infinite force as the relative density tends to unity. (Frenning, 2013) proposed a truncated sphere model applicable to small-to-moderate deformations of a spherical particle under a general loading configuration. The model assumes plastic incompressibility to relate the average pressure in the particle due to elastic volumetric strain, to the mean pressure generated at the particle contacts. For the specific case of hydrostatic loading condition, (Frenning, 2015) later extended the model to account for contact impingement and low compressibility at large deformations. (E. Olsson & Larsson, 2016; Erik Olsson & Larsson, 2013a, 2013b) proposed semi-analytical contact laws for elasto-plastic spherical particles under simple loading configuration that are predictive at large deformations. The formulation extends a correlation between indentation depth and contact radius proposed by (K. Johnson, 1970) for elasto-plastic materials.

Despite the recent developments, the formulation of a mechanistic contact model for large deformation contact behavior of elasto-plastic spherical particles under general loading conditions remains an open problem. We make progress towards achieving this goal by developing a formulation for both contact force and contact radius of elasto-plastic particles under unconfined and confined compression in a simple-cubic packing. This paper presents a semi-mechanistic contact formulation for elastic-perfectly plastic spherical particles under simple, die and hydrostatic loading configurations. Specifically, contact laws for the evolution of contact pressure and contact radius with deformation are proposed. Contact radius is derived as a three-term expansion of the curvature-corrected similarity contact law (Agarwal & Gonzalez, 2018), where each term adds to the contact response under small, moderate and large deformations, respectively. Contact pressure is a piecewise C^1-continuous function, described in each deformation regime by distinct laws. The proposed semi-mechanistic contact formulation is both material and loading-condition dependent, accounting for initial elastic and elasto-plastic deformations and for limited elastic compressibility in confined loading

conditions (i.e., die and hydrostatic conditions) at large deformations. This is accomplished by calibrating (thus, the semi-mechanistic nature of the formulation) the various model parameters to a sufficiently large set of finite element simulations, where the set of elasto-plastic material properties used to perform the simulations is obtained through a space-filling design over a sufficiently large range of material properties.

The paper is organized as follows. Section 2.2 describes the space-filling design problem for acquiring mechanical properties used in the finite element simulations. The finite element results are then presented and discussed in Section 2.3. A detailed description of the semi-mechanistic contact formulation is presented in Section 2.4, followed by its verification through a comparison of model predictions with the finite element results in Section 2.5. An analysis of lateral contacts in the die loading configuration is presented in Section 2.6. Finally, a summary and concluding remarks are presented in Section 2.7.

2.2 Space-filling design of experiments for finite element analysis

A diverse set of elasto-plastic material properties for the finite element simulations is obtained as the solution of a space-filling design problem (Santner, Williams, & Notz, 2013). The factors that characterize the design space are three mechanical properties, namely, Young's modulus (E), Poisson's ratio (ν), and uniaxial yield stress (σ_y), as well as the loading configuration (LC). Table 2.1 provides bounds for the quantitative factors, i.e., the mechanical properties E, ν and σ_y. The bounds are selected to encompass the observed properties of most elasto-plastic materials (thermoplastic polymers, metals, alloys, pharmaceutical powders, etc.) and to ensure that the mechanical properties used in the FE simulations are representative of real materials. The loading configuration (LC), being a qualitative (categorical) factor, is

Table 2.1. Bounds for the independent variables and nonlinear constraint considered in the space-filling design problem

	Minimum Value	Maximum Value
E (MPa)	$2,000$	$200,000$
σ_y (MPa)	1	500
ν	0.2	0.48

assigned three levels, i.e., simple, die and hydrostatic, which are the loading configurations considered in this study.
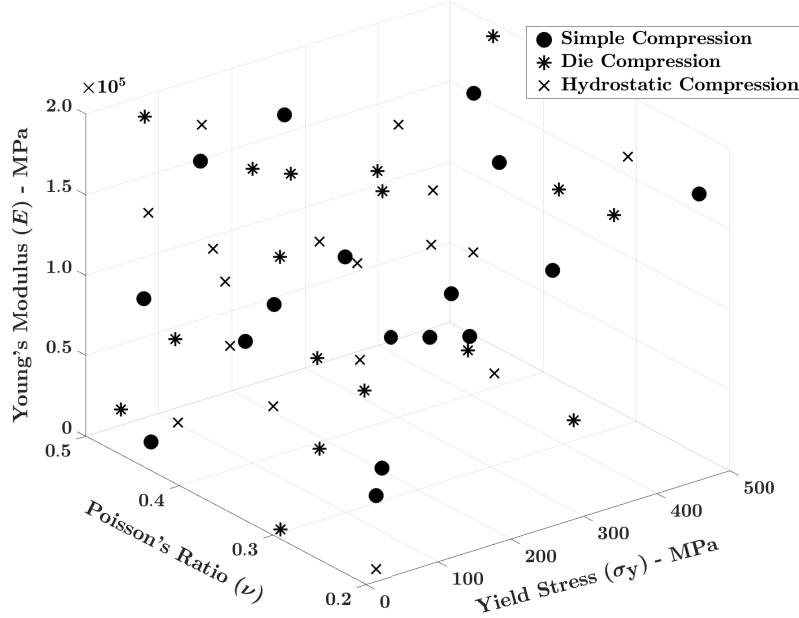
Fig.2.6. Scatter plot of the design points obtained from the space-filling design of mechanical properties and loading configurations for the FE study.

The formulated design problem was solved in the statistical software ("SAS Institute Inc", 2018) using the Fast Flexible Filling (FFF) algorithm, which is capable of incorporating categorical factors (SAS Institute Inc., 2018). Specifically, the FFF algorithm generates a large number of points within the design space, and groups them into N/k primary clusters using a fast Ward's algorithm (Ward Jr., 1963), were N is the total number of requested design points and k is the number of categorical levels. It then creates k sub-clusters per primary cluster, and calculates a design point within each sub-cluster by minimizing a maximum projection (MaxPro) criterion (Joseph, Gul, & Ba, 2015). Finally, it randomly assigns one of the k categorical levels to each sub-cluster, yielding the total of N design points. For the FE study, a total of 51 design points were obtained, i.e., 17 points for each of the three loading configurations. Figure 2.6 shows the set of design points obtained for the three symmetric loading configurations, while Table A.1 in A provides a complete list of the mechanical properties obtained by solving the design problem. In Table A.1, the mechanical properties

for each loading configuration are arranged in the increasing order of the material-dependent dimensionless parameter $E/(1 - \nu^2)\sigma_y$, which has been shown to significantly influence the contact behavior during initial stages of particle compression (Mesarovic & Fleck, 2000). It is evident from the table that a sufficient spread of this parameter is also obtained, along with fairly-spaced material properties over a wide range of values as apparent from Fig. 2.6.

2.3   Finite element analysis

On the account of geometric and loading symmetries, finite-element simulations were performed on one-eighth of a sphere of radius $R = 10$ mm in ABAQUS, Version 6.14. The mesh is comprised of 500,000 linear hexahedral elements of type C3D8R and 515,201 nodes. For representational purposes, a coarser mesh of 62,500 elements and 66,351 nodes is depicted in Fig. 2.7. The material is elastic-ideal plastic (i.e., a hardening exponent $m \to \infty$ in Eq. (2.3)) with the following constitutive law

$$\sigma = \begin{cases} E\epsilon & \epsilon \le \epsilon_y \\ \sigma_y & \epsilon > \epsilon_y \end{cases} \tag{2.9}$$

A total of 51 FE simulations were performed with this model, 17 for each loading configuration (simple, die and hydrostatic) using the material properties obtained from the space-filling design.
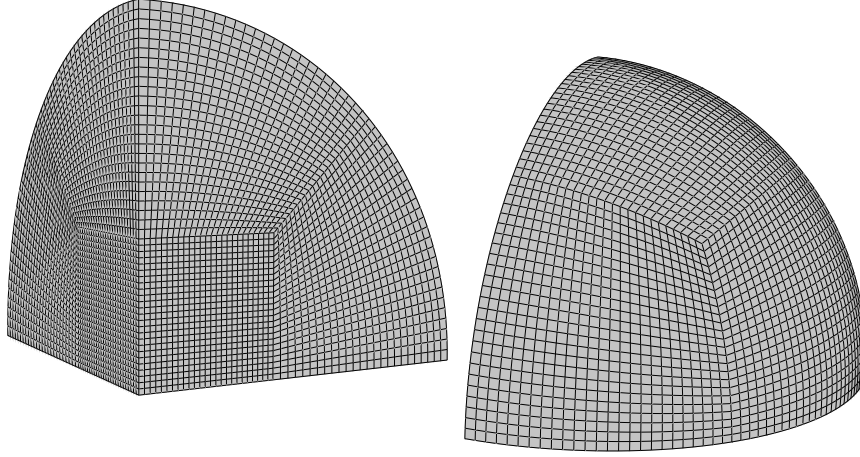
Fig.2.7. Finite element mesh consisting of linear hexahedral elements of type C3D8R, created for one-eighth of a sphere in ABAQUS. The depicted mesh is coarser than the final converged mesh, and consists of 62,500 elements and 66,351 nodes.

(a) Die Compaction   (b) Hydrostatic Compaction
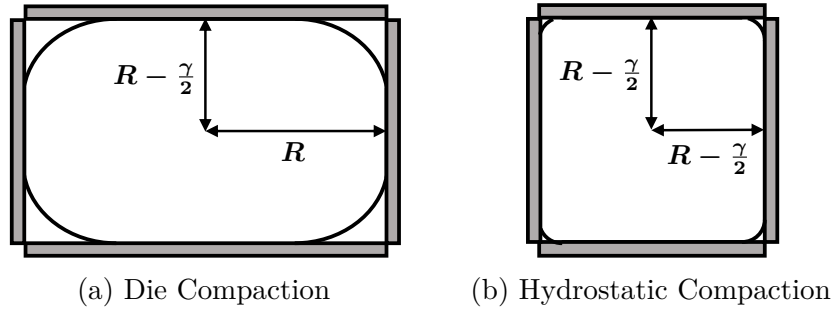
Fig.2.8. Schematic of the voronoi cell for (a) die and (b) hydrostatic loading configurations.

To simulate the extensive particle deformation conditions during powder compaction process, the contact response for simple compression was evaluated until 50% deformation at the particle level (i.e., $\gamma/2R = 0.50$). For hydrostatic and die configurations, a state of complete closure of porosity is achieved with continued particle deformation and material flow. This stage is termed as the zero porosity limit (Tsigginos et al., 2015), following which the stresses required for further deformation are very high and are goverened by the bulk modulus of the material. The volume of the particle's radical voronoi cell (Aurenhammer, 1987; Gellatly & Finney, 1982), which is the polyhedron formed by the rigid contact planes of the particle, becomes equal to the particle volume at the zero porosity limit. Therefore, by

31

neglecting the elastic volume reduction during initial stages of particle compression, this limit can be geometrically computed and it is equal to $\gamma/2R = 1 - \pi/6$ and to $\gamma/2R = 1 - (\pi/6)^{1/3}$, for die and hydrostatic compaction, respectively (see Fig. 2.8). The contact response was then evaluated until the deformation at the particle level surpasses the geometric zero porosity limit by a small margin, i.e., beyond 47.6% for die and 19.4% for hydrostatic loading configurations.

(a)

(b)

(c)
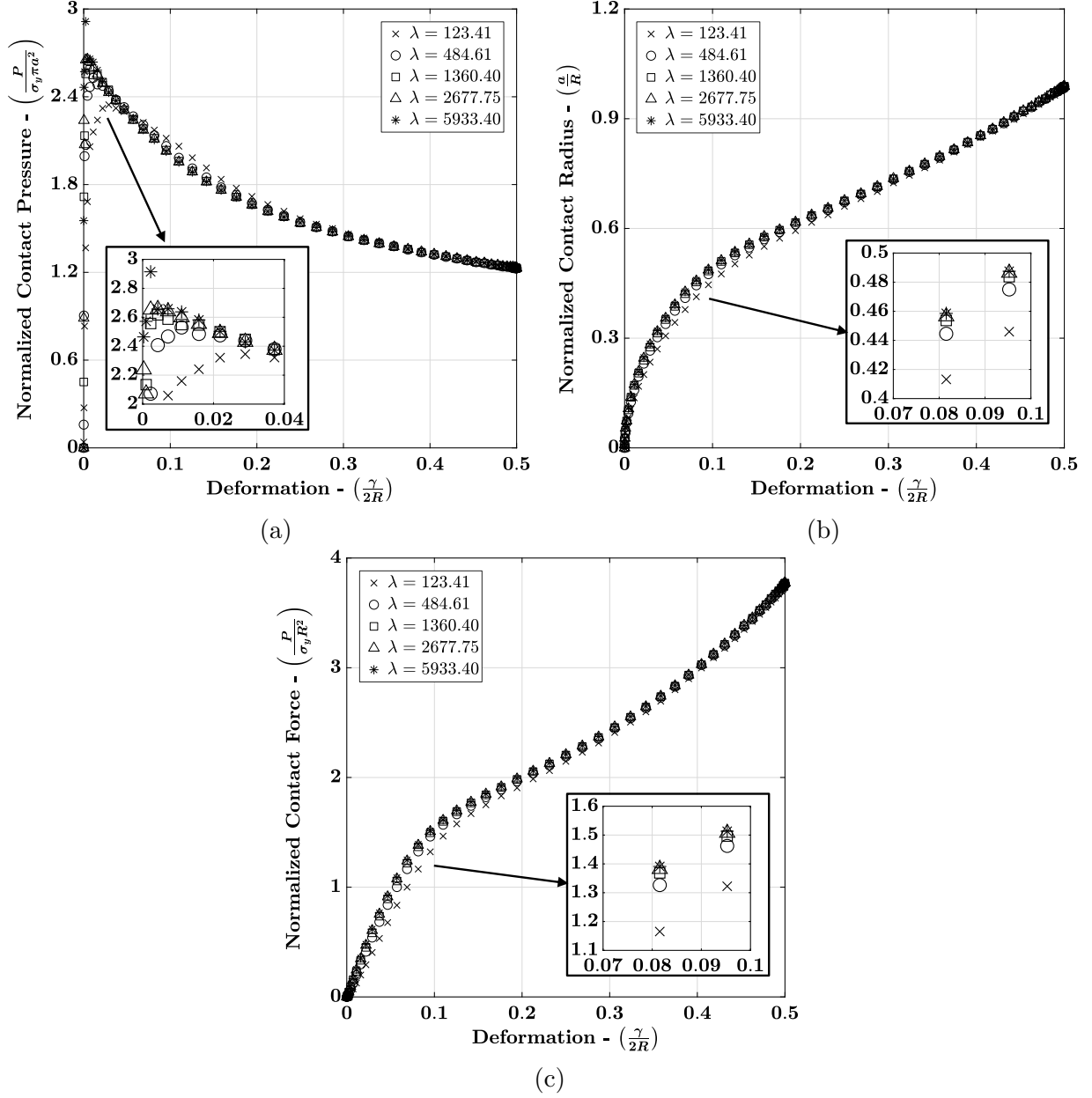
Fig.2.9. Finite element simulation results of normalized (a) contact pressure-deformation, (b) contact radius-deformation, and (c) contact force-deformation behavior of an elastic- perfectly plastic sphere of radius $R = 10$ mm under simple compression. Contact response is depicted for 5 out of the 17 material properties obtained from the space-filling design, ranging from minimum to maximum value of the material parameter $\lambda = E/(1 - \nu^2)\sigma_y$.
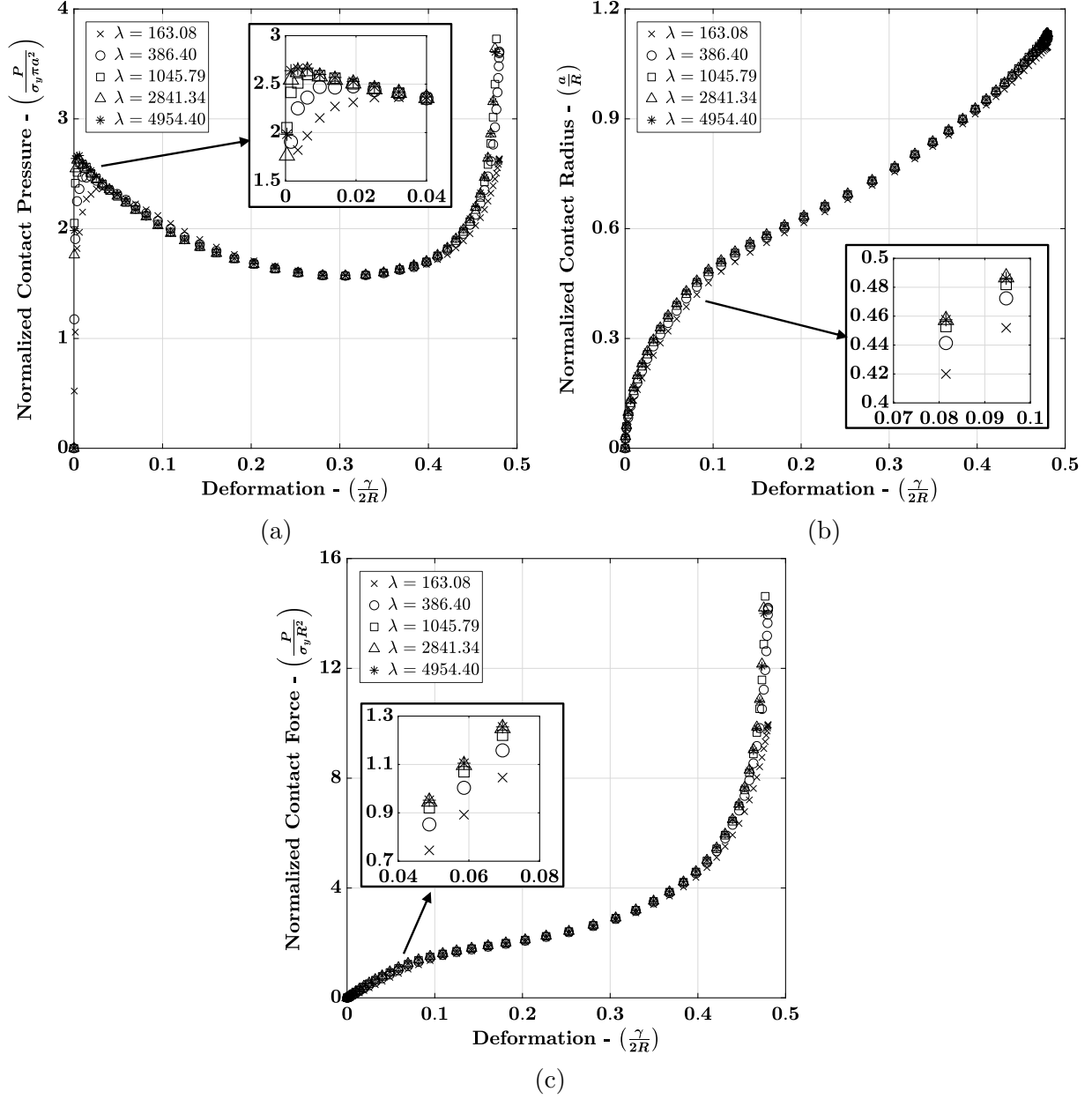
Fig.2.10. Finite element simulation results of normalized (a) contact pressure-deformation, (b) contact radius-deformation, and (c) contact force-deformation behavior at the primary (axial) contacts of an elastic- perfectly plastic sphere of radius $R = 10$ mm under die compression. Contact response is depicted for 5 out of the 17 material properties obtained from the space-filling design, ranging from minimum to maximum value of the material parameter $\lambda = E/(1 - \nu^2)\sigma_y$.

(a)

(b)

(c)
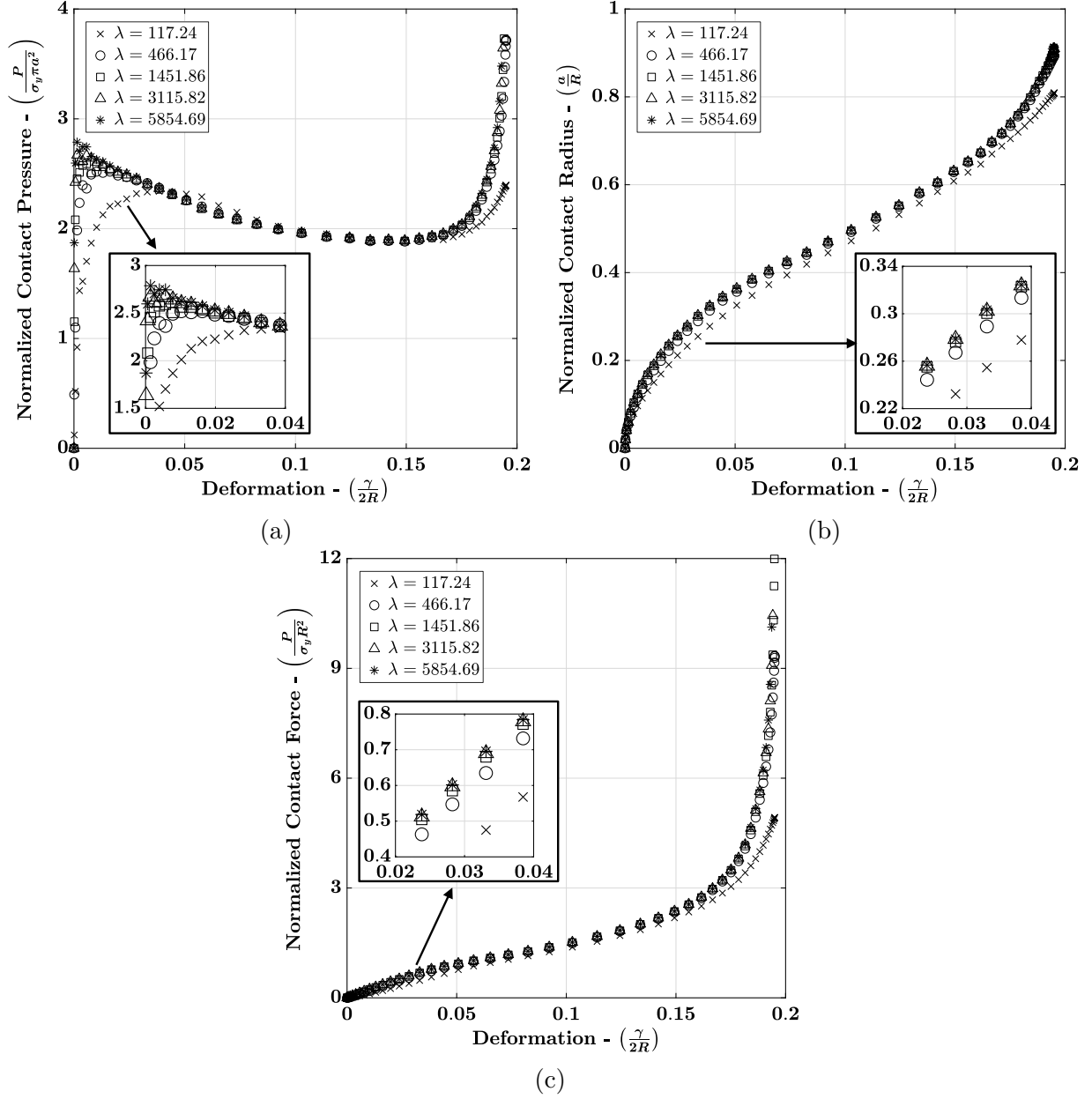
Fig.2.11. Finite element simulation results of normalized (a) contact pressure-deformation, (b) contact radius-deformation, and (c) contact force-deformation behavior of an elastic- perfectly plastic sphere of radius $R = 10$ mm under hydrostatic compaction. Contact response is depicted for 5 out of the 17 material properties obtained from the space-filling design, ranging from minimum to maximum value of the material parameter $\lambda = E/(1 - \nu^2)\sigma_y$.

2.3.1 Primary contacts

Figures 2.9, 2.10 and 2.11 show the normalized contact pressure $(P/\sigma_y \pi a^2)$, contact radius (a/R) and contact force $(P/\sigma_y R^2)$ response plotted against contact deformation $(\gamma/2R)$, for 5 out of the 17 particles simulated under simple, die and hydrostatic loading configurations, respectively. These particles cover the wide range of $E/(1 - \nu^2)\sigma_y$ values (referred to as parameter λ in the rest of this paper) obtained from the space-filling design. For the simple loading configuration, the contact pressure during the elastic and the elastic-plastic regimes depends on material properties, exhibiting higher stiffness and larger maximum contact pressure at larger values of λ (see Fig. 2.9a). This trend converges at higher values of λ, indicating an asymptotic relationship with respect to material properties. Following the onset of the plastic regime, the contact pressure is independent of material properties and it decreases with deformation. Similar observations are made in the response of contact radius (Fig. 2.9b) and contact force (Fig. 2.9c), with contact stiffness rising asymptotically with increasing λ for small-to-moderate particle deformation ($\sim 20\%$) and converging to a common response at larger deformation. The effect of material properties becomes increasingly apparent under hydrostatic loading (Fig. 2.11a), where the contact pressure follows the trend of simple loading until 15% deformation (cf. Fig. 2.9a), following which the contact pressure increases rapidly with increasing particle confinement. Elasticity becomes relevant again during last stage of compression, where stiffness, pressure, contact radius and force increase with increasing λ and follow an asymptotic behavior as in all other stages of compression.

(a)

(b)

(c)
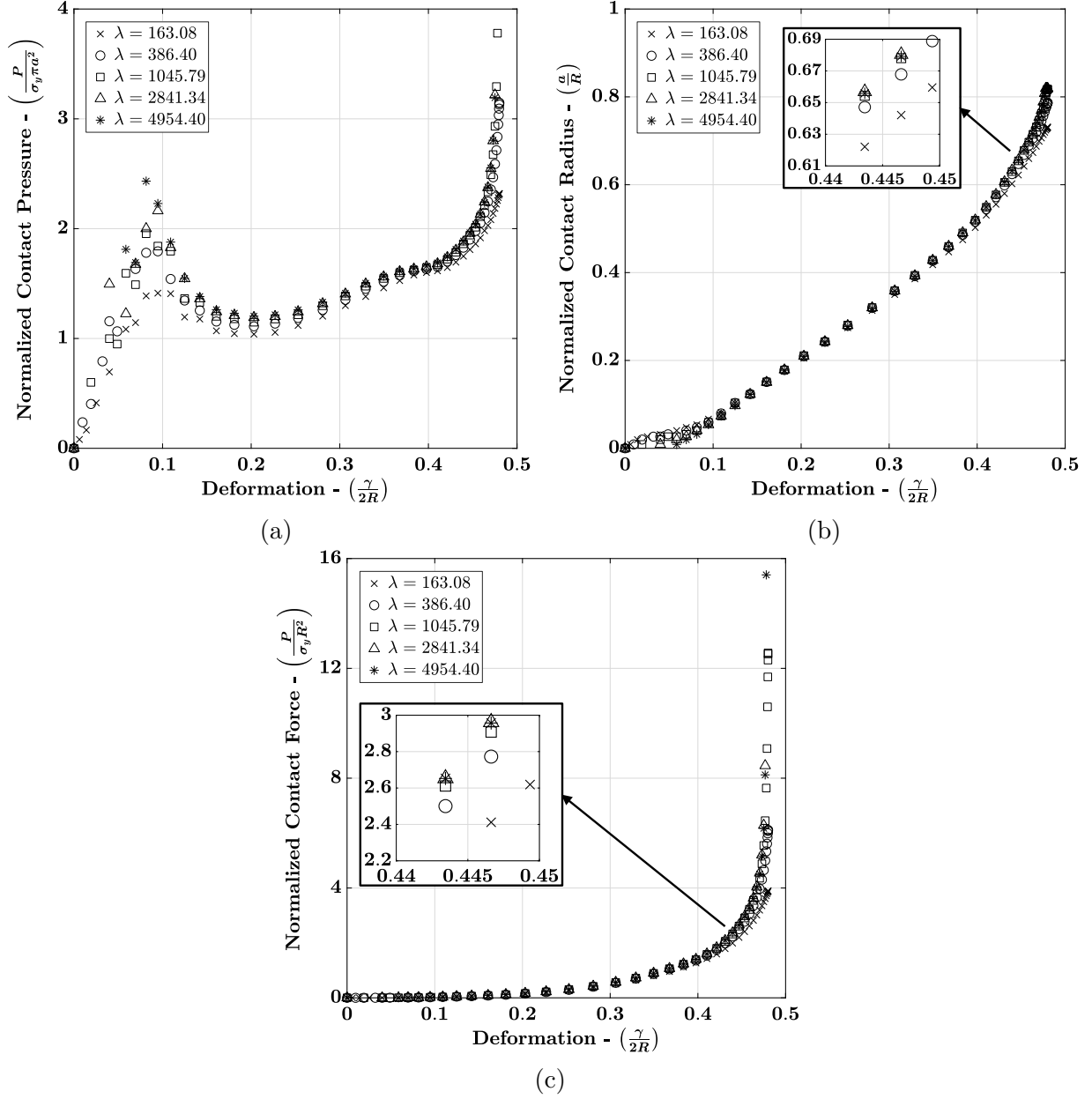
Fig.2.12. Finite element simulation results of normalized (a) contact pressure-deformation, (b) contact radius-deformation, and (c) contact force-deformation behavior at the secondary (lateral) contacts of an elastic- perfectly plastic sphere of radius $R = 10$ mm under die compression. Contact response is depicted for 5 out of the 17 material properties obtained from the space-filling design, ranging from minimum to maximum value of the material parameter $\lambda = E/(1 - \nu^2)\sigma_y$.
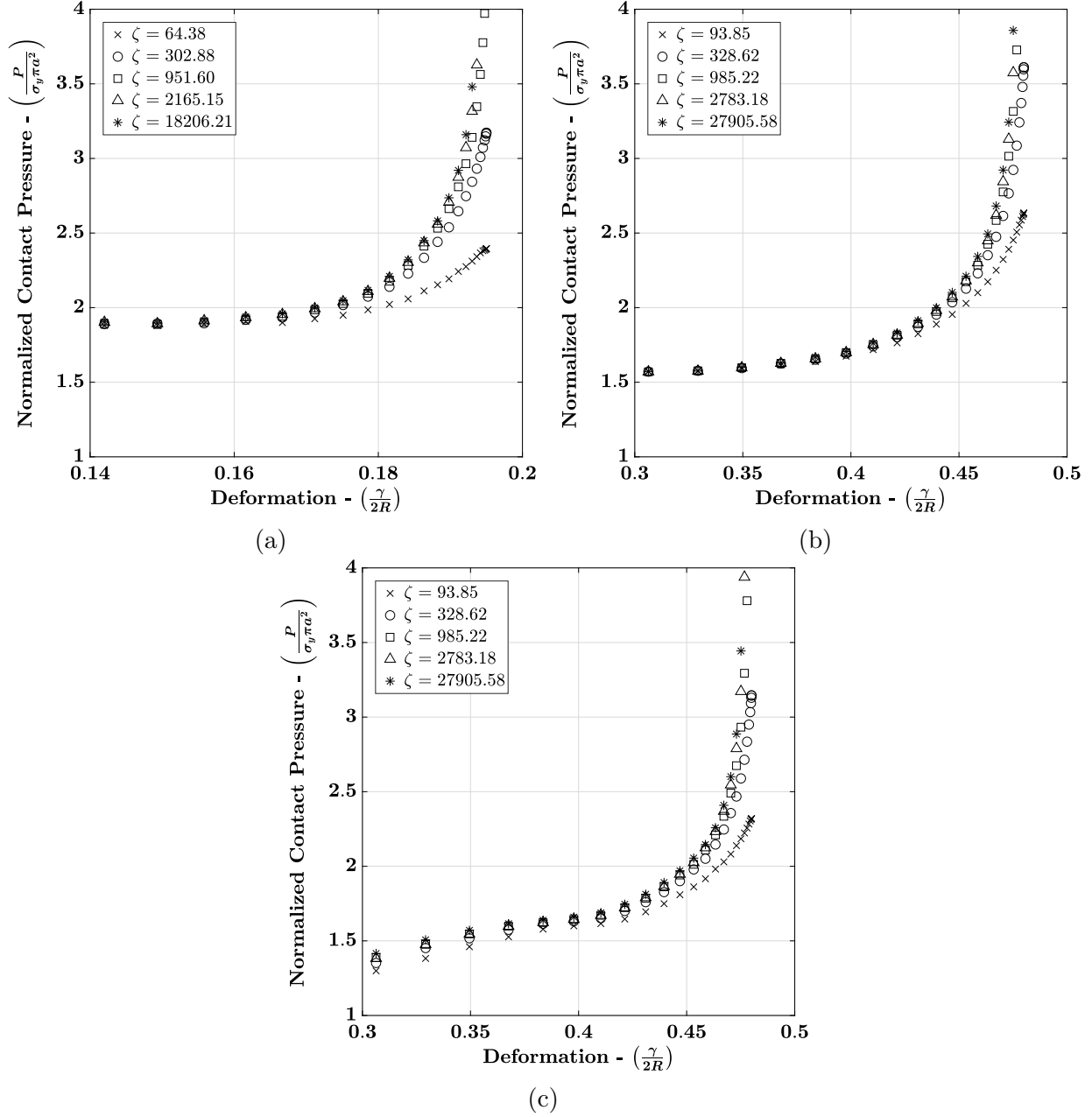
Fig.2.13. Finite element simulation results of normalized contact pressure-deformation behavior of an elastic- perfectly plastic sphere of radius $R = 10$ mm during 'low compressibility' regime (Tsigginos, Strong, & Zavaliangos, 2015), under (a) hydrostatic compaction, (b) die compression (primary contacts) and (c) die compression (secondary contacts). Contact response is depicted for 5 out of the 17 material properties obtained from the space-filling design, ranging from minimum to maximum value of the material parameter $\zeta = B/\sigma_y$.

2.3.2 Secondary contacts

The contact response of secondary contacts of the die loading configuration, i.e., contact interactions formed with lateral stationary walls, is shown in Fig. 2.12. While primary contacts of die compression exhibit, in the initial stages of deformation, a response similar to those in the simple loading configuration (cf. Fig. 2.10 up to $\sim 30\%$). It is worth noting that secondary contacts, despite not being subjected to any kinematic deformation (i.e., lateral walls are stationary), exhibit an evolution of contact pressure, area, and force that increases with increasing deformation of the primary contact. Furthermore, contact pressures of primary and secondary contacts are similar at later stages of compression. It bear emphasis that local contact formulations, such as the similarity contact law, treat contacts as independent from each other and, thus, do not predict these secondary contacts. In sharp contrast, nonlocal contact formulations are capable of predicting secondary contacts by estimating the nonlocal lateral deformation in the secondary contacts (see M. Gonzalez and Cuitiño, 2012, 2016 and Agarwal and Gonzalez, 2018) for an nonlocal contact formulation for elastic particles). The systematic development of a nonlocal contact formulation for elasto-plastic particles is beyond the scope of this paper and it is currently being pursued by the authors. However, a foundational semi-mechanistic analysis of the secondary contacts is presented in one of the later sections of this paper.

2.3.3 Low compressibility regime

The low compressibility regime occurs under confined loading conditions and it is mainly governed by the elastic compressibility of the material, and it leads to rising contact pressure values during the final stages of compression. Fig. 2.13 shows a magnified view of this regime for the hydrostatic loading configuration and for the primary and secondary contacts of the die loading configuration for different values of $\zeta = B/\sigma_y$, where B is the elastic bulk modulus of the material. An apparent asymptotic relationship of the contact pressure with respect to ζ is observed in all the plots, with the response stiffness and pressure values rising rapidly with increasing ζ and converging to a single curve for larger values of ζ.

2.3.4 Asymptotic behavior

We close this section by pointing out the evident asymptotic relationship between the contact response and dimensionless material parameters λ and ζ, during both the initial and the final stages of particle compression. This observation provides key insight into the material dependence of the contact behavior in confined granular systems, which is essential for the development of accurate and predictive contact models, as we will demonstrate next.

2.4 Formulation of a semi-mechanistic contact law

We have demonstrated that a semi-mechanistic contact law for elastic-ideally plastic spherical particles under large deformation must account for the dependency on material properties (i.e., E, ν, σ_y) and loading conditions (i.e., in this work, simple, die, and hydrostatic compression). Therefore, we first revisit the contact problem described by the similarity solution explained in Section 2.1, where the contact force (Eq. (2.4)) for an ideally plastic material ($m \to \infty$) reduces to

$$P = 3\sigma_y \pi a^2 \tag{2.10}$$

From the above equation, the average contact pressure, or Brinell hardness H of the material for the case of a deformable flat surface indented by a rigid spherical indenter, is recovered as

$$H = \frac{P}{\pi a^2} = 3\sigma_y = \bar{H}\sigma_y \tag{2.11}$$

where $\bar{H}$ is the normalized hardness (E. Olsson & Larsson, 2016; Erik Olsson & Larsson, 2013a, 2013b). This result is in good agreement with the empirical findings of (Tabor, 1951), who proposed the hardness of materials from Brinell indentation tests to be given by $2.84\sigma_y$. However, FE simulations presented in section 2.3 suggest that the average contact pressure is not a constant but a function of (i) material parameters λ and ζ, and (ii) the loading configuration. Therefore, we propose a contact law of the form

$$P(\gamma; R, E, \nu, \sigma_y, \mathrm{LC}) := \bar{H}(\gamma/2R; \lambda, \zeta, \mathrm{LC})\ \sigma_y\ \pi\ a(\gamma; R, \lambda, \mathrm{LC})^2 \tag{2.12}$$

where LC corresponds to the loading configuration. In the next sections, we present semi-mechanistic functional relationships for the contact radius a and $\bar{H}$ (referred to as normalized contact pressure in this paper, as the term hardness is applicable exclusively for indentation) using an analytical framework based on the similarity contact law and the FE data.

2.4.1 Semi-mechanistic formulation for the contact radius
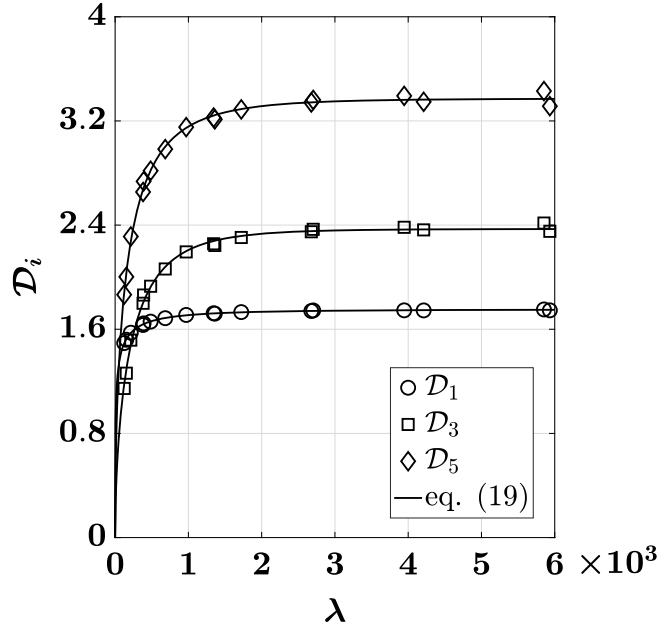
Fig.2.14. Estimation of parameters $\mathcal{D}_1$, $\mathcal{D}_3$, and $\mathcal{D}_5$ for simple loading configuration. Symbols correspond to values calibrated to FE data. Solid curves correspond to $\mathcal{D}_i - \lambda$ relationships obtained from curve fitting.

The similarity contact law (2.4)-(2.5), as well as Hertz contact law for elastic spheres (Hertz, 1882), not only assume small-kinematics but they also approximate the spherical profile of the contacting surfaces by paraboloids of revolution. The latter assumption was relaxed for elastic particles by (Agarwal & Gonzalez, 2018), who proposed the method of curvature correction to consider higher order terms in the Taylor series expansion of the spherical profile. In this study, we adopt this analytical framework to derive a semi-mechanistic contact radius formulation for spherical particles. A detailed derivation of a 2-term curvature corrected similarity solution is presented in B. We next adopt the first three terms of the Taylor

41

expansion of the relationship between contact radius a and particle relative displacement γ, i.e., (B.25), and generalize the expression as follows

$$a = \mathcal{D}_1 \left(\frac{1}{\mathbb{A}^{1/2}} \right) \gamma^{1/2} - \mathcal{D}_3 \left(\frac{\mathbb{B}}{\mathbb{A}^{5/2}} \right) \gamma^{3/2} + \mathcal{D}_5 \left(\frac{\mathbb{B}^2}{\mathbb{A}^{9/2}} \right) \gamma^{5/2} \qquad (2.13)$$

where $\mathbb{A}$ is given by Eq. (2.7), $\mathbb{B} = 1/R_1^3 + 1/R_2^3$, and parameters $\mathcal{D}_1$, $\mathcal{D}_3$, and $\mathcal{D}_5$ account for the dependency on material properties and the loading configuration. The first term corresponds to small plastic deformations and it is similar to the $a - \gamma$ relationship derived by (Biwa & Storåkers, 1995) using the self-similar approach. The second term describes the contact response during moderate plastic deformations, where the overall response undergoes softening and a dip in the slope of $a - \gamma$ curve is observed. The third term describes the large plastic deformations, i.e. the 'low compressibility' regime of confined loading conditions, where the slope of $a - \gamma$ curve rises again. It is worth noting that proposed law is similar to the stress-strain contact model proposed for large unconfined compression of microcrystalline cellulose particles by (Bommireddy, Agarwal, Yettella, Tomar, & Gonzalez, 2019).

It is evident from the FE simulations that dependency of $\mathcal{D}_1$, $\mathcal{D}_3$, and $\mathcal{D}_5$ on material properties and loading condition can be captured by

$$\mathcal{D}_i = \left(b_i^{\mathrm{LC}} \right)^{\frac{i}{2}} \left[\alpha_i \tanh \left(\beta_i \lambda^{\delta_i} \right) \right] \quad (i = 1, 3, 5) \qquad (2.14)$$

where each parameter $\mathcal{D}_i$ is expressed as an asymptotic material function of parameter λ, with coefficients α_i, β_i and δ_i, and a parameter b_i^{LC} that solely depends on loading condition. Simple compression (SC), being the most fundamental loading configuration where the particle remains unconfined, is assigned a loading condition parameter value of $b_i^{\mathrm{SC}} = 1$ ($i = 1, 3, 5$). The FE simulation data for simple compression is used first to estimate b_i^{SC}, β_i and δ_i (Fig. 2.14). Next, the values of b_i^{DC} and b_i^{HC} are estimated using the FE simulation data for die and hydrostatic compression. The estimated values and their corresponding 95% confidence intervals are listed in Table 2.2. It is interesting to note that $\mathcal{D}_1$ is asymptotic to 1.7527, which is very close to $\sqrt{2c^2} = 1.6911$ in Eq. (2.5) for $\lambda \to \infty$ (Bertil Storåkers & Larsson, 1994). Therefore, the small deformation predictions of the proposed contact law is consistent

with predictions of the similarity contact law as the material behavior approaches rigid plasticity. It is also interesting to note that $b_i^{\mathrm{SC}} < b_i^{\mathrm{DC}} < b_i^{\mathrm{HC}}$, which demonstrates the right loading-condition dependency of the proposed semi-mechanistic formulation for the contact radius.

Table 2.2. Estimated values of material function coefficients α_i, β_i and δ_i, and of parameters b_i^{LC} for simple (SC), die (DC) and hydrostatic (HC) loading configurations.

i	α_i	β_i	δ_i	b_i^{SC}	b_i^{DC}	b_i^{HC}
1	1.7527	0.3540	0.2633	1	1.048 ± 0.00477	1.1701 ± 0.0276
3	2.3702	0.0411	0.5366	1	1.1818 ± 0.00873	2.4002 ± 0.096
5	3.3715	0.0634	0.4766	1	1.2352 ± 0.00641	2.9376 ± 0.0452

2.4.2 Semi-mechanistic formulation for the normalized hardness

As already discussed in the previous sections, particle contacts undergo five major deformation regimes during large compression, namely elastic, elastic-plastic, plastic, and, for confined loading configurations, low compressibility and elastic volumetric. Since the evolution of normalized hardness $\bar{H}$ is found to be significantly different in each of these regimes, we propose distinct contact laws for each regime in a way that C^1 continuity is attained at the transition from one regime to another. Hence, the proposed semi-mechanistic formulation is continuous and differentiable at any given level of particle deformation.

During the elastic regime at small deformations, the well-known Hertz contact theory (Hertz, 1882) is capable of sufficiently describing the contact response. According to the theory, normalized hardness $\bar{H}$ for contact between particles of radii R_1 and R_2 and material parameter λ as a function of displacement γ is given by

$$\bar{H}^{\mathrm{e}} = \frac{2}{3\pi} \lambda \mathbb{A}^{1/2} \gamma^{1/2} \tag{2.15}$$

where $\mathbb{A}$ is given by Eq. (2.7), and the superscript "e" is used to denote the elastic regime. Using Eq. (2.15), the slope of $\bar{H}$ with respect to γ, i.e., $\partial\bar{H}/\partial\gamma$ in the elastic regime is given by

$$\frac{\partial\bar{H}^{\mathrm{e}}}{\partial\gamma} = \frac{1}{3\pi}\lambda\mathbb{A}^{1/2}\gamma^{-1/2} \tag{2.16}$$

The elastic regime transitions to the elastic-plastic regime when yield occurs at a point beneath the contact surface at $\bar{H} = 1.1$ (K. L. Johnson, 1987). Using Eq. (2.15), the contact displacement at yield, γ_y, is given by

$$\gamma_y = \frac{1}{\mathbb{A}}\left(\frac{3.3\pi}{2\lambda}\right)^2 \tag{2.17}$$

During the elastic-plastic regime, the non-linear evolution of $\bar{H}$ with respect to displacement γ is well-represented by the following relationship

$$\bar{H}^{\mathrm{ep}} = \bar{H}_{\mathrm{max}} - c_1\left[\ln\left(\frac{\gamma|_{\bar{H}_{\mathrm{max}}}}{\gamma}\right)\right]^{c_2} \tag{2.18}$$

where the superscript "ep" is used to denote the elastic-plastic regime. The proposed relationship is in spirit of a similar formulation proposed by (Erik Olsson & Larsson, 2013b) for the elastic-platic regime, where $\bar{H}$ is represented as a function of the Johnson's parameter (K. Johnson, 1970). In the above equation, $\bar{H}_{\mathrm{max}}$ and $\gamma|_{\bar{H}_{\mathrm{max}}}$ are, respectively, the maximum value of normalized hardness and the contact displacement observed at the transition between elastic-plastic and plastic regimes. Fig. 2.15 shows these values plotted against material parameter λ for all 51 FE simulations. Evidently, $\bar{H}_{\mathrm{max}}$ has an asymptotic increasing trend, while $\gamma|_{\bar{H}_{\mathrm{max}}}$ has an asymptotic decreasing trend with respect to the parameter. From fitting of the plotted values, we propose the following relationships for $\bar{H}_{\mathrm{max}}$ and $\gamma|_{\bar{H}_{\mathrm{max}}}$ with λ

$$\bar{H}_{\mathrm{max}} = 3.101\tanh\left\{0.6746\lambda^{0.0829}\right\} \tag{2.19}$$

$$\gamma|_{\bar{H}_{\mathrm{max}}} = (R_1 + R_2)\left[\exp\left(\frac{0.7073}{\lambda^{0.6547}}\right) - 1\right] \tag{2.20}$$

The proposed relationships are also plotted in Fig. 2.15 (solid curves), and provide very good estimates of the values obtained from FE simulations.
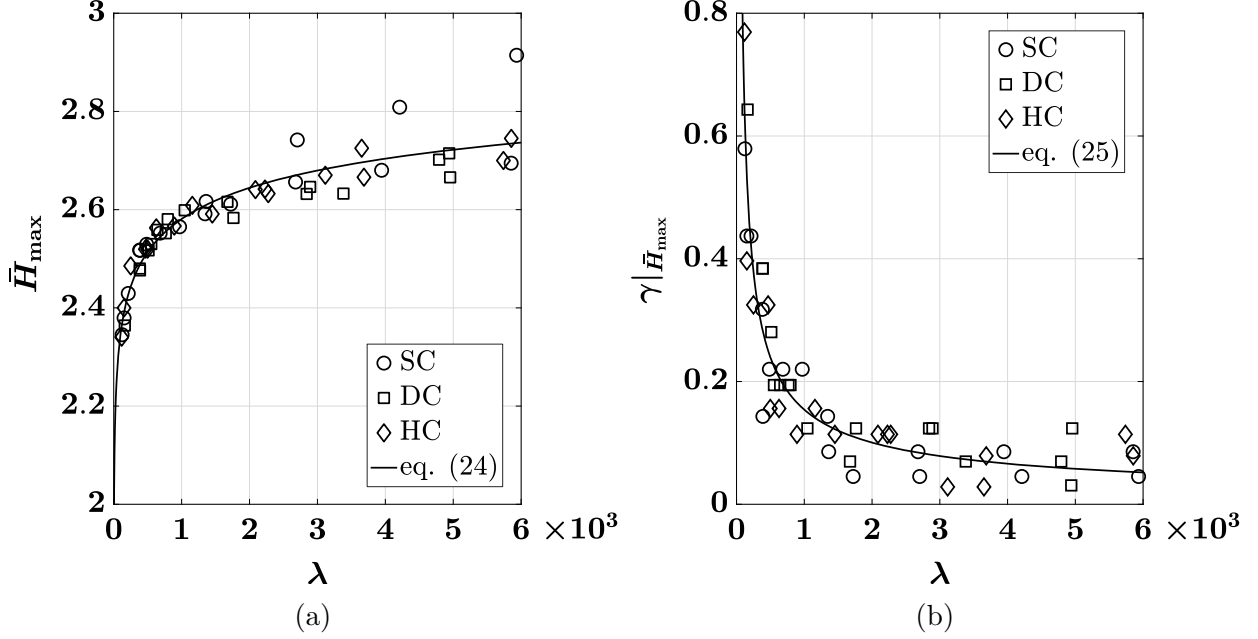
Fig.2.15. Estimation of (2.15a) $\bar{H}_{\max}$ and (2.15b) $\gamma|_{\bar{H}_{\max}}$ as functions of parameter λ. Plotted discrete values correspond to values obtained from FE data, while solid curves correspond to relationships obtained from curve fitting.

Additionally, the elastic-plastic $\bar{H}$ formulation comprises a coefficient c_1 and an exponent c_2, both of which are determined from the condition of C^1 continuity at the transition between elastic and elastic-plastic regimes. Using Eq. (2.18), the slope of $\bar{H}$ with respect to γ in the elastic-plastic regime is given by

$$\frac{\partial \bar{H}^{\mathrm{ep}}}{\partial \gamma} = \frac{c_1 c_2}{\gamma} \left[\ln \left(\frac{\gamma|_{\bar{H}_{\max}}}{\gamma} \right) \right]^{c_2 - 1} \tag{2.21}$$

which gives the condition $c_2 \geq 1$ for the slope given by the above equation to be equal to zero at $\gamma = \gamma|_{\bar{H}_{\max}}$. To achieve C^1 continuity for the evolution of $\bar{H}$ between elastic and elastic-plastic regimes, the values of $\bar{H}$ (Eq. (2.15) for elastic and Eq. (2.18) for elastic-plastic) and its first derivatives with respect to displacement γ (Eq. (2.16) for elastic and (2.21) for

elastic-plastic) at the transition displacement γ_y (Eq. (2.17)) are equated to finally obtain two equations with two unknowns c_1 and c_2. By solving the equations, we get

$$c_2 = \ln\left(\frac{\gamma|_{\bar{H}_{\max}}}{\gamma_y}\right)\left[\frac{\lambda \mathbb{A}^{1/2}\gamma_y^{1/2}}{3\pi(\bar{H}_{\max} - 1.1)}\right] \tag{2.22}$$

and

$$c_1 = (\bar{H}_{\max} - 1.1)\left[\ln\left(\frac{\gamma|_{\bar{H}_{\max}}}{\gamma_y}\right)\right]^{-c_2} \tag{2.23}$$

To determine the permissible values of material parameter λ for the fulfillment of the condition $c_2 \geq 1$, we substitute the expressions for γ_y, $\bar{H}_{\max}$ and $\gamma|_{\bar{H}_{\max}}$ given by Eqs. (2.17), (2.19) and (2.20) in the expression for c_2 given by Eq. (2.22) to obtain

$$c_2 = \frac{0.1774\ln\left[0.0372\mathbb{A}(R_1 + R_2)\lambda^2 \exp\left(\frac{0.7073}{\lambda^{0.6547}} - 1\right)\right]}{\tanh\{0.6746\lambda^{0.0829}\} - 0.3547} \geq 1 \tag{2.24}$$

For contacting particles of equal radii ($R_1 = R_2 = R$), which is the case for our considered loading configurations, $\mathbb{A} = 1/2R$ and $R_1 + R_2 = 2R$ cancel out each other, making Eq. (2.24) a nonlinear equation in λ. Using Newton Raphson's method, the solution to the equation is determined to be $\lambda \geq 22.08$. Therefore, the elastic-plastic $\bar{H} - \gamma$ relationship given by Eq. (2.18), and thus the proposed semi-mechanistic contact formulation, is valid for material parameter λ values greater than or equal to 22.08.

On the onset of the plastic regime, the normalized hardness $\bar{H}$ starts decreasing gradually from its previously achieved maximum value of $\bar{H}_{\max}$. While we acknowledge that a number of contact models have been proposed to predict the evolution of hardness in this regime (see (Ghaednia et al., 2017) and references therein), we propose a contact formulation that incorporates dependence on material properties and loading configuration while maintaining C^1 continuity with other deformation regimes. With this consideration, the normalized hardness in the plastic regime is given by

$$\bar{H}^{\text{fp}} = \bar{H}_{\max} - p\left[\tanh\left\{q\left(\frac{\gamma - \gamma|_{\bar{H}_{\max}}}{R_1 + R_2}\right)\right\}\cos\left\{\left(\frac{\gamma - \gamma|_{\bar{H}_{\max}}}{R_1 + R_2}\right) - s(\gamma|_{\bar{H}_{\min}}, q)\right\}\right]^r \tag{2.25}$$

46

where

$$s(\gamma|_{\bar{H}_{\min}}, q) = \left(\frac{\gamma|_{\bar{H}_{\min}} - \gamma|_{\bar{H}_{\max}}}{R_1 + R_2} \right) - \tan^{-1} \left[2q \operatorname{csch} \left\{ 2q \left(\frac{\gamma|_{\bar{H}_{\min}} - \gamma|_{\bar{H}_{\max}}}{R_1 + R_2} \right) \right\} \right] \qquad (2.26)$$

In the above equations, $\gamma|_{\bar{H}_{\min}}$ is the value of contact displacement at the minimum value of normalized hardness, i.e., $\bar{H}_{\min}$, while p, q, and r are positive model parameters. According to the proposed equations, the value of $\bar{H}^{\text{fp}}$ at $\gamma = \gamma|_{\bar{H}_{\max}}$ is equal to $\bar{H}_{\max}$, while its slope with respect to γ, given by

$$\begin{aligned}
\frac{\partial \bar{H}^{\text{fp}}}{\partial \gamma} = &-\left(\frac{pr}{R_1 + R_2} \right) \left[\tanh \left\{ q \left(\frac{\gamma - \gamma|_{\bar{H}_{\max}}}{R_1 + R_2} \right) \right\} \cos \left\{ \left(\frac{\gamma - \gamma|_{\bar{H}_{\max}}}{R_1 + R_2} \right) - s(\gamma|_{\bar{H}_{\min}}, q) \right\} \right]^{r-1} \\
&\times \left[q \operatorname{sech}^2 \left\{ q \left(\frac{\gamma - \gamma|_{\bar{H}_{\max}}}{R_1 + R_2} \right) \right\} \cos \left\{ \left(\frac{\gamma - \gamma|_{\bar{H}_{\max}}}{R_1 + R_2} \right) - s(\gamma|_{\bar{H}_{\min}}, q) \right\} \right. \\
&\left. - \tanh \left\{ q \left(\frac{\gamma - \gamma|_{\bar{H}_{\max}}}{R_1 + R_2} \right) \right\} \sin \left\{ \left(\frac{\gamma - \gamma|_{\bar{H}_{\max}}}{R_1 + R_2} \right) - s(\gamma|_{\bar{H}_{\min}}, q) \right\} \right]
\end{aligned}$$

$$(2.27)$$

is equal to zero at $\gamma = \gamma|_{\bar{H}_{\max}}$ for $r \geq 1$. Therefore, when the condition $r \geq 1$ is true, the $\bar{H}^{\text{fp}} - \gamma$ relationship given by Eqs. (2.25) and (2.26) is C^1 continuous with the $\bar{H}^{\text{ep}} - \gamma$ relationship given by Eq. (2.18).
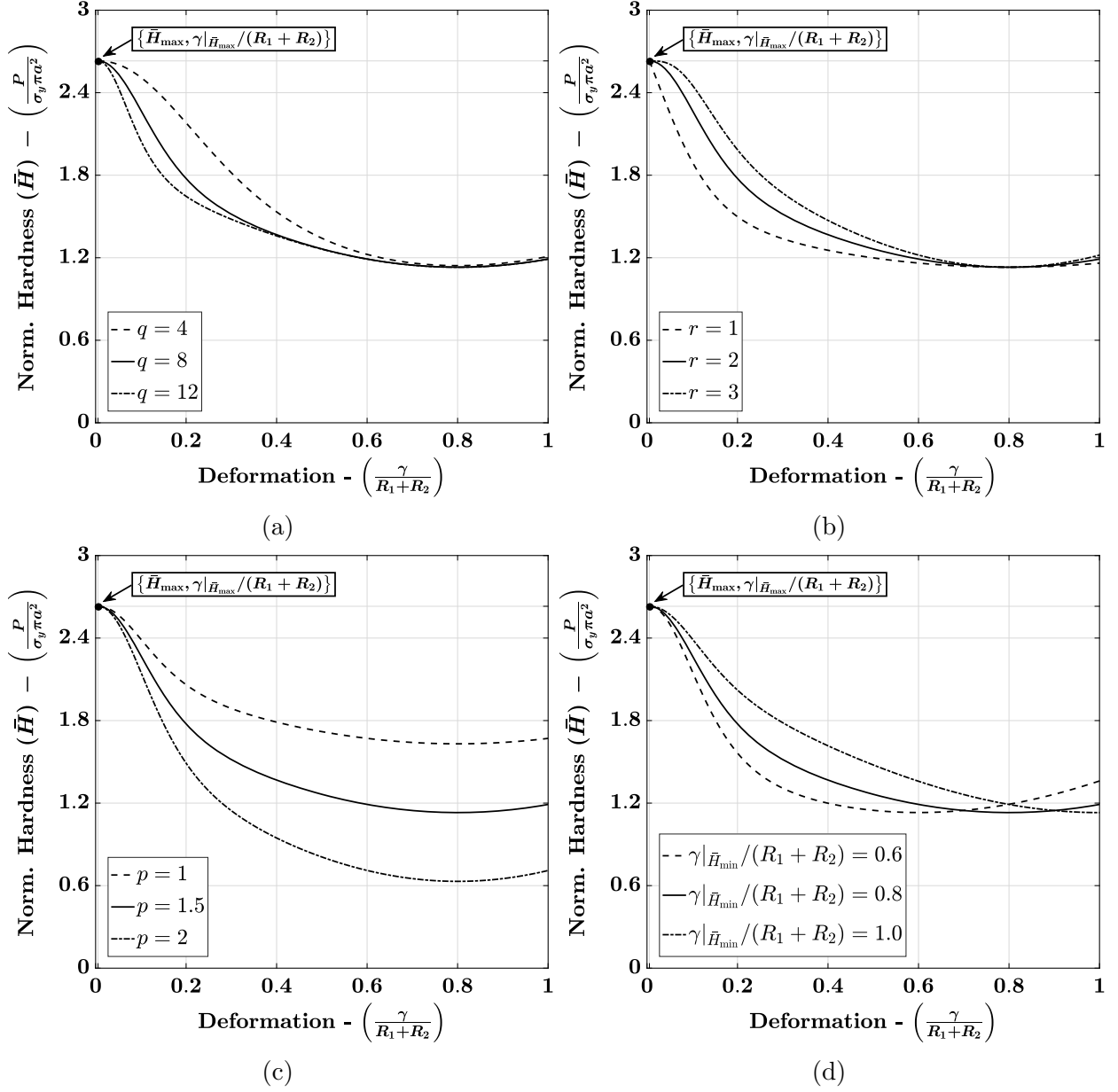
Fig.2.16. Analysis of the influence of model parameters (a) q, (b) r, (c) p and (d) $\gamma|_{\bar{H}_{\min}}$ on $\bar{H}^{\mathrm{fp}}$ model response. Solid curves correspond to the reference curve obtained by setting $q = 8$, $r = 2$, $p = 1.5$ and $\gamma|_{\bar{H}_{\min}}/(R_1 + R_2) = 0.8$, while the other curves (dashed-dotted and dashed) correspond to those obtained by perturbing one of the parameter values while keeping other values constant. The value of $\bar{H}_{\max}$ and $\gamma|_{\bar{H}_{\max}}/(R_1 + R_2)$ corresponds to $\lambda = 1721.55$.

Fig. 2.16 shows the influence of model parameters q, r, p and $\gamma|_{\bar{H}_{\min}}$ on the response of $\bar{H}^{\mathrm{fp}}$. In all figures, the reference model curve (solid line) is obtained by setting $p = 1.5$, $q = 8$,

$r = 2$ and $\gamma|_{\bar{H}_{\min}}/(R_1 + R_2) = 0.8$. The other curves (dashed and dashed-dotted lines) are obtained by perturbing one of the parameter values while keeping the other values constant. The value of $\bar{H}_{\max}$ and $\gamma|_{\bar{H}_{\max}}/(R_1 + R_2)$ in the plots is obtained by setting $\lambda = 1721.55$, which corresponds to the material properties with $E/\sigma_y = 1500.97$ for simple loading case obtained from the space-filling design (ref. Table A.1). From the study, it is evident that parameters q and r predominantly influence the rate of softening of $\bar{H}$, with r mainly controlling the rate at the onset of the plastic regime and q governing the rate of descent thereafter until the attainment of a minimum. Parameter $\gamma|_{\bar{H}_{\min}}$, as per its definition, predominantly influences the level of deformation at the minimum, while p regulates the value of $\bar{H}_{\min}$. It is important to note that the proposed equation models the evolution of $\bar{H}$ until the point of minimum, following which the loading condition effects predominate and another formulation is required to predict the rising pressure values for confined loading configurations.

From the observations of normalized hardness versus deformation data obtained from FE simulations, it is quite evident that the initial softening response from the onset of the plastic regime is primarily dependent on the material properties and fairly independent of the loading configuration. Therefore, parameters q and r are identified to be material-dependent parameters. However, the minimum value of $\bar{H}$ and the level of deformation at the minimum is heavily dependent on the loading configuration as well as the initial rate of softening. Therefore, $\gamma|_{\bar{H}_{\min}}$ and p are identified to be both material and loading condition-dependent parameters.

For the case of a simple loading configuration, it is theorized that the contact response softens until contact pressure approaches the material's yield strength as the particle geometry approaches that of a flat disk at $\gamma \to R_1 + R_2 = 2R$. Therefore, we obtain $\gamma^{\mathrm{SC}}|_{\bar{H}_{\min}} = R_1 + R_2 = 2R$. For confined loading configurations, the contact pressure rises again during the 'low compressibility' regime due to void filling, as well as occupation of the voronoi cell faces by the contact surfaces. While void filling causes the elastic energy of the particle to increase due to material compression, the voronoi cell faces limit the evolution of contact

areas, both of which lead to the increase in pressure. In accordance with this analysis, we propose the following condition to be true at the minimum:

$$\rho_V^{\text{LC,contact}} \times \rho_S^{\text{LC,contact}} = \Gamma \tag{2.28}$$

Thus, for a particular contact of a particle under a given loading condition, the product of relative volume density ($\rho_V^{\text{LC,contact}}$) and relative surface area density ($\rho_S^{\text{LC,contact}}$) is equal to a parameter Γ at the minimum. The relative volume density for a contact is given by

$$\rho_V^{\text{LC,contact}} = \rho_V^{\text{LC}} \times \left(\frac{V_{\text{contact}}^{\text{LC}}}{V_{\text{voro}}^{\text{LC}}} \right) = \left(\frac{V_{\text{particle}}}{V_{\text{voro}}^{\text{LC}}} \right) \left(\frac{V_{\text{contact}}^{\text{LC}}}{V_{\text{voro}}^{\text{LC}}} \right) \tag{2.29}$$

where $\rho_V^{\text{LC}} = \left(V_{\text{particle}} / V_{\text{voro}}^{\text{LC}} \right)$ is the relative density of the particle's voronoi cell (Harthong et al., 2009), $V_{\text{particle}} = (4/3)\pi R^3$ is the volume of the spherical particle, $V_{\text{voro}}^{\text{LC}}$ is the volume of the voronoi cell, and $V_{\text{contact}}^{\text{LC}}$ is a section of the voronoi cell volume associated with the contact, which is estimated as the volume of a pyramid with the base as the contact's voronoi cell face and apex as the particle's center of mass. The relative surface area density is given by

$$\rho_S^{\text{LC,contact}} = \frac{S_{\text{contact}}^{\text{LC}}}{S_{\text{face}}^{\text{LC}}} \tag{2.30}$$

where $S_{\text{contact}}^{\text{LC}}$ is the contact area and $S_{\text{face}}^{\text{LC}}$ is the area of the contact's voronoi cell face. Table 2.3 provides expressions for $V_{\text{voro}}^{\text{LC}}$, $V_{\text{contact}}^{\text{LC}}$ and $S_{\text{face}}^{\text{LC}}$ in terms of particle radius R and contact displacement γ for all contacts under hydrostatic loading and primary contacts under die loading configuration.

Table 2.3. Expressions for various volume and surface quantities in the minimum $\bar{H}$ condition given by Eq. (2.28) for all contacts under hydrostatic and primary contacts under die loading configuration.

	DC	HC
$V_{\text{voro}}^{\text{LC}}$	$8R^2 \left(R - \gamma/2 \right)$	$8 \left(R - \gamma/2 \right)^3$
$V_{\text{contact}}^{\text{LC}}$	$(4/3)R^2 \left(R - \gamma/2 \right)$	$(4/3) \left(R - \gamma/2 \right)^3$
$S_{\text{face}}^{\text{LC}}$	$4R^2$	$4 \left(R - \gamma/2 \right)^2$

Fig. 2.17 shows the values of Γ obtained from FE simulations of die (primary contacts) and hydrostatic loading conditions, plotted against material parameter λ. From the figure, it is evident that Γ has a weak dependence on both material properties and loading condition, which results from the material and loading dependence of the contact area. We neglect these weak effects by proposing a value of Γ averaged across all the obtained numerical values for die and hydrostatic loading conditions, which is $\Gamma = 0.0593$.

Using Eq. (2.28), a detailed derivation of the solution of $\gamma|_{\bar{H}_{\min}}$ for primary contacts of die ($\gamma^{\mathrm{DC}}|_{\bar{H}_{\min}}$) and all contacts of hydrostatic ($\gamma^{\mathrm{HC}}|_{\bar{H}_{\min}}$) conditions is presented in C. It essentially entails substituting various volume and surface quantities (V_{particle}, $V_{\mathrm{voro}}^{\mathrm{LC}}$, $V_{\mathrm{contact}}^{\mathrm{LC}}$ and $S_{\mathrm{face}}^{\mathrm{LC}}$), and contact area $S_{\mathrm{contact}}^{\mathrm{LC}} = \pi a^2$ in Eq. (2.28) with their respective expressions for die and hydrostatic conditions to finally obtain a solvable quintic in terms of the unknown variable $\gamma|_{\bar{H}_{\min}}$.

As discussed previously, the parameter p governs the minimum value of normalized hardness, i.e., $\bar{H}_{\min}$. For the case of simple loading configuration, the contact pressure
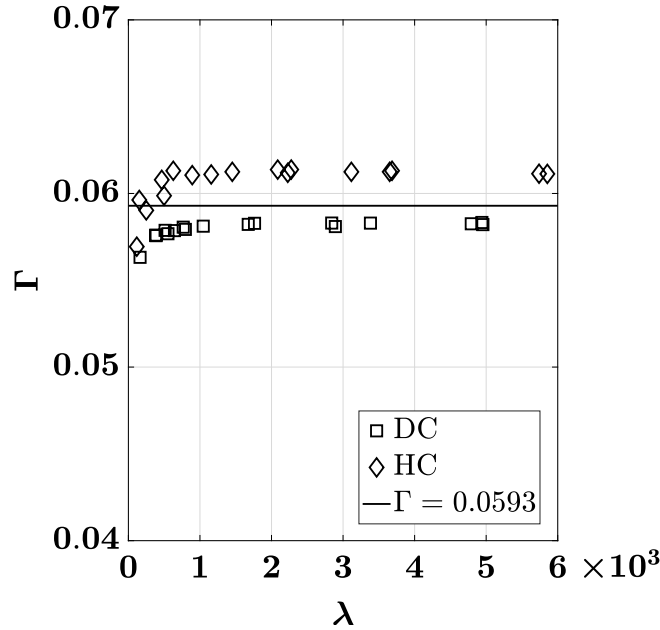
Fig.2.17. Plot of Γ values against material parameter λ for die (primary contacts) and hydrostatic loading conditions. Discrete values correspond to values obtained from FE data, while the solid plot corresponds to the average Γ value determined for the confined loading conditions.

approaches material's yield strength, and hence $\bar{H}_{\min}^{\mathrm{SC}} = 1$ at $\gamma^{\mathrm{SC}}|_{\bar{H}_{\min}} = R_1 + R_2 = 2R$. Consequently, using Eqs. (2.25) and (2.26), we have

$$\bar{H}_{\min}^{\mathrm{SC}} = \bar{H}_{\max} - p^{\mathrm{SC}} \left[\tanh\left\{ q\left(1 - \frac{\gamma|_{\bar{H}_{\max}}}{2R} \right) \right\} \cos\left\{ \left(1 - \frac{\gamma|_{\bar{H}_{\max}}}{2R} \right) - s(2R, q) \right\} \right]^r = 1 \quad (2.31)$$

Rearranging the above equation, we get

$$p^{\mathrm{SC}} = \frac{\bar{H}_{\max} - 1}{\left[\tanh\left\{ q\left(1 - \frac{\gamma|_{\bar{H}_{\max}}}{2R} \right) \right\} \cos\left\{ \left(1 - \frac{\gamma|_{\bar{H}_{\max}}}{2R} \right) - s(2R, q) \right\} \right]^r} \quad (2.32)$$
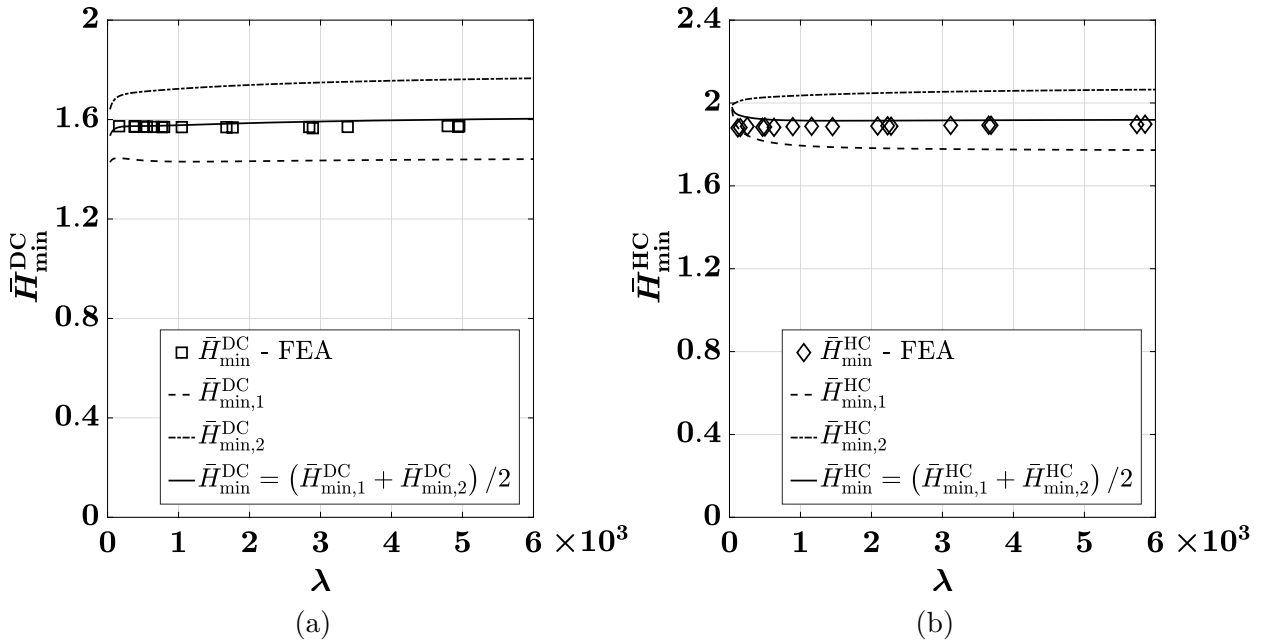
Fig.2.18. Plots of $\bar{H}_{\min}^{\mathrm{LC}}$ against material parameter λ for (a) die and (b) hydrostatic loading conditions. Discrete plots (squares for die and diamonds for hydrostatic) represent values obtained from FE simulation data. $\bar{H}_{\min,1}^{\mathrm{LC}}$ and $\bar{H}_{\min,2}^{\mathrm{LC}}$ are represented by dashed and dashed-dotted curves respectively. The analytical value of $\bar{H}_{\min}^{\mathrm{LC}}$, given by the average of $\bar{H}_{\min,1}^{\mathrm{LC}}$ and $\bar{H}_{\min,2}^{\mathrm{LC}}$, is represented by a solid curve.

For die and hydrostatic loading conditions, determination of $\bar{H}_{\min}$ is not straightforward, since the contact pressure starts rising at $\gamma = \gamma^{\mathrm{LC}}|_{\bar{H}_{\min}}$ (LC→{DC, HC}) before reaching the material's yield strength. However, two prospective values of $\bar{H}_{\min}$ can be obtained from

different analysis. The first value is determined as the value of $\bar{H}$ for the simple loading case at $\gamma^{\text{LC}}|_{\bar{H}_{\text{min}}}$, i.e.

$$
\begin{aligned}
\bar{H}^{\text{LC}}_{\text{min},1} = \bar{H}_{\text{max}} - p^{\text{SC}} & \left[\tanh\left\{ q \left(\frac{\gamma^{\text{LC}}|_{\bar{H}_{\text{min}}} - \gamma|_{\bar{H}_{\text{max}}}}{2R} \right) \right\} \right. \\
& \left. \times \cos\left\{ \left(\frac{\gamma^{\text{LC}}|_{\bar{H}_{\text{min}}} - \gamma|_{\bar{H}_{\text{max}}}}{2R} \right) - s(2R, q) \right\} \right]^r
\end{aligned}
\tag{2.33}
$$

Considering that the initial evolution of normalized hardness during the plastic regime is similar for all loading conditions, a second prospective value of $\bar{H}_{\text{min}}$ can be evaluated by determining an intermediate value of p^{LC}, such that the slope of $\bar{H}^{\text{LC}}$ for die and hydrostatic cases is equal to the slope of $\bar{H}^{\text{SC}}$ for the simple case at their points of inflection, i.e. at the point where the second derivative of $\bar{H}$ with respect to $\gamma/(R_1 + R_2)$ $(= \gamma/2R)$ is zero. This inflection point is evident in the $\bar{H}$ vs. $\gamma/2R$ curves obtained from FE simulations for all loading conditions (Figures 2.9a, 2.10a and 2.11a) during the initial softening response, when the curve changes from *concave donward* to *concave upward*. A detailed approximate solution for this point, denoted by the contact deformation $\gamma^{\text{LC}}|_{\bar{H}=0}/2R$ (LC→{SC, DC, HC}) at the point, is presented in D, where the highly nonlinear equation $\bar{H} = 0$ is solved using Taylor series expansion. The approximate solution is obtained as

$$
\frac{\gamma^{\text{LC}}|_{\bar{H}=0}}{2R} \simeq \frac{\gamma|_{\bar{H}_{\text{max}}}}{2R} + \frac{3r\tan\left\{ s(\gamma^{\text{LC}}|_{\bar{H}_{\text{min}}}, q) \right\} + \left[3(2q^2 + 3)(r-1)(2r+1) + 9(2r^2 - 1)\tan^2\left\{ s(\gamma^{\text{LC}}|_{\bar{H}_{\text{min}}}, q) \right\} \right]^{1/2}}{(2q^2 + 3)(2r+1) + 3(r+1)\tan^2\left\{ s(\gamma^{\text{LC}}|_{\bar{H}_{\text{min}}}, q) \right\}}
\tag{2.34}
$$

By equating the slope of $\bar{H}^{\mathrm{LC}}$ (LC→{DC, HC}) at $\gamma^{\mathrm{LC}}|_{\bar{H}=0}/2R$ to the slope of $\bar{H}^{\mathrm{SC}}$ at $\gamma^{\mathrm{SC}}|_{\bar{H}=0}/2R$, and rearranging the equation, we obtain the intermediate value of p^{LC} (LC→{DC, HC}), denoted by p_o^{LC}, as

$$
p_o^{\mathrm{LC}} = p^{\mathrm{SC}} \left[\frac{2q\mathrm{csch}\left\{2q\left(\frac{\gamma^{\mathrm{SC}}|_{\bar{H}=0}-\gamma|_{\bar{H}_{\mathrm{max}}}}{2R}\right)\right\} - \tan\left\{\left(\frac{\gamma^{\mathrm{SC}}|_{\bar{H}=0}-\gamma|_{\bar{H}_{\mathrm{max}}}}{2R}\right) - s(2R,q)\right\}}{2q\mathrm{csch}\left\{2q\left(\frac{\gamma^{\mathrm{LC}}|_{\bar{H}=0}-\gamma|_{\bar{H}_{\mathrm{max}}}}{2R}\right)\right\} - \tan\left\{\left(\frac{\gamma^{\mathrm{LC}}|_{\bar{H}=0}-\gamma|_{\bar{H}_{\mathrm{max}}}}{2R}\right) - s(\gamma^{\mathrm{LC}}|_{\bar{H}_{\mathrm{min}}},q)\right\}} \right]
$$
$$
\times \left[\frac{\tanh\left\{q\left(\frac{\gamma^{\mathrm{SC}}|_{\bar{H}=0}-\gamma|_{\bar{H}_{\mathrm{max}}}}{2R}\right)\right\} \times \cos\left\{\left(\frac{\gamma^{\mathrm{SC}}|_{\bar{H}=0}-\gamma|_{\bar{H}_{\mathrm{max}}}}{2R}\right) - s(2R,q)\right\}}{\tanh\left\{q\left(\frac{\gamma^{\mathrm{LC}}|_{\bar{H}=0}-\gamma|_{\bar{H}_{\mathrm{max}}}}{2R}\right)\right\} \times \cos\left\{\left(\frac{\gamma^{\mathrm{LC}}|_{\bar{H}=0}-\gamma|_{\bar{H}_{\mathrm{max}}}}{2R}\right) - s(\gamma^{\mathrm{LC}}|_{\bar{H}_{\mathrm{min}}},q)\right\}} \right]^{r}
$$

(2.35)

The second value of $\bar{H}_{\mathrm{min}}$ at $\gamma^{\mathrm{LC}}|_{\bar{H}_{\mathrm{min}}}$ is then given by

$$
\bar{H}_{\mathrm{min},2}^{\mathrm{LC}} = \bar{H}_{\mathrm{max}} - p_o^{\mathrm{LC}} \left[\tanh\left\{q\left(\frac{\gamma^{\mathrm{LC}}|_{\bar{H}_{\mathrm{min}}} - \gamma|_{\bar{H}_{\mathrm{max}}}}{2R}\right)\right\} \right.
$$
$$
\left. \times \cos\left\{\left(\frac{\gamma^{\mathrm{LC}}|_{\bar{H}_{\mathrm{min}}} - \gamma|_{\bar{H}_{\mathrm{max}}}}{2R}\right) - s(\gamma^{\mathrm{LC}}|_{\bar{H}_{\mathrm{min}}},q)\right\} \right]^{r}
$$

(2.36)
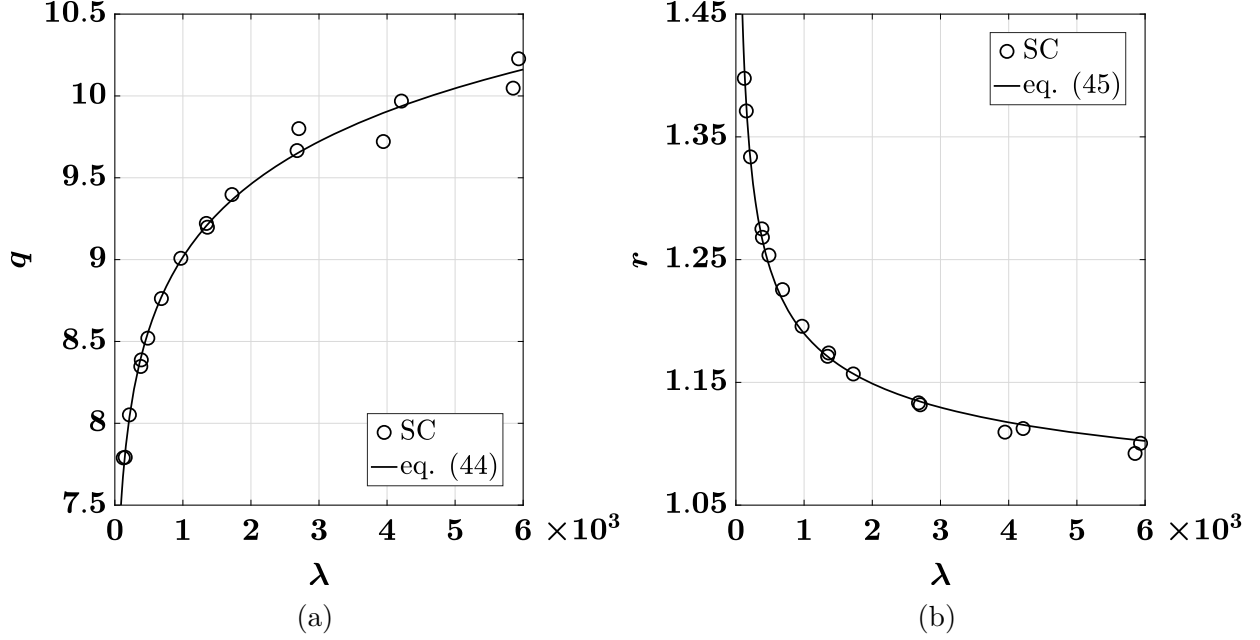
Fig.2.19. Estimation of material-dependent parameters (a) q and (b) r as functions of parameter λ for normalized hardness $\bar{H}^{\text{fp}}$ in the plastic regime. Plotted discrete values correspond to values obtained from FE data, while solid curves correspond to relationships obtained from curve fitting.

Fig. 2.18 shows the plots of $\bar{H}_{\text{min}}^{\text{LC}}$ for die and hydrostatic loading conditions against material parameter λ. The discrete values (square plots for die and diamond plots for hydro) are obtained from FE simulation data, while $\bar{H}_{\text{min},1}^{\text{LC}}$ (dashed curve) and $\bar{H}_{\text{min},2}^{\text{LC}}$ (dashed-dotted curve) are plotted using Eqs. (2.33) and (2.36) respectively for permissible values of $\lambda \geq 22.08$. From the figure, it is evident that $\bar{H}_{\text{min},1}^{\text{LC}}$ undepredicts the numerical values of $\bar{H}_{\text{min}}^{\text{LC}}$, while $\bar{H}_{\text{min},2}^{\text{LC}}$ overpredicts the values. An average of the two prospective values, plotted as a solid curve in the figure, accurately predicts the minimum normalized hardness for both confined loading conditions. Therefore, we represent $\bar{H}_{\text{min}}^{\text{LC}}$ as

$$\bar{H}_{\text{min}}^{\text{LC}} = \frac{\bar{H}_{\text{min},1}^{\text{LC}} + \bar{H}_{\text{min},2}^{\text{LC}}}{2} \tag{2.37}$$

Consequently, using Eqs. (2.25) and (2.26), parameter p^{LC} (LC$\to$\{DC, HC\}) is given by

$$p^{\text{LC}} = \frac{\bar{H}_{\text{max}} - \bar{H}_{\text{min}}^{\text{LC}}}{\left[\tanh\left\{q\left(\frac{\gamma^{\text{LC}}|_{\bar{H}_{\text{min}}} - \gamma|_{\bar{H}_{\text{max}}}}{2R}\right)\right\}\cos\left\{\left(\frac{\gamma^{\text{LC}}|_{\bar{H}_{\text{min}}}\gamma|_{\bar{H}_{\text{max}}}}{2R}\right) - s(\gamma^{\text{LC}}|_{\bar{H}_{\text{min}}}, q)\right\}\right]^r} \tag{2.38}$$

The remaining parameters q and r, determined to be material-dependent parameters, are calibrated from the $\bar{H}$ vs. $\gamma/2R$ FE simulation data of the simple loading case. Fig. 2.19 shows the plots of calibrated q and r values against material parameter λ. From fitting of the plotted values, we propose the following relationships for q and r with λ

$$q = 14.1819 \tanh\left(0.3729\lambda^{0.1013}\right) \tag{2.39}$$

$$r = \exp\left(\frac{1.6199}{\lambda^{0.3232}}\right) \tag{2.40}$$

For confined loading conditions, following the attainment of a minimum normalized hardness $\bar{H}_{\min}^{\mathrm{LC}}$ at contact deformation $\gamma^{\mathrm{LC}}|_{\bar{H}_{\min}}$, the contact pressure rises steadily during the 'low compressibility' regime. During this regime, contact behavior is heavily dependent on the loading condition due to significant contact interactions. Therefore, contacts in this regime cannot be treated independent of each other; rather, the contact behavior should be directly related to the overall particle response under compression. With this consideration, we propose to model contact response in this regime as a function of the relative density of the vornoi cell, ρ_V^{LC}, where the normalized hardness $\bar{H}$ is given by

$$\bar{H}^{\mathrm{lc}} = \bar{H}_{\min}^{\mathrm{LC}} - u \ln\left\{1 - l\left(\frac{\chi^{\mathrm{LC}} - \chi^{\mathrm{LC}}|_{\bar{H}_{\min}}}{\chi_{\mathrm{zp}}^{\mathrm{LC}} - \chi^{\mathrm{LC}}|_{\bar{H}_{\min}}}\right)^2\right\} \tag{2.41}$$

where the superscript "lc" denotes the 'low compressibility' regime, u and l are the model parameters and $\chi^{\mathrm{LC}} = 1/\rho_V^{\mathrm{LC}} = \left(V_{\mathrm{voro}}^{\mathrm{LC}}/V_{\mathrm{particle}}\right)$ is the inverse of the relative density. Using the expressions for $V_{\mathrm{voro}}^{\mathrm{LC}}$ in terms of particle radius R and contact displacement γ from Table 2.3, and $V_{\mathrm{particle}} = (4/3)\pi R^3$, the contact deformation $\gamma^{\mathrm{LC}}/2R$ (LC $\rightarrow$ {DC, HC}) in terms of χ^{LC} is given by

$$\frac{\gamma^{\mathrm{DC}}}{2R} = 1 - \frac{\pi\chi^{\mathrm{DC}}}{6} \ , \quad \frac{\gamma^{\mathrm{HC}}}{2R} = 1 - \left(\frac{\pi\chi^{\mathrm{HC}}}{6}\right)^{1/3} \tag{2.42}$$

Additionally, $\chi^{\mathrm{LC}}|_{\bar{H}_{\min}}$ is the value of χ attained at $\bar{H}_{\min}^{\mathrm{LC}}$, while $\chi_{\mathrm{zp}}^{\mathrm{LC}}$ is the value of χ attained at the zero porosity limit (Tsigginos et al., 2015), which is the limit of full closure of porosity and

beyond which the contact pressure is governed by the particle's elastic volume compressibility. It is given by

$$\chi_{\text{zp}}^{\text{LC}} = \frac{V_{\text{particle}} - V_{\text{el}}^{\text{LC}}}{V_{\text{particle}}} \tag{2.43}$$

where $V_{\text{el}}^{\text{LC}}$ is the elastic reduction in particle volume until the zero porosity limit is reached. It is important to note that the normalized hardness given by Eq. (2.41) attains its minimum value equal to $\bar{H}_{\text{min}}^{\text{LC}}$ at $\chi^{\text{LC}} = \chi^{\text{LC}}|_{\bar{H}_{\text{min}}}$, making it C^1 continuous with the normalized hardness in the plastic regime given by Eq. (2.25) .

The contact pressure beyond the zero porosity limit is given by the elastic volumetric stress on the particle. Therefore, the normalized hardness in this regime is given by

$$\bar{H}^{\text{ev}} = \frac{B}{\sigma_y}\left(1 - \frac{V_{\text{voro}}}{V_{\text{particle}}}\right) = \zeta(1 - \chi^{\text{LC}}) \tag{2.44}$$

where the superscript "ev" denotes the elastic volumetric regime. By equating the value and slope of $\bar{H}^{\text{gh}}$ given by Eq. (2.41) and $\bar{H}^{\text{ev}}$ given by (2.44) at $\chi^{\text{LC}} = \chi_{\text{zp}}^{\text{LC}}$ to achieve C^1 continuity between the contact formulations for $\bar{H}$ in the 'low compressibility' and elastic volumetric regimes, we obtain the following relationships between model parameters u and l and elastic volume reduction $V_{\text{el}}^{\text{LC}}$

$$u = \frac{V_{\text{particle}}\bar{H}_{\text{min}}^{\text{LC}} - \zeta V_{\text{el}}^{\text{LC}}}{V_{\text{particle}}\ln(1 - l)} \tag{2.45}$$

$$V_{\text{el}}^{\text{LC}} = \frac{V_{\text{particle}}\left\{2l\bar{H}_{\text{min}}^{\text{LC}} + \zeta(1 - \chi^{\text{LC}}|_{\bar{H}_{\text{min}}})(1 - l)\ln(1 - l)\right\}}{\zeta\left\{2l + (1 - l)\ln(1 - l)\right\}} \tag{2.46}$$

From the above equations, it is evident that u and $V_{\text{el}}^{\text{LC}}$ can be evaluated from a known value of l. Fig. 2.20 shows a plot of the natural log of $(1 - l)$ against material parameter ζ, where the l values are calibrated from $\bar{H}$ vs. $\gamma/2R$ FE simulation data of die and hydrostatic loading cases. It is interesting to note that the parameter l is independent of the loading condition, since the $\ln(1 - l)$ values for both die and hydrostatic loading conditions fall on a single trend curve that is a function of ζ. Therefore, it is fair to conclude that l is a material-dependent parameter.
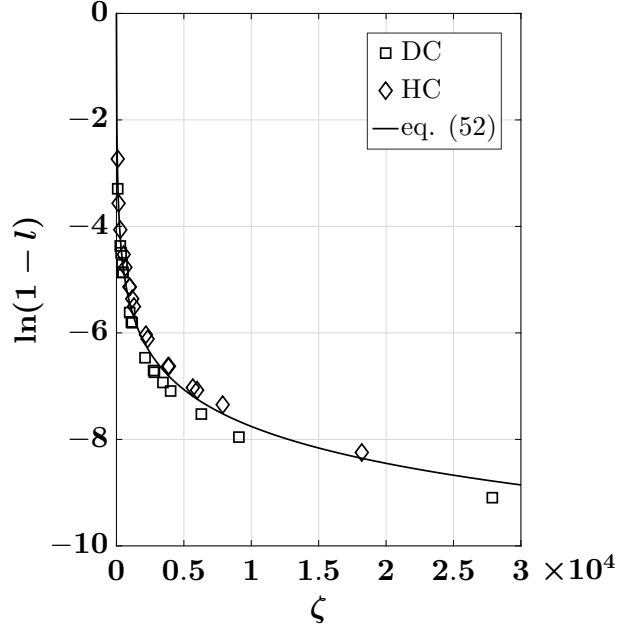
Fig.2.20. Estimation of model parameter l as a function of material parameter ζ for normalized hardness $\bar{H}^{\text{lc}}$ in the 'low compressibility' regime. Plotted discrete values correspond to $\ln(1-l)$ values obtained from calibration of FE data, while the solid curve represents the relationship obtained from curve fitting.

From curve fitting of the plotted values, we propose the following relationship between l and ζ

$$\begin{aligned}
\ln(1-l) &= \ln\left(\frac{1}{1+0.2335\zeta}\right) \\
&\implies l = 1 - \left(\frac{1}{1+0.2335\zeta}\right)
\end{aligned} \tag{2.47}$$

To conclude the analysis, we provide below a summarized form of the semi-mechanistic contact law for the normalized hardness $\bar{H}$

$$
\bar{H} = \begin{cases}
= \bar{H}^{\mathrm{e}} = \frac{2}{3\pi}\lambda\mathbb{A}^{1/2}\gamma^{1/2} & \gamma \in [0, \gamma_y] \\[3mm]
= \bar{H}^{\mathrm{ep}} = \bar{H}_{\max} - c_1 \left[\ln\left(\frac{\gamma|_{\bar{H}_{\max}}}{\gamma}\right)\right]^{c_2} & \gamma \in \left(\gamma_y, \gamma|_{\bar{H}_{\max}}\right] \\[3mm]
= \bar{H}^{\mathrm{fp}} = \bar{H}_{\max} - p^{\mathrm{LC}}\left[\tanh\left\{q\left(\frac{\gamma-\gamma|_{\bar{H}_{\max}}}{2R}\right)\right\}\right. & \gamma \in \left(\gamma|_{\bar{H}_{\max}}, \gamma^{\mathrm{LC}}|_{\bar{H}_{\min}}\right] \\[3mm]
\qquad\quad \left. \times \cos\left\{\left(\frac{\gamma-\gamma|_{\bar{H}_{\max}}}{2R}\right) - s(\gamma^{\mathrm{LC}}|_{\bar{H}_{\min}}, q)\right\}\right]^r & \mathrm{LC} \to \{\mathrm{SC}, \mathrm{DC}, \mathrm{HC}\} \\[3mm]
= \bar{H}^{\mathrm{lc}} = \bar{H}_{\min}^{\mathrm{LC}} - u\ln\left\{1 - l\left(\frac{\chi^{\mathrm{LC}}-\chi^{\mathrm{LC}}|_{\bar{H}_{\min}}}{\chi_{\mathrm{zp}}^{\mathrm{LC}}-\chi^{\mathrm{LC}}|_{\bar{H}_{\min}}}\right)^2\right\} & \gamma \in \left(\gamma^{\mathrm{LC}}|_{\bar{H}_{\min}}, \gamma_{\mathrm{zp}}^{\mathrm{LC}}\right] \\[3mm]
& \mathrm{LC} \to \{\mathrm{DC}, \mathrm{HC}\} \\[3mm]
= \bar{H}^{\mathrm{ev}} = \zeta(1 - \chi^{\mathrm{LC}}) & \gamma \in \left(\gamma_{\mathrm{zp}}^{\mathrm{LC}}, \infty\right) \\[3mm]
& \mathrm{LC} \to \{\mathrm{DC}, \mathrm{HC}\}
\end{cases}
\tag{2.48}
$$

2.5   Verification of the semi-mechanistic contact law

The semi-mechanistic contact formulation developed in the previous section was verified by comparing the contact law predictions of normalized contact radius (a/R), normalized contact pressure or hardness $(\bar{H} = P/\sigma_y\pi a^2)$ and normalized contact force $(P/\sigma_y\pi R^2)$ with data obtained from FE simulations. Figures 2.21, 2.22 and 2.23 present this comparison for simple, die (primary contacts) and hydrostatic loading configurations respectively. To verify the material property dependence of the contact formulation, comparative plots for all loading configurations are provided for the lowest and the highest value of material parameter λ obtained from the space-filling design. The figures show an excellent agreement between the numerical FE data and the analytical contact law predictions, with an accurate representation of material and loading condition - dependence of the contact behavior.

(a)

(b)

(c)
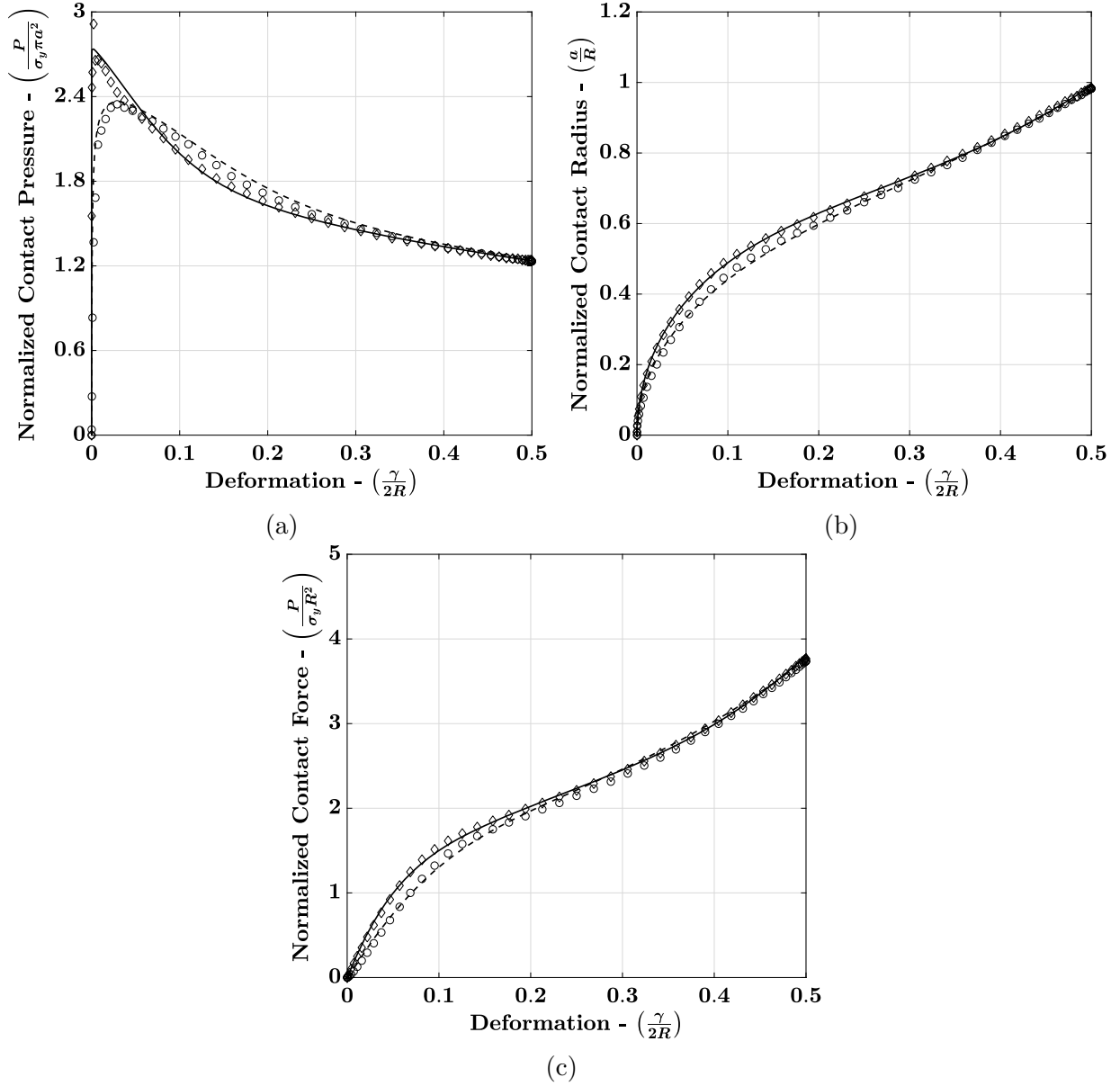
Fig.2.21. Comparison of the predictions of normalized (a) contact pressure, (b) contact radius, and (c) contact force evolution with respect to contact deformation from the proposed semi-mechanistic contact formulation with FE simulation data for a particle under simple compression. FE data for the lowest value of $\lambda = 123.41$ obtained from space-filling design are denoted by circles, with corresponding contact law predictions denoted by a dashed curve. FE data with the highest value of $\lambda = 5933.40$ are denoted by diamonds, with corresponding contact law predictions denoted by a solid curve.

(a)

(b)

(c)

Fig.2.22. Comparison of the predictions of normalized (a) contact pressure, (b) contact radius, and (c) contact force evolution with respect to contact deformation from the proposed semi-mechanistic contact formulation with FE simulation data for primary contacts of a particle under die compression. FE data for the lowest value of $\lambda = 163.08$ obtained from space-filling design are denoted by circles, with corresponding contact law predictions denoted by a dashed curve. FE data with the highest value of $\lambda = 4954.40$ are denoted by diamonds, with corresponding contact law predictions denoted by a solid curve.

61

(a)

(b)

(c)

Fig.2.23. Comparison of the predictions of normalized (a) contact pressure, (b) contact radius, and (c) contact force evolution with respect to contact deformation from the proposed semi-mechanistic contact formulation with FE simulation data for a particle under hydrostatic compression. FE data for the lowest value of $\lambda = 117.24$ obtained from space-filling design are denoted by circles, with corresponding contact law predictions denoted by a dashed curve. FE data with the highest value of $\lambda = 5854.69$ are denoted by diamonds, with corresponding contact law predictions denoted by a solid curve.

2.6 Preliminary semi-mechanistic analysis of the secondary contacts of die loading configuration

For the case of die loading configuration, we have shown the evolution of contact behavior at the lateral or 'secondary' contacts from the FE simulations presented in Section 2.3. These contacts, despite being subjected to zero applied or 'local' deformation, develop solely due to the lateral or 'nonlocal' deformation of the particle resulting from axial compression. In this section, we attempt to lay the foundation of a nonlocal contact formulation capable of predicting such contact behavior by proposing semi-mechanistic laws relating the deformation at primary and secondary contacts.

To obtain an estimate of the lateral deformation, we utilize the FE simulations for the simple loading configuration and post-process the average nodal displacements at the lateral edge of the $(1/8)^{\text{th}}$ sphere (Fig. 2.24). Therefore, for a displacement $\gamma/2$ at the particle-plate axial contact (γ for a two-particle contact), we obtain an average nodal displacement of $\gamma_{\text{s}}/2$ at the lateral edge, where the subscript 's' denotes the equivalent displacement at the secondary contact in the die loading configuration. It is important to note that, according to
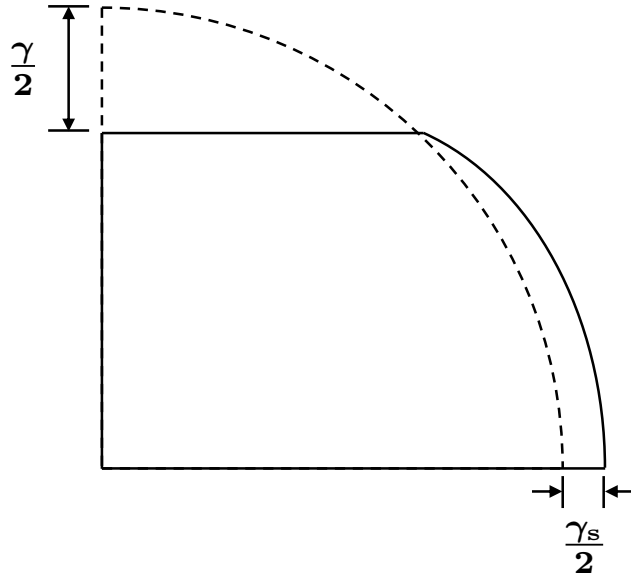
Fig.2.24. Schematic of the simple compression of $(1/8)^{\text{th}}$ sphere, showing an axial contact displacement of $\gamma/2$ resulting in a lateral edge displacement of $\gamma_{\text{s}}/2$.

63

the nonlocal contact formulation (ref. (M. Gonzalez & Cuitiño, 2012, 2016) and (Agarwal & Gonzalez, 2018)), each particle contact acquires nonlocal displacement contributions from all other contacts on the particle. Therefore, as the lateral secondary displacements γ_s evolve and become larger, their nonlocal contributions to the primary and other secondary contacts become significant. Since the development of a complete nonlocal contact formulation for elasto-plastic particles is beyond the scope of this paper, we restrict our estimation of the secondary displacements to the small deformation regime to safely neglect any nonlocal contributions from the secondary contacts.
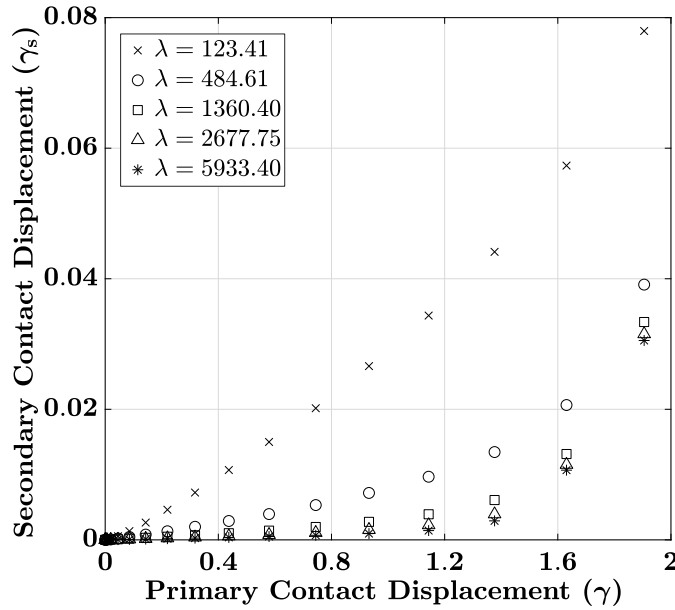
Fig.2.25. Plots of lateral secondary contact displacement (γ_s) vs. axial primary contact displacement (γ) obtained from FE simulations of the simple loading configuration. Plots are depicted for 5 out of the 17 material properties obtained from the space-filling design, ranging from minimum to maximum value of the material parameter λ. The units of displacement on both axes is millimeters (mm).

From the observation of FE simulation results of normalized hardness for secondary die contacts (Fig. 2.12a), we find that the contact behavior remains within the small deformation elastic-plastic regime until the primary contact deformation $\gamma/2R$ reaches 0.1. Therefore, the lateral secondary displacements are evaluated until the primary contact displacement reaches $\gamma = 0.1 \times 2R = 2$ mm for $R = 10$ mm. The obtained displacements are plotted in

Fig. 2.25 for 5 out of the 17 material properties for simple configuration obtained from the sapce filling design, ranging from minimum to the maximum value of material parameter λ. From the figure, we observe that the evolution of lateral displacement follows a power law, with the rate of evolution increasing with increasing material compliance (decreasing λ). Accordingly, we propose the following relationship between the secondary and primary contact displacement

$$\gamma_s = \tau \gamma^\omega \tag{2.49}$$

where τ and ω are material-dependent parameters. Fig. 2.26 shows a plot of the discrete values of these parameters against material parameter λ, obtained by fitting the above relationship to the secondary vs. primary displacement data for all 17 material properties. From curve fitting of these calibrated values, we propose the following relationship for τ and ω with λ

$$\tau = \frac{1}{1480.8863 \tanh\left\{(5.0261 \times 10^{-5}) \cdot (\lambda^{1.2889})\right\}} \tag{2.50}$$

$$\omega = 5.7775 \tanh\left\{0.0159\left(\lambda^{0.6146}\right)\right\} \tag{2.51}$$
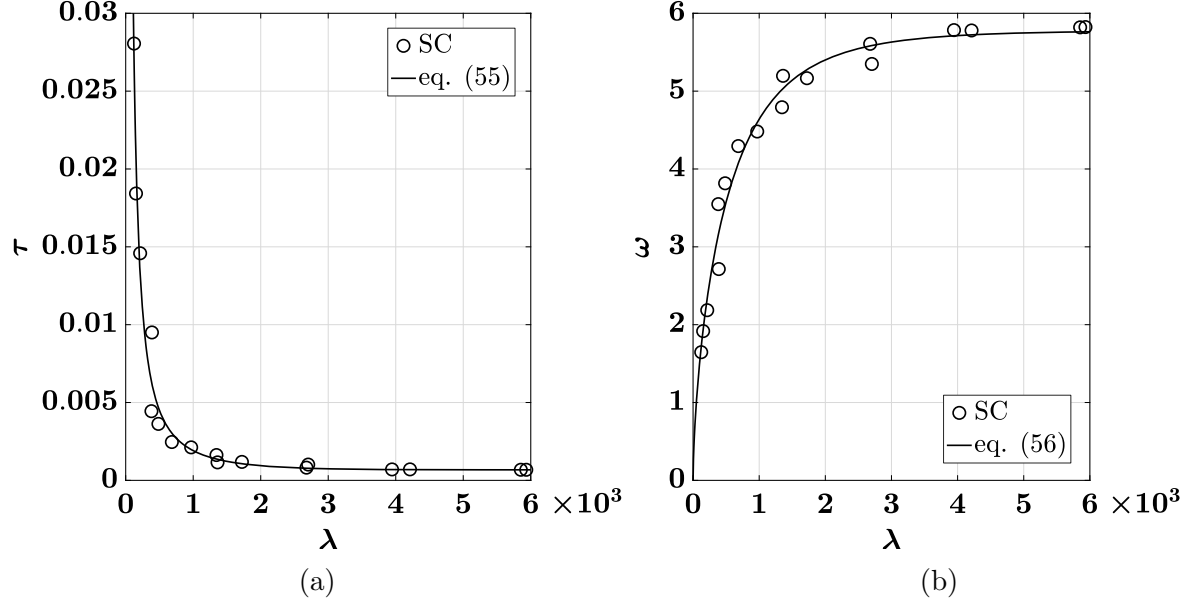
Fig.2.26. Estimation of material-dependent parameters (2.26a) τ and (2.26b) ω as functions of parameter λ for the relationship between secondary and primary contact displacements γ_s and γ. Plotted discrete values correspond to values obtained from FE data, while solid curves correspond to relationships obtained from curve fitting.

The above relationships are also plotted in Fig. 2.26, and provide excellent estimates of the calibrated parameter values. Finally, by using these relationships in the $\gamma_s - \gamma$ power law given by Eq. (2.49), the evaluated secondary displacements are plotted and compared with the FE values for the minimum and miximum λ in Fig. 2.27. The figure confirms the accuracy of the proposed power law, with an excellent agreement obtained between the modeled and FE results.
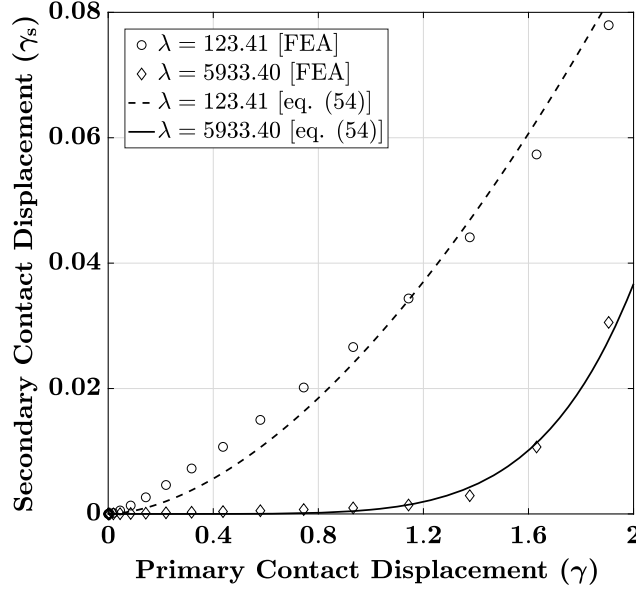
Fig.2.27. Comparison of secondary displacement (γ_s) vs. primary displacement (γ) obtained from the power law given by Eq. (2.49) and FE simulations of the simple loading configuration. Plots are depicted for minimum and maximum value of λ obtained from the space-filling design. The units of displacement on both axes is millimeters (mm).

The secondary contact displacement model from Eq. (2.49) can now be used to obtain the contact radius (Eq. (2.13)), normalized hardness (Eq. (2.15) for elastic and Eq. (2.18) for elastic-plastic regime) and contact force (Eq. (2.12)) until the primary contact deformation reaches 0.1, which denotes the limit of elastic-plastic regime for the secondary contacts.

Additionally, we have proposed in the previous section that during the 'low compressibility' regime, the contact response is a function of the overall particle compression due to significant contact interactions. Therefore, it is fair to assume that beyond the 'low compressibility' regime, all particle contacts are subjected to the same pressure, which is given by Eq. (2.41) in the 'low compressibility' regime and Eq. (2.44) in the elastic volumetric regime. For the secondary contacts, the onset of 'low compressibility' regime is predicted by using the

minimum hardness condition given by Eq. (2.28), where the product of volume and surface relative densities is given by

$$
\begin{aligned}
\rho_V^{\text{DC,contact}} \times \rho_S^{\text{DC,contact}} &= \left(\frac{V_{\text{particle}}}{V_{\text{voro}}^{\text{DC}}}\right)\left(\frac{V_{\text{contact}}^{\text{DC}}}{V_{\text{voro}}^{\text{DC}}}\right)\left(\frac{S_{\text{contact}}^{\text{DC}}}{S_{\text{face}}^{\text{DC}}}\right) \\
&= \frac{\frac{4}{3}\pi R^3}{8R^2\left(R-\frac{\gamma}{2}\right)} \times \frac{\frac{4}{3}R^2\left(R-\frac{\gamma}{2}\right)}{8R^2\left(R-\frac{\gamma}{2}\right)} \times \frac{S_{\text{contact}}^{\text{DC}}}{4R\left(R-\frac{\gamma}{2}\right)} \qquad (2.52) \\
&= \frac{\pi S_{\text{contact}}^{\text{DC}}}{144R^2\left(1-\frac{\gamma}{2R}\right)^2}
\end{aligned}
$$

The value of primary deformation $\gamma/2R$ at the onset can be obtained by interpolating the $\gamma/2R$ vs. $\rho_V^{\text{DC,contact}} \times \rho_S^{\text{DC,contact}}$ data generated by using FE values of the secondary contact area $S_{\text{contact}}^{\text{DC}}$. Fig. 2.28 presents this data for 5 out of the 17 material properties for die configuration, ranging from minimum to maximum λ. According to Eq. (2.28), the 'low compressibility' regime starts when the product of volume and surface relative densities equals $\Gamma = 0.0593$. The deformation values at the fulfillment of this condition are obtained by cubic interpolation between points on either side of the Γ value, and are listed in Table 2.4 for the five plotted material properties.
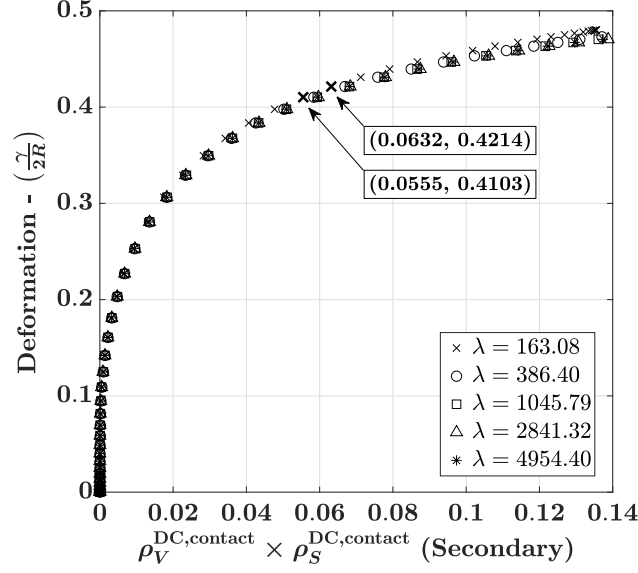
Fig.2.28. Plot of primary deformation $(\gamma/2R)$ vs. the product of volume and surface relative densities $\rho_V^{\text{DC,contact}} \times \rho_S^{\text{DC,contact}}$ for the secondary contacts of die loading configuration. Plots are depicted for 5 out of 17 material properties for die configuration, ranging from minimum to maximum value of λ. The marked points (bold cross markers) correspond to the points between which the value of $\gamma/2R$ at $\rho_V^{\text{DC,contact}}\rho_S^{\text{DC,contact}} = \Gamma = 0.0593$ is interpolated for $\lambda = 163.08$.

Table 2.4. Values of primary contact deformation $\gamma/2R$ at the onset of 'low compressibility' regime for secondary die contacts. Values are provided for 5 out of the 17 material properties for die loading configuration.

λ	$\gamma/2R$ (Low Compressibility)
163.08	0.4159
386.40	0.4115
1045.79	0.4102
2841.32	0.41
4954.40	0.4098

Observation of the large deformation normalized contact pressure response of secondary die contacts from finite element simulations (Fig. 2.13c) suggests that while the normalized hardness $\bar{H}$ at the onset of 'low compressibility' regime ($\gamma/2R \sim 0.41$ from Table 2.4) does not attain a minimum value, it does fall on an inflection point, following which the evolution

69
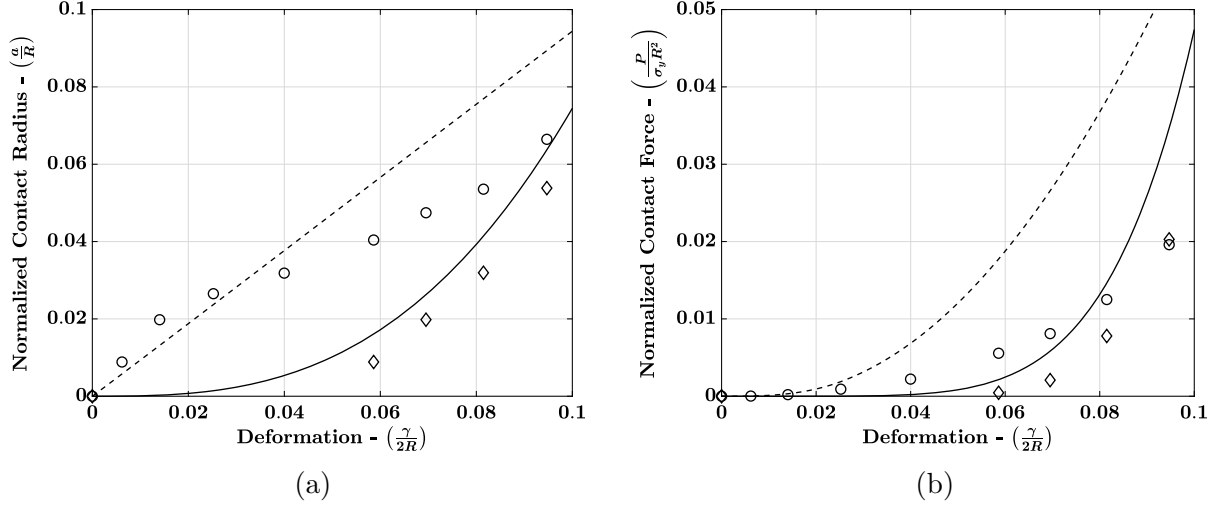
Fig.2.29. Comparison of the predictions of small-deformation normalized (a) contact radius (Eq. (2.13)) and (b) contact force (Eq. (2.12)) evolution at the secondary contacts with respect to primary contact deformation with FE simulation data for a particle under die compression. FE data for the lowest value of $\lambda = 163.08$ are denoted by circles, with corr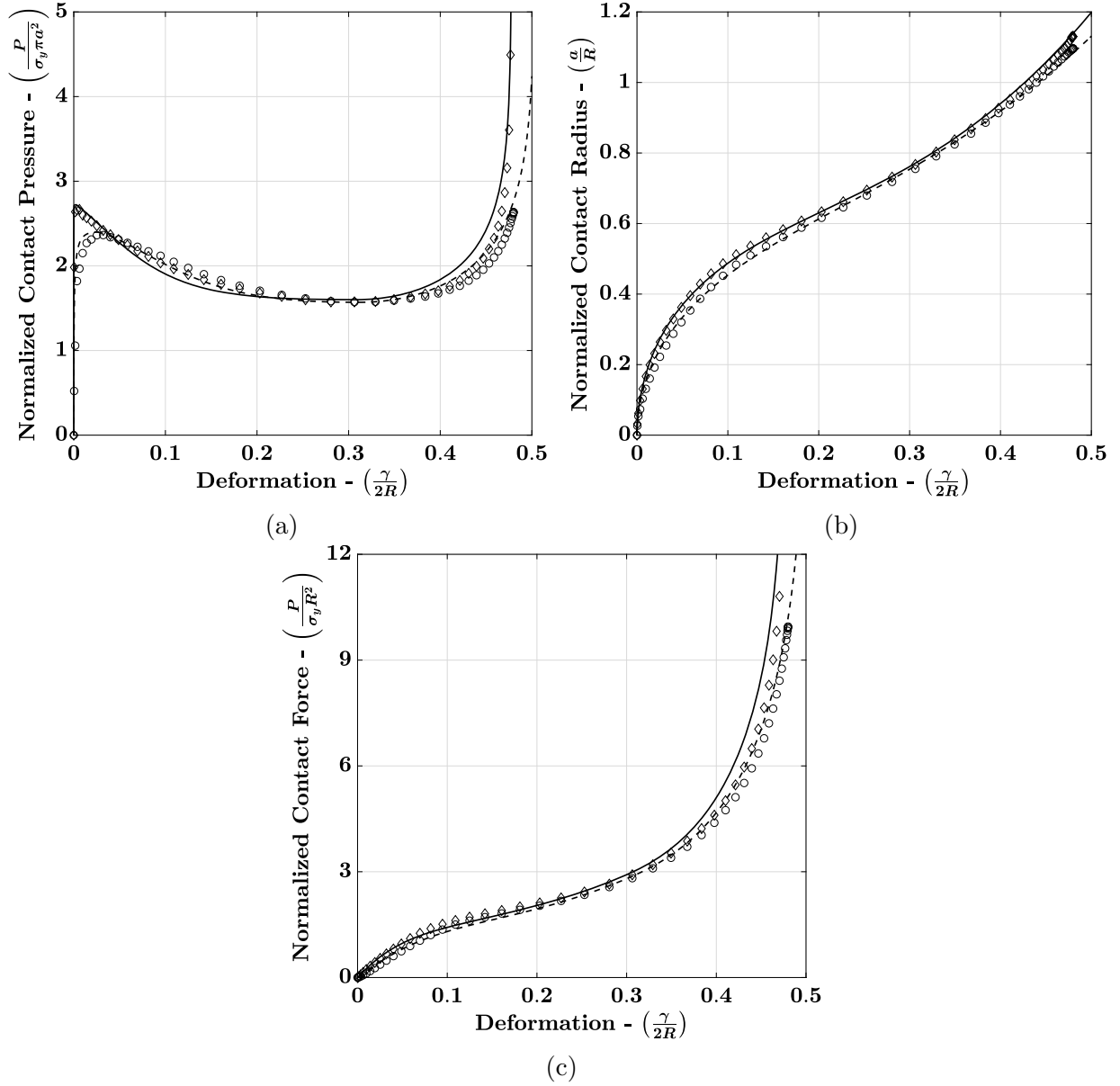esponding contact law predictions denoted by a dashed curve. FE data with the highest value of $\lambda = 4954.40$ are denoted by diamonds, with corresponding contact law predictions denoted by a solid curve.
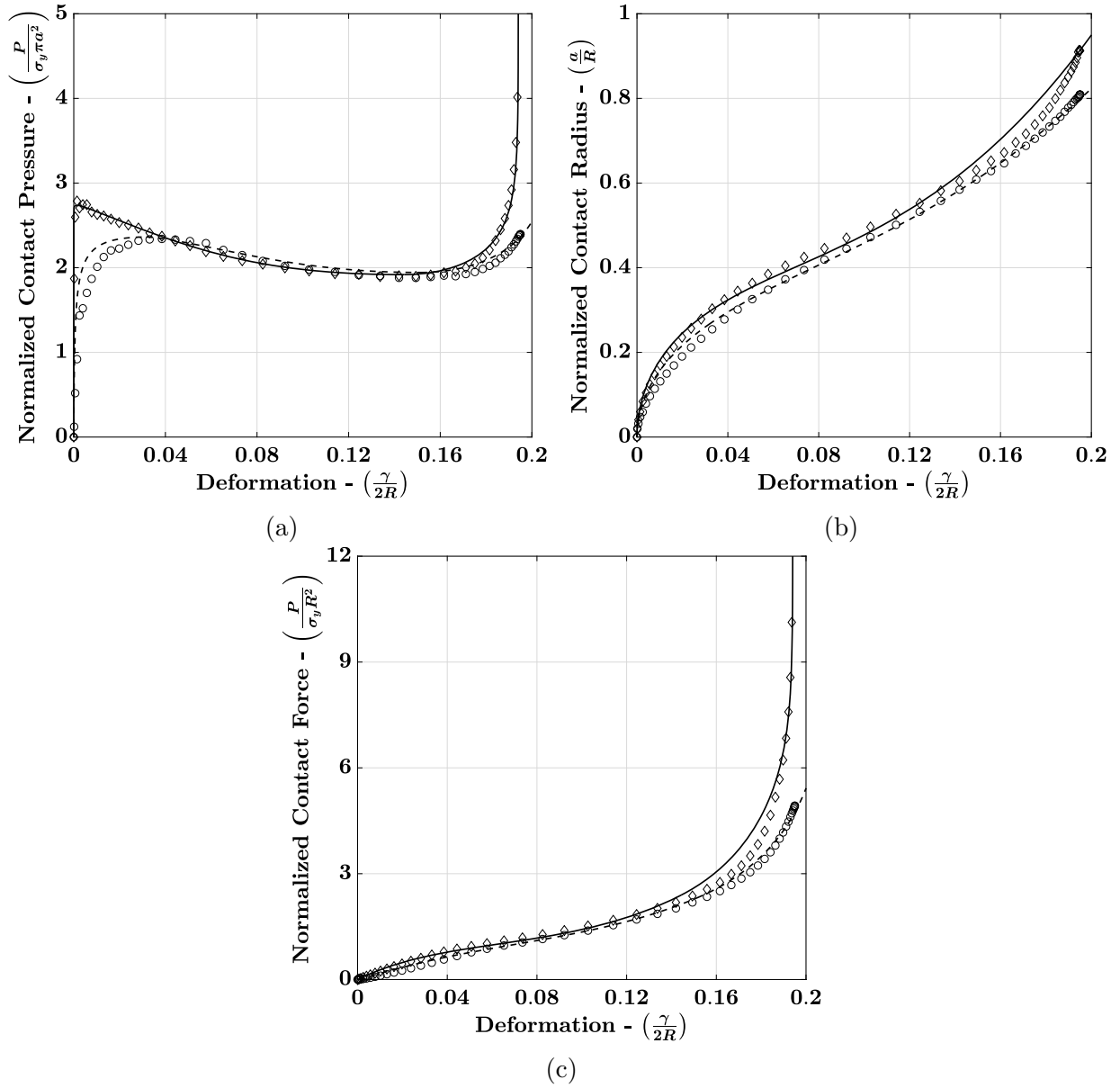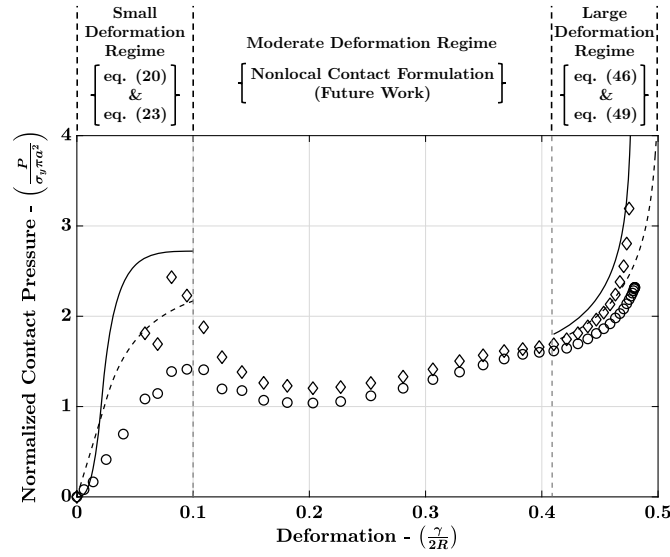

Fig.2.30. Comparison of the predictions of small and large deformation normalized hardness evolution at the secondary contacts with respect to primary contact deformation with FE simulation data for a particle under die compression. FE data for the lowest value of $\lambda = 163.08$ are denoted by circles, with corresponding contact law predictions denoted by a dashed curve. FE data with the highest value of $\lambda = 4954.40$ are denoted by diamonds, with corresponding contact law predictions denoted by a solid curve.

70

of contact pressure is visibly similar to that of the primary contacts (Fig. 2.13b). This observation confirms the accuracy of our predictions of the onset of the 'low compressibility' regime for secondary die contacts.

Fig. 2.29 presents a comparison of the predicted evolution of normalized secondary contact radius and contact force in the small-deformation (elastic and elastic-plastic) regime with the finite element simulation results. Additionally, Fig. 2.30 shows the predicted vs. FE results of the evolution of normalized hardness in both small and large (beyond 'low compressibility') deformation regimes. Comparative plots are provided for the minimum and the maximum value of λ for die configuration. Even though an excellent agreement is not achieved, the predicted results at small deformations are still comparable with the FE data and of the same order of magnitude. Concurrently, a good agreement between the predicted and FE results is obtained for normalized hardness in the large deformation regime.

2.7 Summary and discussion

We have developed a semi-mechanistic contact formulation for material and loading condition-dependent contact behavior of an elastic-perfectly plastic spherical particle, as it is compressed in a simple cubic packing under unconfined (simple axial compression) or confined (die and hydrostatic compression) loading conditions. Contact laws for the evolution of contact radius and normalized contact pressure (or hardness) have been proposed, while the contact force is efficiently determined from the product of contact pressure and area. The material-dependence is systematically incorporated in the formulation through calibration of model parameters to a set of 51 single-particle finite element simulations (17 for each of simple, die and hydrostatic loading conditions), where the diverse set of material properties is obtained from a space-filling design.

The contact radius is determined as a three-term nonlinear function of the contact displacement, where each term corresponds to the evolution of contact area during a specific deformation regime, i.e., small, moderate and large deformations. The analytical framework for the three-term function is obtained by applying the method of curvature-correction to the small-deformation similarity contact law. The normalized hardness, due to its complex

71

and distinct evolution in each deformation regime, is modeled as a piecewise differentiable function, with distinct contact laws proposed for each regime in a way that the function remains continuous and differentiable with respect to the contact deformation at all stages of particle compression. A salient feature of the proposed contact law is its capability to predict the rise in contact pressure for confined loading conditions during the 'geometrical hardening' or 'low compressibility' regime as a function of the particle's elastic compressibility, thus unraveling critical material-dependent behavior at large deformations. The capabilities of the contact formulation are successfully verified by attainment of an excellent agreement between the model and finite element predictions of the evolution of contact radius, pressure and force with contact deformation for the three considered loading configurations.

Finally, we have presented a foundational semi-mechanistic analysis of the lateral walled (secondary) contacts in the die loading configuration. The secondary contacts, despite not being subjected to any applied deformation, evolve as a result of the lateral expansion of the axially compressed particle. The induced deformation at the secondary contacts, termed as nonlocal deformation, is determined by post-processing the nodal displacements at the lateral edge of the particle from finite element simulations of the simple loading configuration. Although, this analysis is limited to small deformations to safely neglect any nonlocal contributions from the secondary contacts themselves. The relationship between primary and nonlocal secondary contact displacements is modeled as a power law, which is shown to accurately represent the material-dependent evolution of the secondary displacements. By using this relationship, the contact response is evaluated at small deformations from the proposed semi-mechanistic contact formulation. Additionally, by utilizing the assumption of equal contact pressure at all particle contacts beyond the 'low compressibility' regime, the contact pressure at large deformations for the secondary contacts is determined from the proposed normalized hardness law. A comparison of the model and finite element predictions of the secondary contact response shows that while an excellent agreement is not achieved, the model predicted response is comparable and of the same order of magnitude as the numerical FE data. With regard to this observation, it is worth mentioning that since the FE simulations performed in this study were set up for an accurate determination of the large deformation contact response, a separate finite element study with a finer mesh may be

needed for proper convergence of contact behavior at small deformations. Such a study will enable a more reliable verification of the modeled response at the secondary contacts, and is a worthwhile direction of future research.

3. SEMI-MECHANISTIC CONTACT LAW FOR LARGE DEFORMATION UNCONFINED AND CONFINED COMPRESSION OF SPHERICAL RIGID-PLASTIC PARTICLES WITH POWER-LAW HARDENING

The content of this chapter and associated appendices C and E will be submitted to International Journal of Solids and Structures.

3.1 Introduction

Compaction of granular materials and powder compaction are central to many industries, such as pharmaceutical, energy production, and agriculture. The commercial applications makes the characterization of these materials of great importance. Current research has been particularly focusing on the area of predictive modeling of mesoscopic and macroscopic behavior of powders and granular materials under confinement. The fundumental understanding of the compaction behavior allows for optimization of the performance in all applications of these materials. These materials are heterogenous in nature which greatly effects the macroscropic behavior. Mechanistic continuum modeling, on a macroscopic scale, are capable of describing microstructure evolution during compaction processes of these materials (Puri et al., 1995; Sun and Kim, 1997, Chtourou et al., 2002, Cunningham et al., 2004; DiMaggio and Sandler, 1971; Han et al., 2008; Sinha et al., 2010; Sinka et al., 2004,and A. Bakhshiani et al., 2004, 2002; Khoei et al., 2002). Such models assume the granular systems as homogenrous materials ignoring fundamental behavior at the partice-scale. These assumptions are relaxed in the use of Discrete Element Modeling (DEM), a numerical method proposed by (Cundall & Strack, 1979). DEM is a dynamic modeling approach that is capable of predicting behavior from deformation of elasto-plastic particles in powder compaction at the mesoscale (or particle-scale) (Belheine et al., 2009; Harthong et al., 2009; Jerier et al., 2011; C.L. Martin and Bouvard, 2003; C.L Martin et al., 2003; C. L. Martin et al., 2006; Rojek et al., 2016; Sheng et al., 2002; Skrinjar and Larsson, 2004). Recently, a more computationally efficient approach called discrete particle mechanics (M. Gonzalez and Cuitiño, 2016; Marcial Gonzalez, 2019;

Marcial Gonzalez et al., 2018; Poorsolhjouy and Gonzalez, 2018; Yohannes et al., 2016, 2017) has been proposed. The use of discrete modeling to describe the macroscopic behavior of granular systems during compaction depend on contact formulation between inter-particle contacts occuring prior and during compaction processes. Contact formulations describe the contact force-area-deformation relationships between inter-particles contacts. In our work, we focus on developing contact formulation for unconfined and confined compression of plastic particles with power-law hardening.

In our formulation, we adopt a rigid-plastic flow formulation considering two widely used power-law hardening behavior. We first consider the power-law from (Ludwik, 1909), where stress evolve according to the following power-law relationship

$$\sigma = \sigma_y + K\epsilon_{\mathrm{pl}}^{1/n} \tag{3.1}$$

where σ is the true stress, σ_y is the yield stress, K is the strength coefficient, $1/n$ is the hardening exponent, and ϵ_{pl} is the plastic strain determined from

$$\epsilon_{\mathrm{pl}} = \epsilon - \frac{\sigma}{E} \tag{3.2}$$

where ϵ is the total strain and E is the Young's modulus. To stay consistent with previous work on contact models for elasto-plastic spheres assuming rigid-plastic power-law hardening (Biwa & Storåkers, 1995; Tabor, 1951) and contact of inelastic solids of revolution (B. Storåkers et al., 1997), we also consider Hollomon's stress-strain power-law relationship (Hollomon, 1945)

$$\sigma = \kappa\epsilon^{1/m} \tag{3.3}$$

where κ is the strength coefficient and $1/m$ is the hardening exponent. For considering both power law relationships, Eqns.(3.1) and (3.3) are set equal to one another (Harthong et al., 2009) and the hardening properties from Eqn.(3.1) are calibrated to fit Eqn.(3.3) using least-square error optimization. In our study, the relationships from the rigid-plastic contact model proposed by Biwa and Storåkers is utilized where the contact of two spheres of radii

R_1 and R_2, strength coefficients κ_1 and κ_1, and hardening exponent $1/m$, the contact force (P)-radius (a)-displacement (γ) relationships are given by

$$P = \eta_{\mathrm{P}} a^{2 + \frac{1}{m}}$$
(3.4)

and

$$a = \left(\frac{2c^2}{\mathbb{A}} \right)^{1/2} \gamma^{1/2}$$
(3.5)

where γ is the relative displacement of the particles

$$\gamma = R_1 + R_2 - ||\mathbf{x}_1 - \mathbf{x}_2||$$
(3.6)

and geometric parameter $\mathbb{A}$ and plastic law coefficient η_{P} are given by

$$\mathbb{A} = \frac{1}{R_1} + \frac{1}{R_2}$$
(3.7)

$$\eta_{\mathrm{P}} = \pi k \mathbb{A}^{1/m} \left(\frac{1}{\kappa_1^m} + \frac{1}{\kappa_2^m} \right)^{-1/m}$$
(3.8)

with $k = 3 \times 6^{-1/m}$ and $c^2 = 1.43\mathrm{e}^{-0.97/m}$. The similarity contact law uses the assumption of independent contacts and small-strain kinematics. These assumptions make the solution of the contact law only predictable for small deformations and the solution is independent from loading configuration. Contact models must be able to predict complex behaviors of materials during moderate deformation such as softening and capture the dependence on loading configuration at large deformations. There has been a proposed semi-mechanistic DEM contact law built on curve fitting of force-deformation FE data (Harthong et al., 2009; Harthong et al., 2012), however, the contact model does not provide prediction of contact radius and there has been no extension on using the contact law for a general loading condition. Semi-analytic contact law for elasto-plastic spherical particles has been proposed by (E. Olsson & Larsson, 2016; Erik Olsson & Larsson, 2013a, 2013b) where the solution is predictive for large deformation, however,the formulation lacks prediction of the full range of hardening exponent.

76

In spite of all recent work, finding a predictive mechanistic contact law for large deformation contact behavior of elasto-plastic particles under general loading conditions is difficult. In light of this issue, we propose a semi-mechanistic contact law for plastic particles with power-law hardening under unconfined and confined loading configurations. This paper extends the efforts made towards formulating a semi-mechanistic contact law for elastic-ideally plastic particles under unconfined and confined loading configurations (Agarwal et al., 2021) to consider strain-hardening effects.

The paper is organized as follows. The rigid-plastic limit of the elastic-ideally plastic formulation is examined in Section 2.2. The space-filling design problem and finite element simulations are presented in Section 2.3. Modifications to the rigid-plastic limit of the elastic-ideally plastic formulation to consider hardening effects are discussed in Section 2.4. The predictions of the contact model are verified by making a comparison with the finite element results are presented in Section 2.5. Then in Section 2.6, the contact model is used to estimate hardening properties, contact radius, and stress response under confined loading configuration of micro-crystalline cellulose particles under large deformation using experimental data. Finally, a conclusion of the paper is presented in Section 2.7.

3.2 Rigid-plastic limit of the perfect plasticity semi-mechanistic formulation

To formulate contact laws for rigid-plastic matieral adopting strain-hardening behavior, we began by taking the rigid-plastic limit of the perfect plasticity formulation (Agarwal et al., 2021). The rigid-plastic limit of the equations that define the contact radius-displacement and contact pressure-displacement relationships are taken by finding the limit as the material properties ratio E/σ_y approaches ∞. In the formulation, the contact law proposed has the form

$$P(\gamma; \lambda, \zeta, \mathrm{LC}) := \bar{H}(\gamma/2R; \lambda, \zeta, \mathrm{LC})\sigma_y \pi \{a(\gamma; \lambda, \mathrm{LC})\}^2 \tag{3.9}$$

where $\lambda = E/(1-\nu^2)\sigma_y$ and $\zeta = B/\sigma_y$, where B is the elastic bulk modulus of the material. λ and ζ are dimensionless material parameters, LC denotes loading configuration dependency, and $\bar{H}$ is the normalized Brinell hardness (E. Olsson and Larsson, 2016; Erik Olsson and

Larsson, 2013a, 2013b) which will be referred to as normalized contact pressure. The similarity contact law and perfectly plastic FE simulations were used to formulate the framework of the normalized contact radius and contact pressure relationships.

3.2.1 Rigid-plastic limit of the contact radius formulation

The semi-mechanistic contact radius formulation was derived from an analytical framework where the curvature correction method was used for the approximation of the spherical profile of the contact surfaces descibed by the similarity contact law given by Eqn. 3.5 (Agarwal & Gonzalez, 2018). A 2-term curvature corrected similarity solution from the Taylor series expansion was used to derive the following form of the contact radius formulation

$$a = \mathcal{D}_1 \left(\frac{1}{\mathbb{A}^{1/2}} \right) \gamma^{1/2} - \mathcal{D}_3 \left(\frac{\mathbb{B}}{\mathbb{A}^{5/2}} \right) \gamma^{3/2} + \mathcal{D}_5 \left(\frac{\mathbb{B}^2}{\mathbb{A}^{9/2}} \right) \gamma^{5/2} \qquad (3.10)$$

where $\mathbb{A}$ is from Eqn. 3.7, $\mathbb{B} = 1/R_1^3 + 1/R_2^3$, and $\mathcal{D}_i$ (i = 1, 2, 3) are material properties and loading condition dependent parameters. The rigid-plastic limit of the contact radius formulation does not change the form in Eqn. 3.10 as it only affects the definition of parameters $\mathcal{D}_i$. At the limit, these parameters become only loading condition dependent where the values are presented in Table 3.1.

Table 3.1. Estimated values of $\mathcal{D}_i$.

	SC	DC	HC
$\mathcal{D}_1$	1.7527	1.7943	1.8959
$\mathcal{D}_3$	2.3702	3.0451	8.8138
$\mathcal{D}_5$	3.3715	5.7169	39.8654

3.2.2 Rigid-plastic limit of the normalized contact pressure formulation

The normalized contact pressure formulation is derived by analysing finite element (FE) simulations of elastic-ideally plastic particles ($1/m \to 0$) (Agarwal et al., 2021). During large compression of elasto-plastic particles, there are five main deformation regimes the particles undergo: elastic, elastic-plastic, plastic, and low compressibility and elastic volumetric regimes

for confined loading configurations. The formulation is built on different contact laws for each regime where the transition from each regime is C^1-continuous resulting in a continuous and differentiable semi-mechanistic contact law. The normalized contact pressure for the elastic regime, occuring at small deformations, is described using Hertz contact theory (Hertz, 1882). In the elastic-plastic regimes, the normalized contact pressure can be described by a nonlinear relationship with displacement. The normalized contact pressure for both of these regimes are

$$\bar{H}^{\mathrm{e}} = \frac{2}{3\pi} \lambda \mathbb{A}^{1/2} \gamma^{1/2} \tag{3.11}$$

$$\bar{H}^{\mathrm{ep}} = \bar{H}_{\mathrm{max}} - c_1 \left[\ln \left(\frac{\gamma|_{\bar{H}_{\mathrm{max}}}}{\gamma} \right) \right]^{c_2} \tag{3.12}$$

where $\bar{H}_{\mathrm{max}}$ and $\gamma|_{\bar{H}_{\mathrm{max}}}$ are the normalized contact pressure and corresponding displacement value at the point of transition between elastic-plastic and plastic regimes. Parameters c_1, and c_2 are obtained by honoring the C^1-continuous condition, that is, setting the equations and their first derivatives with respect to displacement equal to one another at the point of transition between the two regimes. The values of $\gamma|_{\bar{H}_{\mathrm{max}}}$ are obtained by observing the FE simulations showing a clear relationships with material properties. For the rigid-plastic limit the elastic and elastic-plastic regimes do not exist. This is not directly obtained from taking the limits of the equations, but rather from determining the region of deformation for these regimes at the rigid-plastic limit. At the limit, $\gamma|_{\bar{H}_{\mathrm{max}}} = 0$ and $\bar{H}_{\mathrm{max}} = 3.101$ indicating that elastic and elastic-plastic regime do not have a deformation region, the normalized contact pressure begins with the plastic regime from $\bar{H}_{\mathrm{max}}$. The plastic regime depends on loading configuration and material properties and is given by

$$\bar{H}^{\mathrm{fp}} = \bar{H}_{\mathrm{max}} - p^{LC} \left[\tanh \left\{ q \left(\frac{\gamma - \gamma|_{\bar{H}_{\mathrm{max}}}}{R_1 + R_2} \right) \right\} \cos \left\{ \left(\frac{\gamma - \gamma|_{\bar{H}_{\mathrm{max}}}}{R_1 + R_2} \right) - s(\gamma|_{\bar{H}_{\mathrm{min}}}, q) \right\} \right]^r \tag{3.13}$$

with

$$s(\gamma|_{\bar{H}_{\min}}, q) = \left(\frac{\gamma|_{\bar{H}_{\min}} - \gamma|_{\bar{H}_{\max}}}{R_1 + R_2}\right) - \tan^{-1}\left[2q\operatorname{csch}\left\{2q\left(\frac{\gamma|_{\bar{H}_{\min}} - \gamma|_{\bar{H}_{\max}}}{R_1 + R_2}\right)\right\}\right] \quad (3.14)$$

In these equations, p^{LC}, q, and r are model parameters and $\gamma|_{\bar{H}_{\min}}$ is the displacement value at the minimum normalized contact pressure, $\bar{H}_{\min}$. The minimum value of normalized contact pressure heavily depends on loading conditions and level of softening making $\gamma|_{\bar{H}_{\min}}$ and parameter p^{LC} loading condition and material dependent, while parameters q and r are only material dependent. It is important to note that through a parameter study, parameter p^{LC} was determined to control the minimum value of normalized contact pressure. For determining the minimum value of normalized contact pressure, the case of two spherical particles with equal radii is considered ($R_1 + R_2 = 2R$). For simple loading condition, the particle can be deformed to the point where it becomes a flat disk at $\gamma \to 2R$, at which point, the contact pressure of the material approaches the material's yield strength. This means that for the case of simple loading condition $\gamma|_{\bar{H}_{\min}} = 2R$. For confined loading conditions, there is a low compressibility and elastic volumetric regimes where the contact pressure rises due to void filling. The occupation of the voronoi cell increaes the elastic energy of the particle and the contact pressure. During this phase, the evolution of contact area is limited. This analysis led to the proposition that at the minimum in the case of confined loading conditions, the following condition is true

$$\rho_V^{\text{LC,contact}} \times \rho_S^{\text{LC,contact}} = \Gamma \quad (3.15)$$

where $\rho_V^{\text{LC,contact}}$ and $\rho_S^{\text{LC,contact}}$ are the relative volume density and relative surface area density, and $\Gamma = 0.0593$. The relative volume density is determined from

$$\rho_V^{\text{LC,contact}} = \rho_V^{\text{LC}} \times \left(\frac{V_{\text{contact}}^{\text{LC}}}{V_{\text{voro}}^{\text{LC}}}\right) = \left(\frac{V_{\text{particle}}}{V_{\text{voro}}^{\text{LC}}}\right)\left(\frac{V_{\text{contact}}^{\text{LC}}}{V_{\text{voro}}^{\text{LC}}}\right) \quad (3.16)$$

In the eqution above, $\rho_V^{\text{LC}} = \left(V_{\text{particle}}/V_{\text{voro}}^{\text{LC}}\right)$ is the relative density of the particle's voronoi cell (Harthong et al., 2009), $V_{\text{particle}} = (4/3)\pi R^3$ and $V_{\text{voro}}^{\text{LC}}$ are the volumes of the spherical particle and the voronoi cell. $V_{\text{contact}}^{\text{LC}}$ is the volume of the contact section with the voronoi cell

Table 3.2. Expressions for various volume and surface quantities in the minimum $\bar{H}$ condition given by Eq. (2.28) for all contacts under hydrostatic and primary contacts under die loading configuration.

	DC	HC
$V_{\text{voro}}^{\text{LC}}$	$8R^2\left(R-\gamma/2\right)$	$8\left(R-\gamma/2\right)^3$
$V_{\text{contact}}^{\text{LC}}$	$(4/3)R^2\left(R-\gamma/2\right)$	$(4/3)\left(R-\gamma/2\right)^3$
$S_{\text{face}}^{\text{LC}}$	$4R^2$	$4\left(R-\gamma/2\right)^2$

described as a pyramid with the apex being the center of mass of the particle and the base being the voronoi cell face in contact. The relative surface area density is determined from

$$\rho_S^{\text{LC,contact}} = \frac{S_{\text{contact}}^{\text{LC}}}{S_{\text{face}}^{\text{LC}}} \tag{3.17}$$

where $S_{\text{contact}}^{\text{LC}}$ and $S_{\text{face}}^{\text{LC}}$ are the contact area of the particle and the contact area of the voronoi cell face. the area of the contact's voronoi cell face. Expressions for $V_{\text{voro}}^{\text{LC}}$, $V_{\text{contact}}^{\text{LC}}$ and $S_{\text{face}}^{\text{LC}}$ for die and hydrostatic loading conditions are shown in Table 3.2. The value of $\gamma|_{\bar{H}_{\min}}$ for die and hydrostatic loading conditions is determined from Eqn. (3.15) which involves solving a quintic equation in terms of unknown $\gamma|_{\bar{H}_{\min}}$, see Appendix C for the derivation.

For the case of simple loading configuration, $\gamma|_{\bar{H}_{\min}} = 2R$, thus $\bar{H}_{\min} = 1$. Using this condition and using Eqns. 3.13 and 3.14, parameter p^{LC} for the simple loading condition is given by

$$p^{\text{SC}} = \frac{\bar{H}_{\max} - 1}{\left[\tanh\left\{q\left(1 - \frac{\gamma|_{\bar{H}_{\max}}}{2R}\right)\right\} \cos\left\{\left(1 - \frac{\gamma|_{\bar{H}_{\max}}}{2R}\right) - s(2R, q)\right\}\right]^r} \tag{3.18}$$

Determining the value of minimum normalized contact pressure for die and hydrostatic loading conditions is determined through two methods. The first method suggests that the

minimum normalized contact pressure for die and hydro is equal to the value of normalized contact pressure for simple loading condition at $\gamma|_{\bar{H}_{\min}}$, i.e,

$$
\begin{aligned}
\bar{H}^{\mathrm{LC}}_{\min,1} = \bar{H}_{\max} - p^{\mathrm{SC}} & \left[\tanh\left\{ q\left(\frac{\gamma^{\mathrm{LC}}|_{\bar{H}_{\min}} - \gamma|_{\bar{H}_{\max}}}{2R} \right) \right\} \right. \\
& \left. \times \cos\left\{ \left(\frac{\gamma^{\mathrm{LC}}|_{\bar{H}_{\min}} - \gamma|_{\bar{H}_{\max}}}{2R} \right) - s(2R, q) \right\} \right]^{r}
\end{aligned}
\tag{3.19}
$$

The second method for determinig the minimum value of normalized contact pressure utlizes the inflection point where the second derivative of the normalized contact pressure is equal to zero. In the FE simulations of elastic-ideally plastic particles, this inflection point happens when softening begins. At this inflection point, the slopes from die and hydrostatic loading conditions is set equal to the slope from simple loading condition giving the second solution for the value of $\bar{H}_{\min}$

$$
\begin{aligned}
\bar{H}^{\mathrm{LC}}_{\min,2} = \bar{H}_{\max} - p^{\mathrm{LC}}_o & \left[\tanh\left\{ q\left(\frac{\gamma^{\mathrm{LC}}|_{\bar{H}_{\min}} - \gamma|_{\bar{H}_{\max}}}{2R} \right) \right\} \right. \\
& \left. \times \cos\left\{ \left(\frac{\gamma^{\mathrm{LC}}|_{\bar{H}_{\min}} - \gamma|_{\bar{H}_{\max}}}{2R} \right) - s(\gamma^{\mathrm{LC}}|_{\bar{H}_{\min}}, q) \right\} \right]^{r}
\end{aligned}
\tag{3.20}
$$

where

$$
\begin{aligned}
p^{\mathrm{LC}}_o = p^{\mathrm{SC}} & \left[\frac{2q\operatorname{csch}\left\{ 2q\left(\frac{\gamma^{\mathrm{SC}}|_{\bar{H}=0} - \gamma|_{\bar{H}_{\max}}}{2R} \right) \right\} - \tan\left\{ \left(\frac{\gamma^{\mathrm{SC}}|_{\bar{H}=0} - \gamma|_{\bar{H}_{\max}}}{2R} \right) - s(2R, q) \right\}}{2q\operatorname{csch}\left\{ 2q\left(\frac{\gamma^{\mathrm{LC}}|_{\bar{H}=0} - \gamma|_{\bar{H}_{\max}}}{2R} \right) \right\} - \tan\left\{ \left(\frac{\gamma^{\mathrm{LC}}|_{\bar{H}=0} - \gamma|_{\bar{H}_{\max}}}{2R} \right) - s(\gamma^{\mathrm{LC}}|_{\bar{H}_{\min}}, q) \right\}} \right] \\[2ex]
& \times \left[\frac{\tanh\left\{ q\left(\frac{\gamma^{\mathrm{SC}}|_{\bar{H}=0} - \gamma|_{\bar{H}_{\max}}}{2R} \right) \right\} \times \cos\left\{ \left(\frac{\gamma^{\mathrm{SC}}|_{\bar{H}=0} - \gamma|_{\bar{H}_{\max}}}{2R} \right) - s(2R, q) \right\}}{\tanh\left\{ q\left(\frac{\gamma^{\mathrm{LC}}|_{\bar{H}=0} - \gamma|_{\bar{H}_{\max}}}{2R} \right) \right\} \times \cos\left\{ \left(\frac{\gamma^{\mathrm{LC}}|_{\bar{H}=0} - \gamma|_{\bar{H}_{\max}}}{2R} \right) - s(\gamma^{\mathrm{LC}}|_{\bar{H}_{\min}}, q) \right\}} \right]^{r}
\end{aligned}
\tag{3.21}
$$

and

$$\frac{\gamma^{\mathrm{LC}}|_{\bar{H}=0}}{2R} \simeq \frac{\gamma|_{\bar{H}_{\max}}}{2R} + \frac{3r\tan\left\{s(\gamma^{\mathrm{LC}}|_{\bar{H}_{\min}},q)\right\} + \left[3(2q^2+3)(r-1)(2r+1) + 9(2r^2-1)\tan^2\left\{s(\gamma^{\mathrm{LC}}|_{\bar{H}_{\min}},q)\right\}\right]^{1/2}}{(2q^2+3)(2r+1) + 3(r+1)\tan^2\left\{s(\gamma^{\mathrm{LC}}|_{\bar{H}_{\min}},q)\right\}} \tag{3.22}$$

The results from the two methods are compared with the FE simulations which showed that an average of the two solutions provides an accurate prediction of the minimum value of normalized contact pressure for the confined loading conditions (Agarwal et al., 2021). From this observation, the final value of $\bar{H}_{\min}$ is determined to be

$$\bar{H}_{\min}^{\mathrm{LC}} = \frac{\bar{H}_{\min,1}^{\mathrm{LC}} + \bar{H}_{\min,2}^{\mathrm{LC}}}{2} \tag{3.23}$$

The rigid-plastic limit of the plastic regime eliminates the dependency on the material and the equations become only loading condition dependent. For the limit, the normalized contact pressure for the plastic regime becomes

$$\bar{H}^{\mathrm{fp}} = \bar{H}_{\max} - p^{LC}\left[\tanh\left\{q\left(\frac{\gamma}{2R}\right)\right\}\cos\left\{\left(\frac{\gamma}{2R}\right) - s^{LC}\right\}\right] \tag{3.24}$$

with

$$s^{\mathrm{LC}} = \left(\frac{\gamma|_{\bar{H}_{\min}}}{2R}\right) - \tan^{-1}\left[2q\operatorname{csch}\left\{2q\left(\frac{\gamma|_{\bar{H}_{\min}}}{2R}\right)\right\}\right] \tag{3.25}$$

$$p^{\mathrm{LC}} = \frac{\bar{H}_{\max} - \bar{H}_{\min}^{\mathrm{LC}}}{\left[\tanh\left\{q\left(\frac{\gamma^{\mathrm{LC}}|_{\bar{H}_{\min}}}{2R}\right)\right\}\cos\left\{-s^{\mathrm{LC}}\right\}\right]} \tag{3.26}$$

and

$$\bar{H}_{\min}^{\mathrm{LC}} = \frac{\bar{H}_{\min,1}^{\mathrm{LC}} + \bar{H}_{\min,2}^{\mathrm{LC}}}{2} \tag{3.27}$$

where

$$\begin{aligned}\bar{H}_{\min,1}^{\mathrm{LC}} = &\bar{H}_{\max} - p^{\mathrm{SC}}\left[\tanh\left\{q\left(\frac{\gamma^{\mathrm{LC}}|_{\bar{H}_{\min}}}{2R}\right)\right\}\right. \\ &\left.\times\cos\left\{\frac{\gamma^{\mathrm{LC}}|_{\bar{H}_{\min}}}{2R} - s^{\mathrm{LC}}(2R)\right\}\right]\end{aligned} \tag{3.28}$$

$$\bar{H}^{\mathrm{LC}}_{\min,2} = \bar{H}_{\max} - p_o^{\mathrm{LC}} \left[\tanh\left\{ q\left(\frac{\gamma^{\mathrm{LC}}|_{\bar{H}_{\min}}}{2R} \right) \right\} \right.$$
$$\left. \times \cos\left\{ \frac{\gamma^{\mathrm{LC}}|_{\bar{H}_{\min}}}{2R} - s^{\mathrm{LC}}(\gamma^{\mathrm{LC}}|_{\bar{H}_{\min}}) \right\} \right] \tag{3.29}$$

with

$$p^{\mathrm{SC}} = \bar{H}_{\max} - 1 \tag{3.30}$$

$$p_o^{\mathrm{LC}} = p^{\mathrm{SC}} \left[\frac{2q\,\mathrm{csch}\left\{ 2q\left(\frac{\gamma^{\mathrm{SC}}|_{\bar{H}=0}}{2R} \right) \right\}}{2q\,\mathrm{csch}\left\{ 2q\left(\frac{\gamma^{\mathrm{LC}}|_{\bar{H}=0}}{2R} \right) \right\}} - \tan\left\{ \left(\frac{\gamma^{\mathrm{SC}}|_{\bar{H}=0}}{2R} \right) - s^{\mathrm{LC}}(2R) \right\} }{2q\,\mathrm{csch}\left\{ 2q\left(\frac{\gamma^{\mathrm{LC}}|_{\bar{H}=0}}{2R} \right) \right\}} - \tan\left\{ \left(\frac{\gamma^{\mathrm{LC}}|_{\bar{H}=0}}{2R} \right) - s^{\mathrm{LC}}(\gamma^{\mathrm{LC}}|_{\bar{H}_{\min}}) \right\}} \right]$$
$$\times \left[\frac{\tanh\left\{ q\left(\frac{\gamma^{\mathrm{SC}}|_{\bar{H}=0}}{2R} \right) \right\} \times \cos\left\{ \left(\frac{\gamma^{\mathrm{SC}}|_{\bar{H}=0}}{2R} \right) - s^{\mathrm{LC}}(2R) \right\}}{\tanh\left\{ q\left(\frac{\gamma^{\mathrm{LC}}|_{\bar{H}=0}}{2R} \right) \right\} \times \cos\left\{ \left(\frac{\gamma^{\mathrm{LC}}|_{\bar{H}=0}}{2R} \right) - s^{\mathrm{LC}}(\gamma^{\mathrm{LC}}|_{\bar{H}_{\min}}) \right\}} \right] \tag{3.31}$$

and

$$\frac{\gamma^{\mathrm{LC}}|_{\bar{H}=0}}{2R} \simeq \frac{3r\tan\left\{ s^{\mathrm{LC}}(\gamma^{\mathrm{LC}}|_{\bar{H}_{\min}}) \right\} \left[9\tan^2\left\{ s^{\mathrm{LC}}(\gamma^{\mathrm{LC}}|_{\bar{H}_{\min}}) \right\} \right]^{1/2}}{3(2q^2+3) + 6\tan^2\left\{ s^{\mathrm{LC}}(\gamma^{\mathrm{LC}}|_{\bar{H}_{\min}}) \right\}} \tag{3.32}$$

where $q = 14.1819$ and $\gamma^{\mathrm{LC}}|_{\bar{H}_{\min}}$ is solved for die and hydrostatic loading conditions, see Appendix C. The methods for determining the minimum normalized contact pressure remain the same but the equations simplify as they are no longer dependent on material properties. For confined loading conditions, the normalized contact pressure evolves in the low compressibility regime which depends heavily on the loading condition. The proposed form of the normalized contact pressure in this regime is given by

$$\bar{H}^{\mathrm{lc}} = \bar{H}^{\mathrm{LC}}_{\min} - u\ln\left\{ 1 - l\left(\frac{\chi^{\mathrm{LC}} - \chi^{\mathrm{LC}}|_{\bar{H}_{\min}}}{\chi^{\mathrm{LC}}_{\mathrm{zp}} - \chi^{\mathrm{LC}}|_{\bar{H}_{\min}}} \right)^2 \right\} \tag{3.33}$$

where u and l are model parameters and $\chi^{\mathrm{LC}} = 1/\rho_V^{\mathrm{LC}} = \left(V_{\mathrm{voro}}^{\mathrm{LC}}/V_{\mathrm{particle}}\right)$ is the inverse of the relative density, where the relationships to displacement for the die and hydrostatic loading conditions is given by

$$\frac{\gamma^{\mathrm{DC}}}{2R} = 1 - \frac{\pi\chi^{\mathrm{DC}}}{6} \ , \quad \frac{\gamma^{\mathrm{HC}}}{2R} = 1 - \left(\frac{\pi\chi^{\mathrm{HC}}}{6}\right)^{1/3} \tag{3.34}$$

$\chi^{\mathrm{LC}}|_{\bar{H}_{\min}}$ is the value of χ at $\bar{H}_{\min}^{\mathrm{LC}}$ and $\chi_{\mathrm{zp}}^{\mathrm{LC}}$ is the value of χ at the zero porosity limit (Tsigginos et al., 2015) which is given by

$$\chi_{\mathrm{zp}}^{\mathrm{LC}} = \frac{V_{\mathrm{particle}} - V_{\mathrm{el}}^{\mathrm{LC}}}{V_{\mathrm{particle}}} \tag{3.35}$$

where $V_{\mathrm{el}}^{\mathrm{LC}}$ is the particle's elastic reduction in volume until the point of zero porosity. After the zero porosity limit, the normalized contact pressure evolves in the elastic volumetric regime given by

$$\bar{H}^{\mathrm{ev}} = \frac{B}{\sigma_y}\left(1 - \frac{V_{\mathrm{voro}}}{V_{\mathrm{particle}}}\right) = \zeta(1 - \chi^{\mathrm{LC}}) \tag{3.36}$$

where $\zeta = E/3\sigma_y(1 - 2\nu)$. The relationships between u, l, and $V_{\mathrm{el}}^{\mathrm{LC}}$ is determined through the C^1 continuity condition between the low compressibility and elastic volumetric regime. These relationships are given by

$$u = \frac{V_{\mathrm{particle}}\bar{H}_{\min}^{\mathrm{LC}} - \zeta V_{\mathrm{el}}^{\mathrm{LC}}}{V_{\mathrm{particle}}\ln(1 - l)} \tag{3.37}$$

$$V_{\mathrm{el}}^{\mathrm{LC}} = \frac{V_{\mathrm{particle}}\left\{2l\bar{H}_{\min}^{\mathrm{LC}} + \zeta(1 - \chi^{\mathrm{LC}}|_{\bar{H}_{\min}})(1 - l)\ln(1 - l)\right\}}{\zeta\left\{2l + (1 - l)\ln(1 - l)\right\}} \tag{3.38}$$

From FE simulations, it was determined that parameter l is a material dependent parameter given by

$$\ln(1 - l) = \ln\left(\frac{1}{1 + 0.2335\zeta}\right)$$
$$\implies l = 1 - \left(\frac{1}{1 + 0.2335\zeta}\right) \tag{3.39}$$

The rigid-plastic limit of the elastic volumetric regime becomes ∞ whereas the limit of the low compressibilty regime becomes

$$\bar{H}^{\text{lc}} = \bar{H}^{\text{LC}}_{\min} + \left(\frac{1 - \chi^{\text{LC}}|_{\bar{H}_{\min}}}{0.467}\right) \ln\left\{1 - \left(\frac{\chi^{\text{LC}} - \chi^{\text{LC}}|_{\bar{H}_{\min}}}{\chi^{\text{LC}}_{\text{zp}} - \chi^{\text{LC}}|_{\bar{H}_{\min}}}\right)^2\right\} \tag{3.40}$$

To conclude, the rigid-plastic limit of the semi-mechanistic contact law for normalized contact pressure becomes

$$\lim_{E/\sigma_y \to \infty} \bar{H} = \begin{cases} \lim_{E/\sigma_y \to \infty} \bar{H}^{\text{fp}} = \bar{H}_{\max} - p^{\text{LC}}\left[\tanh\left\{q\left(\frac{\gamma}{2R}\right)\right\}\right. & \gamma \in \left(0, \gamma^{\text{LC}}|_{\bar{H}_{\min}}\right] \\ \qquad\qquad \left. \times \cos\left\{\left(\frac{\gamma}{2R}\right) - s^{\text{LC}}\right\}\right] & \text{LC} \to \{\text{SC}, \text{DC}, \text{HC}\} \\ \lim_{E/\sigma_y \to \infty} \bar{H}^{\text{lc}} = \bar{H}^{\text{LC}}_{\min} + \left(\frac{1-\chi^{\text{LC}}|_{\bar{H}_{\min}}}{0.467}\right) & \gamma \in \left(\gamma^{\text{LC}}|_{\bar{H}_{\min}}, \gamma^{\text{LC}}_{\text{zp}}\right] \\ \qquad\qquad \times \ln\left\{1 - \left(\frac{\chi^{\text{LC}}-\chi^{\text{LC}}|_{\bar{H}_{\min}}}{\chi^{\text{LC}}_{\text{zp}}-\chi^{\text{LC}}|_{\bar{H}_{\min}}}\right)^2\right\} & \text{LC} \to \{\text{DC}, \text{HC}\} \\ \lim_{E/\sigma_y \to \infty} \bar{H}^{\text{ev}} = \infty & \gamma \in \left(\gamma^{\text{LC}}_{\text{zp}}, \infty\right) \\ & \text{LC} \to \{\text{DC}, \text{HC}\} \end{cases} \tag{3.41}$$

3.3 Space-filling design and FE simulations

For our study, we performed 60 finite element simulations; 20 for each three loading configuration (simple compression, die compaction, and hydrostatic compaction). The hardening properties (strength coefficient κ and hardening exponent $1/m$ from Eqn. (3.3)) are randomly chosen to eliminate bias by solving a space-filling design problem set up using the statistical software ("SAS Institute Inc", 2018). In the software, Fast Flexible Filling algorithm (Lekivetz & Jones, 2015) is utilized where the Number of Runs and Cluster Size are chosen minimize MaxPro optimality criterion (Joseph et al., 2015). Loading configurations were set as a categorial factor where the created sub-clusters by the algorithm are assigned to. In the space-filling design problem, the full range of hardening exponent is used (from 0 to 1). The lower bound of the hardening coefficient was chosen based on the fitting of Ludwik's power law to Holloman's power law, whereas the upper limit is chosen based on the range of common materials. The bounds chosen for the hardening properties in the space-filling

design problem are in Table 3.3. Figure 3.1 shows a scatter plot of the hardening properties obtained from the solution of the space-filling design problem. For a complete list of these hardening properties, refer to Appendix E.

Table 3.3. Bounds for hardening exponent $1/m$ and strength coefficient κ used in the space-filling design problem.

	Lower Bound	Upper Bound
$1/m$	0	1
κ (MPa)	50	200
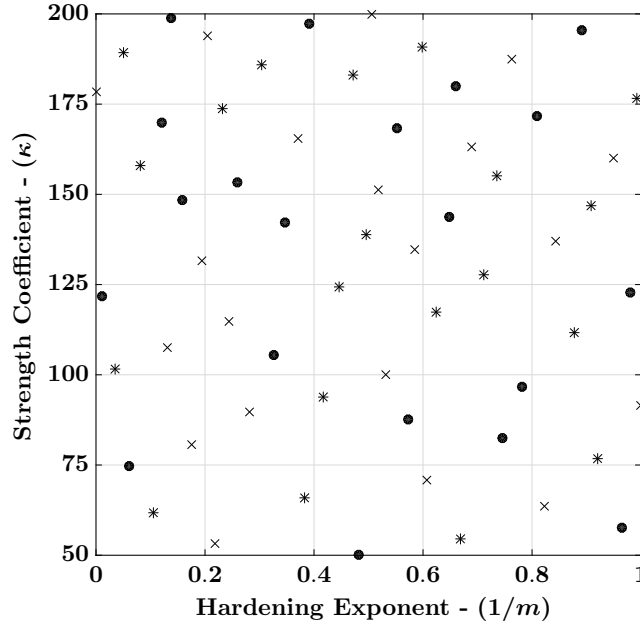
Fig.3.1. Scatter plot of the hardening properties obtained from the space-filling design problem. Simple loading configuration properties are denoted by solid circle markers. Die loading configuration properties are denoted by cross markers. Hydrostatic loading configuration properties are denoted by asterick markers.

The hardening properties from the space-filling design problem were used to run FE simulation using ABAQUS Version 6.14. This work follows the same setup procedure as the semi-mechanistic contact law for elastic-ideally plastic particles (Agarwal et al., 2021), where an eighth of a sphere with radius $R = 10$ mm is deformed. The mesh used in ABAQUS consists of 500,000 linear hexahedral elements of type C3D8R and 515,201 nodes. To capture

87

the particle deformation level present in power compaction processes, the simulated particle is deformed until 50% for simple compression, 47.6% for die compaction, and 19.6% for hydrostatic compaction. The deformation level for die and hydrostatic compaction were determined based on the zero porosity limit caused by confiment, that is, $\gamma/2R = 1 - \pi/6$ for die compaction and $\gamma/2R = 1 - (\pi/6)^{1/3}$ for hydrostatic compaction.

Given the focus on plastic regime and hardening behavior of materials for different hardening properties, all simulations are given the same elastic parameters, namely, Young's Modulus E, yield stress σ_y, and Poisson's ratio ν. Our study utilizes rigid-plastic analysis for building the contact law, thus, a large Young's Modulus and a small yield stress are chosen to minimize elastic and elastic-plastic regimes. The materials used in the simulations follow the constituve law in Eqn. (3.1). As mentioned in the previous section, parameters K and n in the consitutive law are calibrated by setting the two power-law hardening equations (Eqns. (3.1) and (3.3)) equal to one another.

To ensure the validity of rigid-plastic assumption, test set of FE simulations are performed using the lower and upper bound values for κ. The results show how small the elastic and elasto-plastic regimes validating our rigid-plastic assumption. These results are presented in Figure 3.2 for simple, die, and hydrostatic loading configurations. In these plots, the limit of $\kappa = 20$ MPa is used, however, a lower limit of $\kappa = 50$ MPa was chosen for the simulations. The lower bound of κ was increased because we observed that materials having such low κ in combination with a low hardening exponent $(1/m)$ resulted in inadequate fitting of the power-law equations.
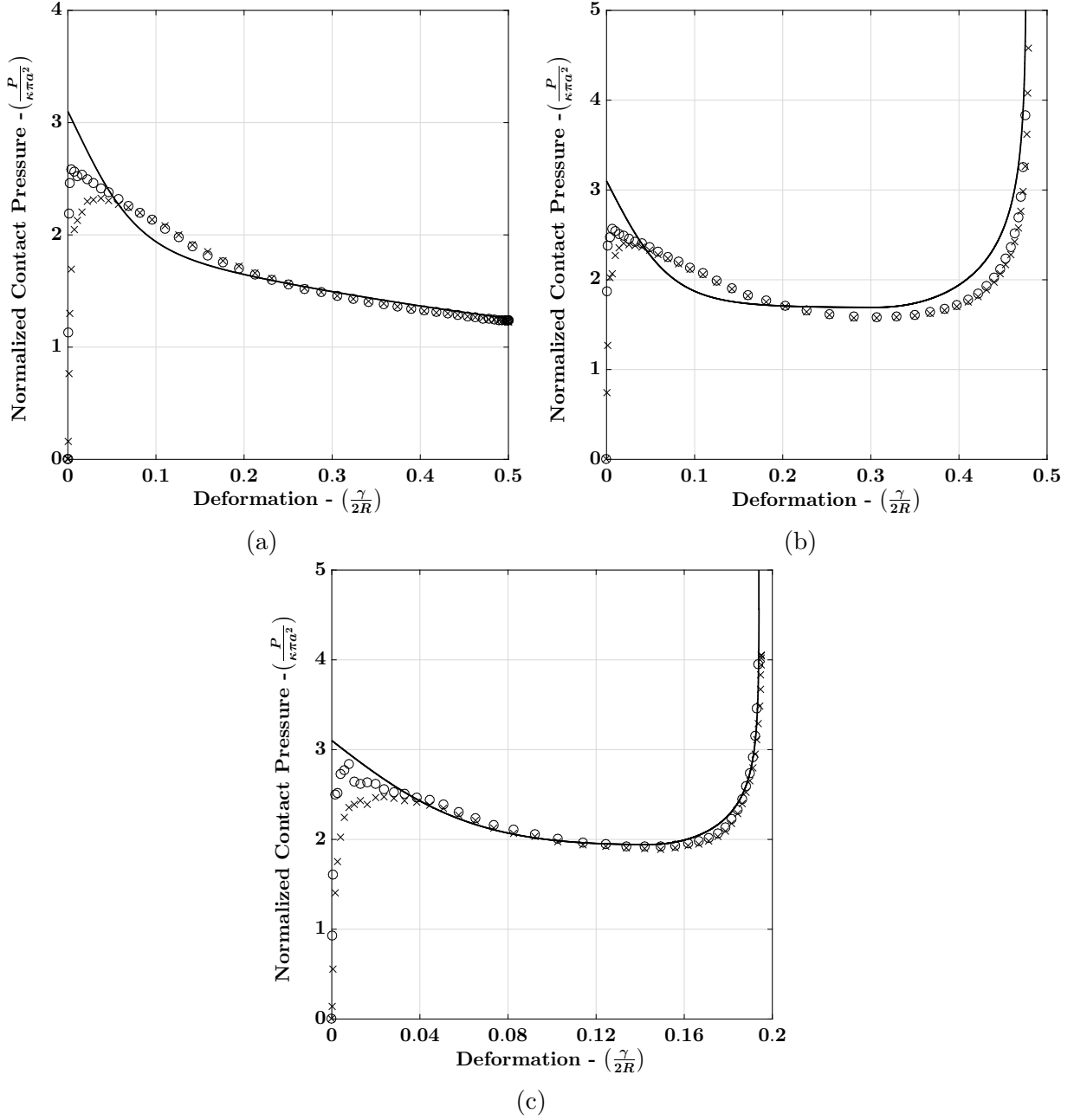
Fig.3.2. FE simulations results for normalized contact pressure under simple compression (3.2a), die compaction (3.2b), and hydrostatic compaction (3.2c) for near perfectly plasticity with $1/m = 0.0001$. The figure shows the lower bound $\kappa = 20$ MPa denoted by circle markers and upper bound $\kappa = 200$ MPa denoted by cross markers. The figure also includes the results from the rigid-plastic limit of the perfectly plasticity semi-mechanistic contact law (solid black lines).
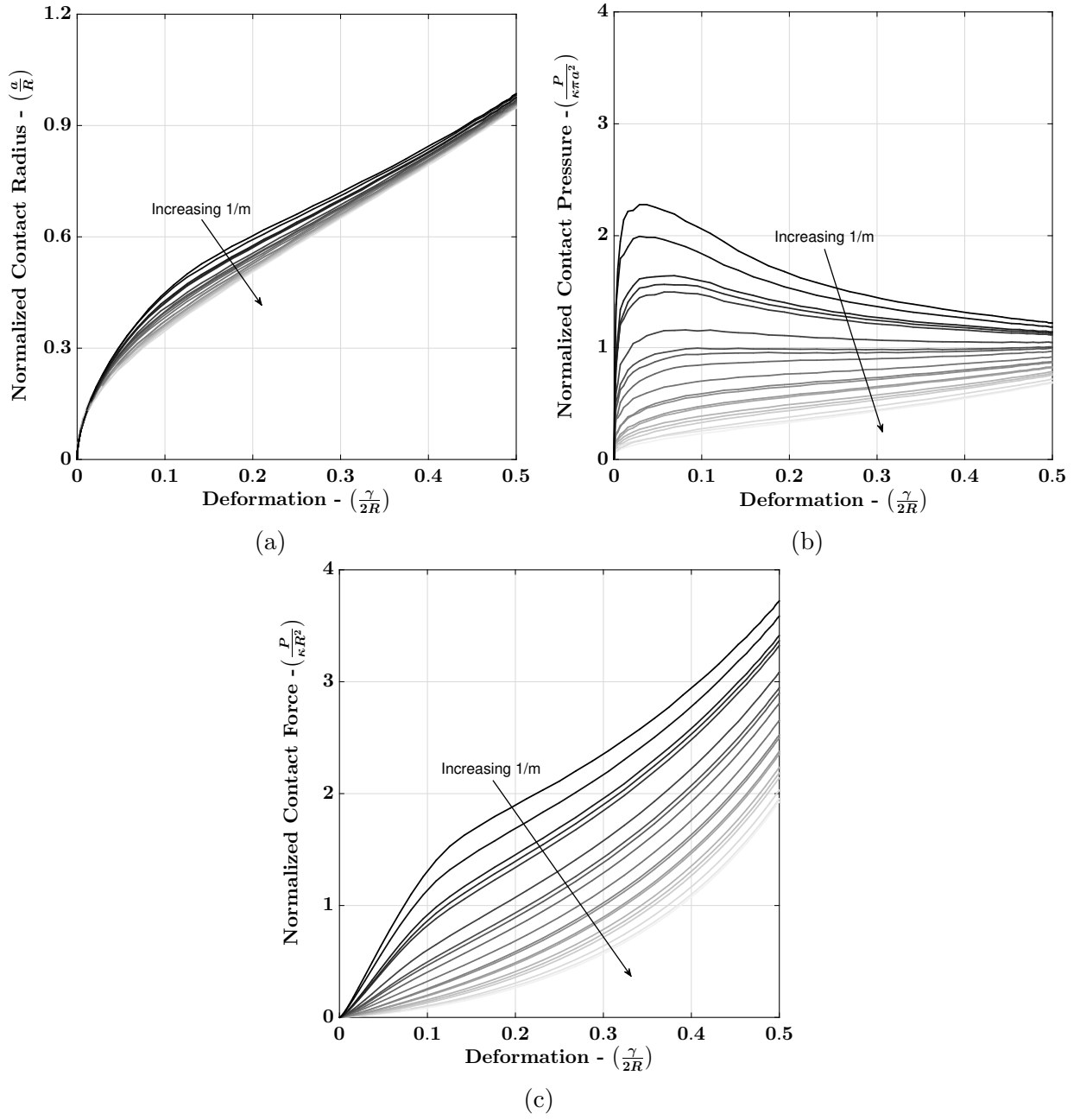
Fig.3.3. Finite element simulation results for simple loading configuration of normalized contact radius 3.3a, contact pressure 3.3b, and contact force 3.3c. The figures show results of 20 simulations where there is a clear trend with increasing hardening exponent $(1/m)$.

90

(a)

(b)

(c)
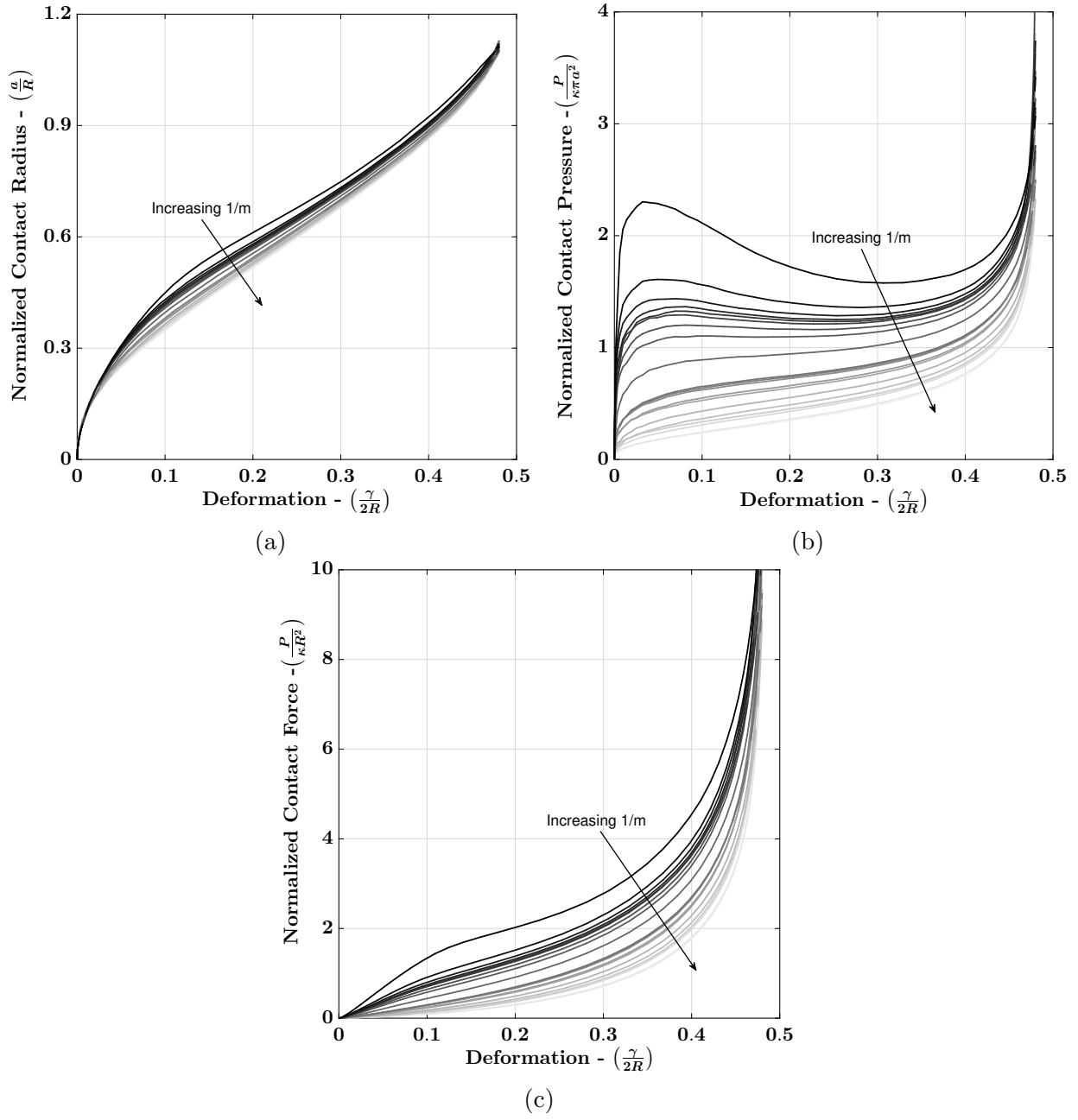
Fig.3.4. Finite element simulation results for die loading configuration of normalized contact radius 3.4a, contact pressure 3.4b, and contact force 3.4c. The figures show results of 20 simulations where there is a clear trend with increasing hardening exponent $(1/m)$.

(a)

(b)

(c)
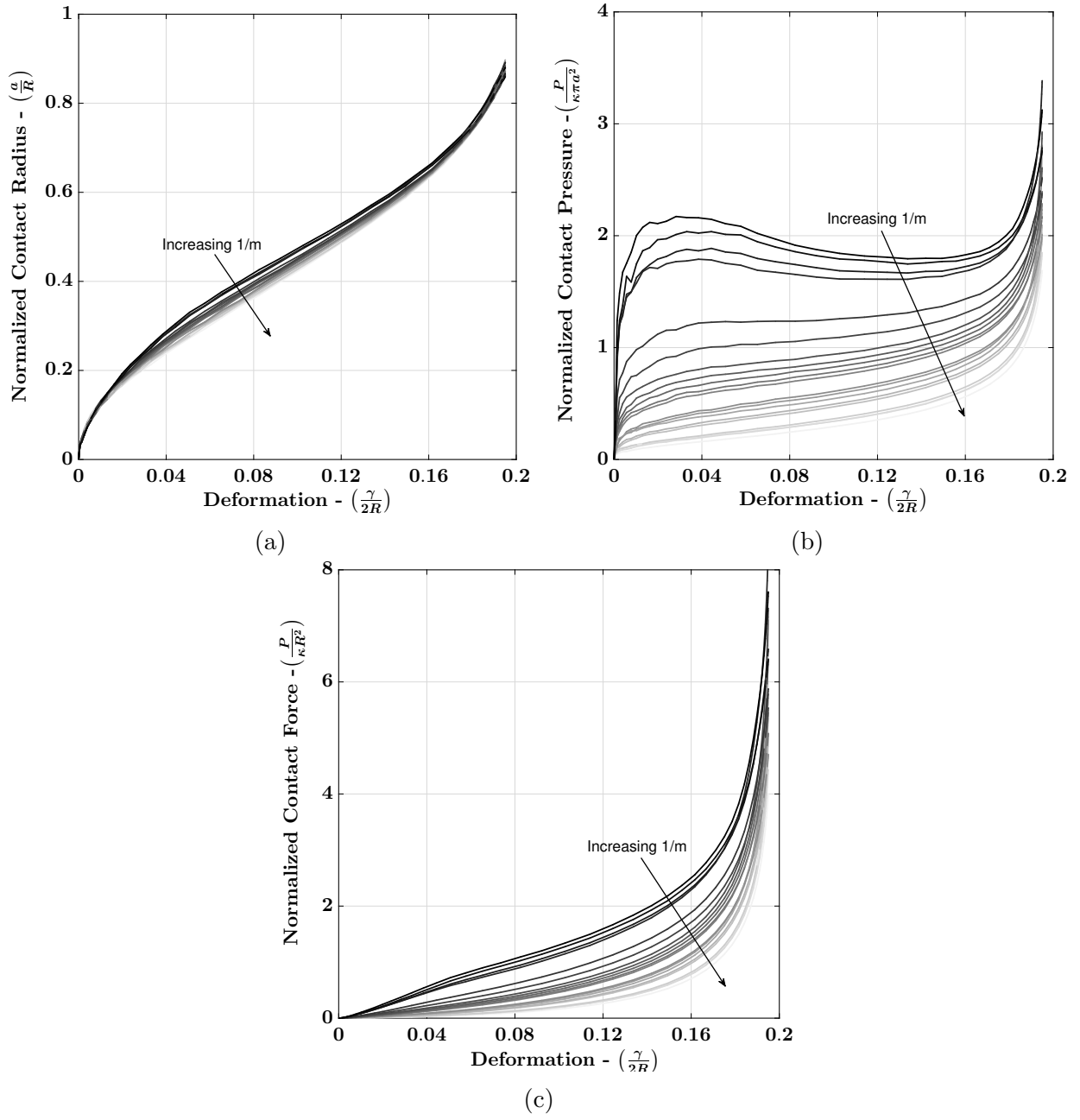
Fig.3.5. Finite element simulation results for hydrostatic loading configuration of normalized contact radius 3.5a, contact pressure 3.5b, and contact force 3.5c. The figures show results of 20 simulations where there is a clear trend with increasing hardening exponent $(1/m)$.

The normalized contact pressure $(P/\kappa\pi a^2)$, contact radius (a/R), and contact force $(P/\kappa R^2)$ obtained from the FE simulations are shown in Figures 3.3, 3.4, and 3.5 for simple, die, and hydrostatic loading configurations. It is clear that all the results show a decreasing trend with increasing hardening exponent $(1/m)$. Normalized contact pressure figures for die and hydrostatic loading configuration show that when the hardening parameter is high enough $(1/m > 0.5)$, the materials no longer shows any softening and the contact pressure only increases with no apparent yield. This is also true for simple loading condition, however, for results with hardening exponent around 0.5, the contact pressure appears to be near a constant value of 1. Under large deformation for die and hydro loading condition, there is an apparent rapid increase in contact pressure caused by the confinement of the particle. From these results, we propose that the simple loading condition only has a plastic regime, whereas die and hydrostatic loading conditions have plastic, low compressibility, and elastic volumetric regimes.

3.4   Formulation of the semi-mechanistic formulation contact law

The FE simulations show that dependency on loading condition and hardening parameter are necessary for formulating a contact law for rigid-plastic particles with power-law hardening. In our case, we are analysing the contact of two materials with equal hardening properties $(\kappa_1 = \kappa_2 = \kappa)$ and radii $(R_1 + R_2 = 2R)$. Using this information and Eqn. (3.5), the similarity contact law in Eqn. (3.4) becomes

$$P = \pi k \left(\frac{a}{R}\right)^{1/m} \kappa a^2 \tag{3.42}$$

where $k = 3 \times 6^{-1/m}$. Combining the equation above with the contact radius-displacement relationship in Eqn. (3.6), the contact force becomes

$$P = \pi k \left(2c^2\right)^{1/2m} \left(\frac{\gamma}{2R}\right)^{1/2m} \kappa a^2 \tag{3.43}$$

where $c^2 = 1.43\mathrm{e}^{-0.97/m}$, $\mathbb{A} = 1/R_1 + 1/R_2$ and $\mathbb{B} = 1/R_1^3 + 1/R_2^3$. From these definitions, the normalized hardness $\bar{H}$ (referred to as contact pressure), from Brinell hardness H from indentation of flat surface by a spherical rigid indentor, is given by

$$\bar{H} = \frac{P}{\kappa\pi a^2} = k\left(2c^2\right)^{1/2m}\left(\frac{\gamma}{2R}\right)^{1/2m} \tag{3.44}$$

The equation above shows that normalized hardness depends on the hardening exponent and deformation, however, as seen in the FE simulations, there is a loading condition dependency that is missing. We propose a contact law in the following form

$$P(\gamma; R, 1/m, \mathrm{LC}) := \bar{H}(\gamma/2R; 1/m, \mathrm{LC})\kappa\pi\{a(\gamma; R, 1/m, \mathrm{LC})\}^2 \tag{3.45}$$

where LC denotes loading configuration. For formulating this contact law, we follow a similar approach as the one adopted for formulating the contact law for elastic-ideally plastic particles. We will utitilize the similarity contact law and the FE data to find semi-mechanistic relationships for contact radius and contact pressure.

3.4.1 Rigid-plastic semi-mechanistic formulation for contact radius

For the contact radius, we begin with the rigid-plastic limit of the perfectly plastic formulation in Eqn. (3.10). To find the dependency on hardening exponent, we revisit the 2-term curvature corrected similarity solution where the first three terms of the Taylor series expansion was used

$$a = 2^{1/2}c\left(\frac{1}{\mathbb{A}}\right)^{1/2}\gamma^{1/2} - 2^{-3/2}c^3\left(\frac{\mathbb{B}^{2/3}}{\mathbb{A}^{5/3}}\right)^{3/2}\gamma^{3/2} + \frac{7}{2^{9/2}}c^5\left(\frac{\mathbb{B}^{4/5}c^2}{\mathbb{A}^{9/5}}\right)^{5/2}\gamma^{5/2} \tag{3.46}$$

where $c^2 = 1.43\mathrm{e}^{-0.97/m}$. Note that the rigid-plastic limit value of $\mathcal{D}_1$ is close to $2^{1/2}c$ when $m \to \infty$. To keep the dependency of hardening exponent in parameters $\mathcal{D}_\mathrm{i}$ (i $= 1, 2, 3$) in the rigid-plastic limit, we propose carrying over the exponential relationship with hardening exponent from the first and second term in c^2. We observed that carrying over the third term

does not predict the contact radius well, instead the third term was calibrated using the FE data. We propose the following expression for contact radius-displacement relationship

$$
\begin{aligned}
a = \mathcal{D}_1 e^{-0.485/m} \left(\frac{1}{\mathbb{A}^{1/2}} \right) \gamma^{1/2} - \mathcal{D}_3 e^{-1.455/m} \left(\frac{\mathbb{B}}{\mathbb{A}^{5/2}} \right) \gamma^{3/2} \\
+ \mathcal{D}_5 e^{-0.5279/m^{0.4616}} \left(\frac{\mathbb{B}^2}{\mathbb{A}^{9/2}} \right) \gamma^{5/2}
\end{aligned}
\tag{3.47}
$$

where $\mathcal{D}_i$ (i = 1, 2, 3) depend on loading condition and the values are presented in Table 3.1. Note that for ideally plastic case ($m \to \infty$), the rigid-plastic limit in Eqn. (3.10) is preserved.

3.4.2 Rigid-plastic semi-mechanistic formulation for normalized hardness

The semi-mechanistic formulation for normalized hardness (will be referred to as normalized contact pressure) begins with the rigid-plastic limit of plastic regime in Eqns. (3.24), (3.25), and (3.26). For the contact pressure in the FE simulations, it is apparent that the value of $\bar{H}_{\max}$ present at small deformations decreases with increasing hardening exponent. The value of $\bar{H}_{\max}$ in the ideally plastic cases represented the maximum normalized contact pressure and the starting value of normalized contact pressure in the plastic regime, however in this case, $\bar{H}_{\max}$ only represents the contact pressure at where the plastic regime begins as there is no maximum in the small deformation region for cases with large hardening exponent. Based on this analysis, we propose a modification to the value of the $\bar{H}_{\max}$ consisting of an exponential function dependent on hardening exponent. Further in Eqn. (3.44), the term $(\gamma/2R)^{1/2m}$ is 1 for the ideally plastic case, thus, it is also carried over to the definition of the contact pressure for the three deformation regimes. The normalized contact pressure for the plastic regime becomes

$$
\begin{aligned}
\bar{H}^{\text{fp}} = \Big[\bar{H}_{\max} e^{-1.748/m} \\
- p^{\text{LC}} \tanh \left\{ q \left(\frac{\gamma}{2R} \right) \right\} \cos \left\{ \left(\frac{\gamma}{2R} \right) - s^{\text{LC}} \right\} \Big] \left(\frac{\gamma}{2R} \right)^{1/2m}
\end{aligned}
\tag{3.48}
$$

with

$$
s^{\text{LC}} = \left(\frac{\gamma|_{\bar{H}_{\min}}}{2R} \right) - \tan^{-1} \left[2q \operatorname{csch} \left\{ 2q \left(\frac{\gamma|_{\bar{H}_{\min}}}{2R} \right) \right\} \right]
\tag{3.49}
$$

$$p^{\text{LC}} = \frac{\bar{H}_{\text{max}} - \bar{H}_{\text{min}}^{\text{LC}}}{\left[\tanh\left\{ q\left(\frac{\gamma^{\text{LC}}|_{\bar{H}_{\text{min}}}}{2R} \right) \right\} \cos\left\{ -s^{\text{LC}} \right\} \right]} \tag{3.50}$$

and

$$\bar{H}_{\text{min}}^{\text{LC}} = \frac{\bar{H}_{\text{min},1}^{\text{LC}} + \bar{H}_{\text{min},2}^{\text{LC}}}{2} \tag{3.51}$$

where

$$\begin{aligned}
\bar{H}_{\text{min},1}^{\text{LC}} = {} & \bar{H}_{\text{max}} - p^{\text{SC}} \left[\tanh\left\{ q\left(\frac{\gamma^{\text{LC}}|_{\bar{H}_{\text{min}}}}{2R} \right) \right\} \right. \\
& \left. \times \cos\left\{ \frac{\gamma^{\text{LC}}|_{\bar{H}_{\text{min}}}}{2R} - s^{\text{LC}}(2R) \right\} \right]
\end{aligned} \tag{3.52}$$

$$\begin{aligned}
\bar{H}_{\text{min},2}^{\text{LC}} = {} & \bar{H}_{\text{max}} - p_o^{\text{LC}} \left[\tanh\left\{ q\left(\frac{\gamma^{\text{LC}}|_{\bar{H}_{\text{min}}}}{2R} \right) \right\} \right. \\
& \left. \times \cos\left\{ \frac{\gamma^{\text{LC}}|_{\bar{H}_{\text{min}}}}{2R} - s^{\text{LC}}(\gamma^{\text{LC}}|_{\bar{H}_{\text{min}}}) \right\} \right]
\end{aligned} \tag{3.53}$$

with

$$p^{\text{SC}} = \bar{H}_{\text{max}} - 1 \tag{3.54}$$

$$p_o^{\text{LC}} = p^{\text{SC}} \left[\frac{\begin{array}{c} 2q\,\text{csch}\left\{ 2q\left(\frac{\gamma^{\text{SC}}|_{\bar{H}=0}}{2R} \right) \right\} \\ - \tan\left\{ \left(\frac{\gamma^{\text{SC}}|_{\bar{H}=0}}{2R} \right) - s^{\text{LC}}(2R) \right\} \end{array}}{\begin{array}{c} 2q\,\text{csch}\left\{ 2q\left(\frac{\gamma^{\text{LC}}|_{\bar{H}=0}}{2R} \right) \right\} \\ - \tan\left\{ \left(\frac{\gamma^{\text{LC}}|_{\bar{H}=0}}{2R} \right) - s^{\text{LC}}(\gamma^{\text{LC}}|_{\bar{H}_{\text{min}}}) \right\} \end{array}} \right]$$
$$\times \left[\frac{\begin{array}{c} \tanh\left\{ q\left(\frac{\gamma^{\text{SC}}|_{\bar{H}=0}}{2R} \right) \right\} \\ \times \cos\left\{ \left(\frac{\gamma^{\text{SC}}|_{\bar{H}=0}}{2R} \right) - s^{\text{LC}}(2R) \right\} \end{array}}{\begin{array}{c} \tanh\left\{ q\left(\frac{\gamma^{\text{LC}}|_{\bar{H}=0}}{2R} \right) \right\} \\ \times \cos\left\{ \left(\frac{\gamma^{\text{LC}}|_{\bar{H}=0}}{2R} \right) - s^{\text{LC}}(\gamma^{\text{LC}}|_{\bar{H}_{\text{min}}}) \right\} \end{array}} \right] \tag{3.55}$$

and

$$\frac{\gamma^{\text{LC}}|_{\bar{H}=0}}{2R} \simeq \frac{3r \tan\left\{ s^{\text{LC}}(\gamma^{\text{LC}}|_{\bar{H}_{\text{min}}}) \right\} \left[9 \tan^2\left\{ s^{\text{LC}}(\gamma^{\text{LC}}|_{\bar{H}_{\text{min}}}) \right\} \right]^{1/2}}{3(2q^2 + 3) + 6 \tan^2\left\{ s^{\text{LC}}(\gamma^{\text{LC}}|_{\bar{H}_{\text{min}}}) \right\}} \tag{3.56}$$

where $q = 14.1819$ and $\gamma^{\text{LC}}|_{\bar{H}_{\min}}$ is solved for die and hydrostatic loading conditions, see Appendix C. Note that these modifications to the equations honor the conditions set for $\bar{H}^{\text{LC}}_{\min}$ in the ideally-plastic case. Simlar to the definition of $\bar{H}^{\text{LC}}_{\max}$ for the hardening cases, the definition of $\bar{H}^{\text{LC}}_{\min}$ is the minimum value of the low compressibility regime as there is no minimum in the cases with large hardening exponent.

In the low compressibility regime at the rigid-plastic limit for die and hydrostatic loading conditions, the value multiplied by ζ in parameter l, Eqn. (3.39), shows up at the limit. We exploit this finding to consider the dependency on hardening exponent in the low compressibility regime by including hardening exponent dependency in the form of an exponential function determined from calibration of FE data. Parameter l becomes

$$
\begin{aligned}
\ln(1 - l) &= \ln\left(\frac{1}{1 + 0.2335\mathrm{e}^{-0.5883/m}\zeta}\right) \\
&\implies l = 1 - \left(\frac{1}{1 + 0.2335\mathrm{e}^{-0.5883/m}\zeta}\right)
\end{aligned}
\tag{3.57}
$$

Adding multiplicative term $(\gamma/2R)^{1/2m}$ to the normalized contact pressure equation as done in the plastic regime, then the low compressibility regime equation at the rigid-plastic limit becomes

$$
\bar{H}^{\text{lc}} = \left[\bar{H}^{\text{LC}}_{\min} + \left(\frac{1 - \chi^{\text{LC}}|_{\bar{H}_{\min}}}{0.467\mathrm{e}^{-0.5883/m}}\right)\ln\left\{1 - \left(\frac{\chi^{\text{LC}} - \chi^{\text{LC}}|_{\bar{H}_{\min}}}{\chi^{\text{LC}}_{\text{zp}} - \chi^{\text{LC}}|_{\bar{H}_{\min}}}\right)^2\right\}\right]\left(\frac{\gamma}{2R}\right)^{\frac{1}{2m}}
\tag{3.58}
$$

where $\chi^{\text{LC}} = 1/\rho^{\text{LC}}_V = \left(V^{\text{LC}}_{\text{voro}}/V_{\text{particle}}\right)$ is the inverse of the relative density, $\chi^{\text{LC}}|_{\bar{H}_{\min}}$ is the value of χ at $\bar{H}^{\text{LC}}_{\min}$, and $\chi^{\text{LC}}_{\text{zp}}$ is the value of χ at the zero porosity limit. The elastic volumetric regime for die and hydrostatic loading conditions is kept the same as the rigid-plastic limit

from Eqn. (3.41). To conclude, the rigid-plastic semi-mechanistic contact law for contact pressure is the following

$$
\bar{H} =
\begin{cases}
\bar{H}^{\text{fp}} = \left[\bar{H}_{\text{max}} \mathrm{e}^{-1.748/m} - p^{\text{LC}} \tanh \left\{ q \left(\frac{\gamma}{2R} \right) \right\} \right. & \gamma \in \left(0, \gamma^{\text{LC}}|_{\bar{H}_{\text{min}}} \right] \\
\qquad \left. \times \cos \left\{ \left(\frac{\gamma}{2R} \right) - s^{\text{LC}} \right\} \right] \left(\frac{\gamma}{2R} \right)^{\frac{1}{2m}} & \text{LC} \to \{\text{SC}, \text{DC}, \text{HC}\} \\[2ex]
\bar{H}^{\text{lc}} = \left[\bar{H}_{\text{min}}^{\text{LC}} + \left(\frac{1 - \chi^{\text{LC}}|_{\bar{H}_{\text{min}}}}{0.467 \mathrm{e}^{0.5883/m}} \right) \right. & \gamma \in \left(\gamma^{\text{LC}}|_{\bar{H}_{\text{min}}}, \gamma_{\text{zp}}^{\text{LC}} \right] \\
\qquad \left. \times \ln \left\{ 1 - \left(\frac{\chi^{\text{LC}} - \chi^{\text{LC}}|_{\bar{H}_{\text{min}}}}{\chi_{\text{zp}}^{\text{LC}} - \chi^{\text{LC}}|_{\bar{H}_{\text{min}}}} \right)^{2} \right\} \right] \left(\frac{\gamma}{2R} \right)^{\frac{1}{2m}} & \text{LC} \to \{\text{DC}, \text{HC}\} \\[2ex]
\bar{H}^{\text{ev}} = \infty & \gamma \in \left(\gamma_{\text{zp}}^{\text{LC}}, \infty \right) \\
& \text{LC} \to \{\text{DC}, \text{HC}\}
\end{cases}
\tag{3.59}
$$

3.5   Rigid-plastic semi-mechanistic contact law verification

To verify the rigid-plastic semi-mechanistic contact law, the results for normalized contact pressure $(P/\kappa\pi a^{2})$, contact radius (a/R), and contact force $(P/\kappa R^{2})$ are compared with the FE simulations at five different values of hardening exponent. The results are presented in Figures 3.6, 3.7, and 3.8 for simple, die, and hydrostatic loading configurations. The contact law shows good prediction of the FE simulations for the full range of hardening exponent. Due to the rigid-plastic assumption, the contact law lacks in prediction of the normalized contact pressure at small deformations for particles with near perfect plasticity behavior.

(a)

(b)

(c)
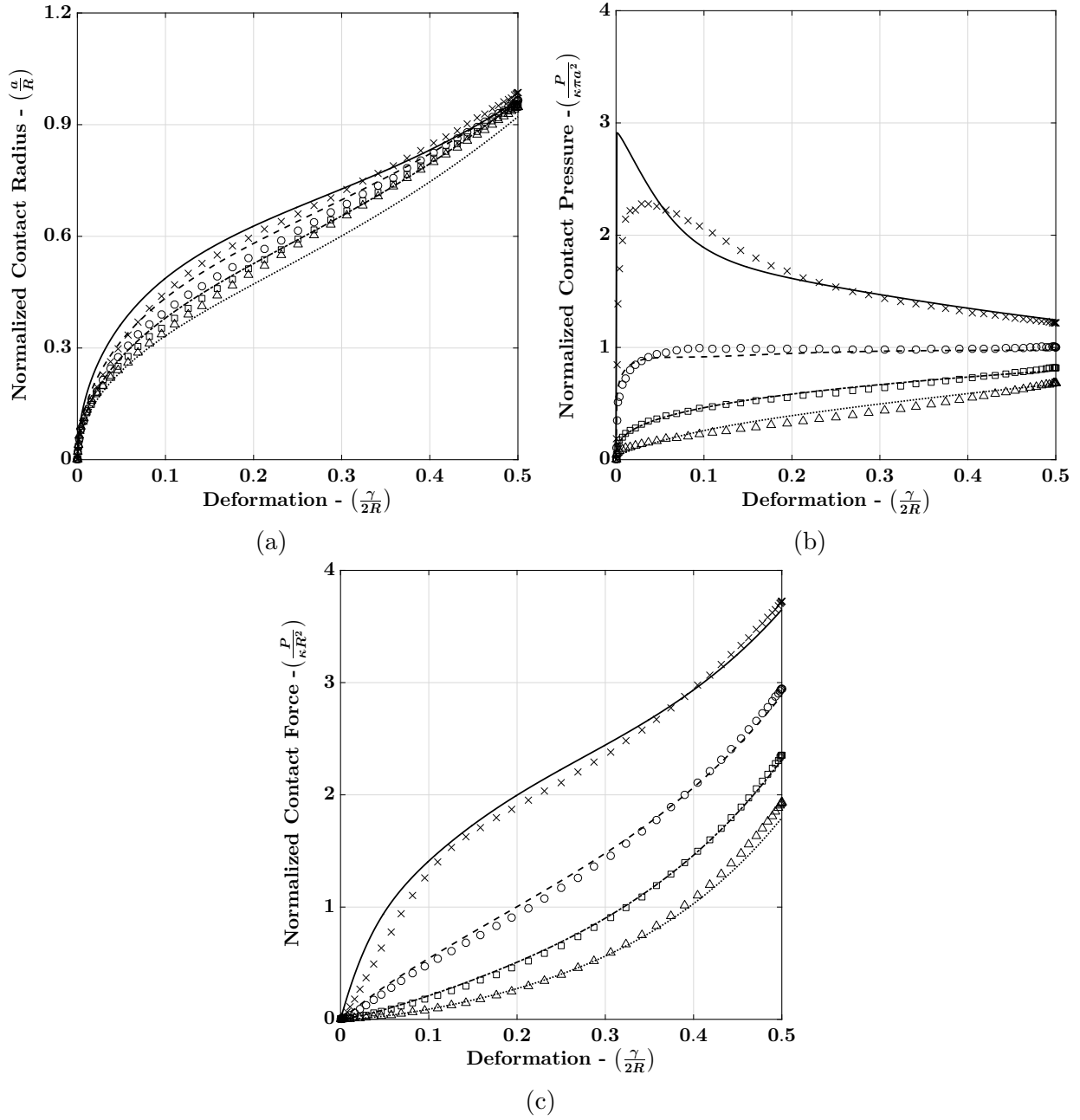
Fig.3.6. Semi-mechanistic contact law results for normalized contact radius 3.6a, contact pressure 3.6b, and contact force 3.6c for simple loading configuration. The figures show results for 4 values of hardening exponent: highest value, lowest value, and 2 values in between. FE data for $1/m = 0.01147$ are denoted by cross markers with corresponding contact law prediction by a solid lines. FE data for $1/m = 0.32677$ and $1/m = 0.66044$ are denoted by circle and square markers with the correspondig contact law predictions by dashed line and dash-dot lines. FE data for $1/m = 0.98094$ are denoted by triangle markers and the corresponding contact law predictions by a dotted line.

(a)

(b)

(c)
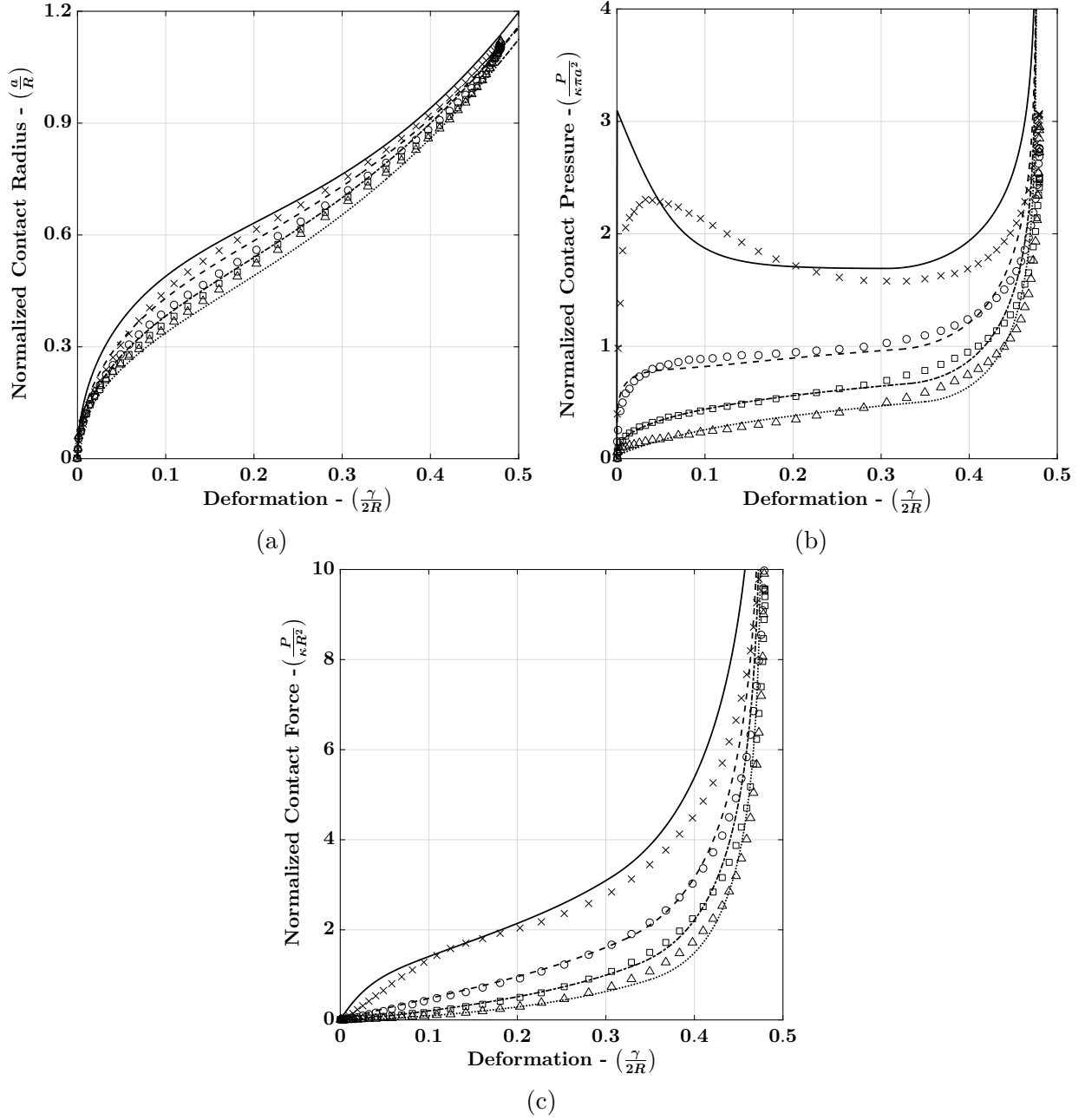
Fig.3.7. Semi-mechanistic contact law results for normalized contact radius 3.7a, contact pressure 3.7b, and contact force 3.7c for simple loading configuration. The figures show results for 4 values of hardening exponent: highest value, lowest value, and 2 values in between. FE data for $1/m = 3.64464\text{E} - 05$ are denoted by cross markers with corresponding contact law prediction by a solid lines. FE data for $1/m = 0.37109$ and $1/m = 68869$ are denoted by circle and square markers with the correspondig contact law predictions by dashed line and dash-dot lines. FE data for $1/m = 0.99996$ are denoted by triangle markers and the corresponding contact law predictions by a dotted line.

(a)

(b)

(c)
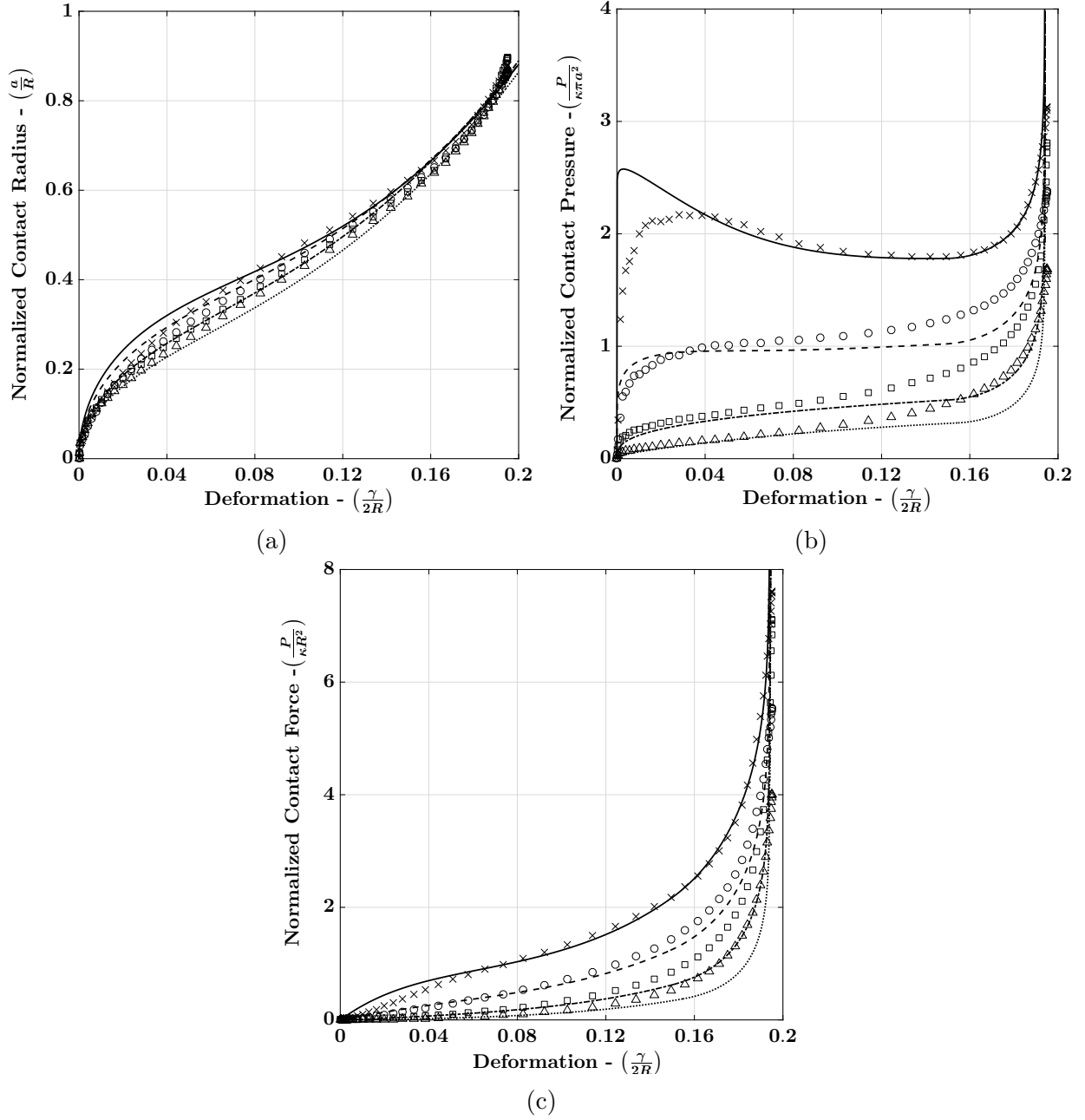
Fig.3.8. Semi-mechanistic contact law results for normalized contact radius 3.8a, contact pressure 3.8b, and contact force 3.8c for simple loading configuration. The figures show results for 4 values of hardening exponent: highest value, lowest value, and 2 values in between. FE data for $1/m = 0.03555$ are denoted by cross markers with corresponding contact law prediction by a solid lines. FE data for $1/m = 0.30431$ and $1/m = 0.66875$ are denoted by circle and square markers with the correspondig contact law predictions by dashed line and dash-dot lines. FE data for $1/m = 0.99223$ are denoted by triangle markers and the corresponding contact law predictions by a dotted line.
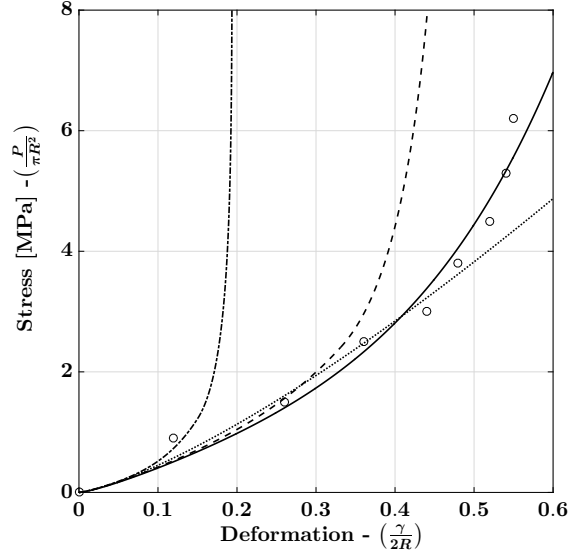
Fig.3.9. Calibration of MCC particles under large deformation simple compression. The experimental data points of MCC are denoted by circle markers and the corresponding calibrated results are denoted by a solid line. The estimated response under die and hydrostatic loading configuration are denoted by dashed line and dash-dot line. The response from the similarity contact law is denoted by a dotted line.
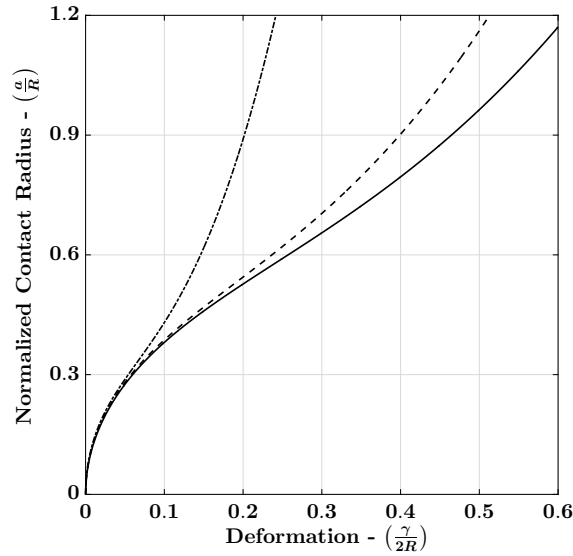
Fig.3.10. Estimated contact radius evolution of MCC particles under large deformation. Results for simple compression are denoted by a solid line. Results for die loading configuration are denoted by a dashed line. Results for hydrostatic loading configuration are denoted by a dash-dot line.

3.6 Calibration of micro-crystalline cellulose particles under large deformations

The rigid-plastic semi-mechanistic contact law is tested for experimental data from simple compression of micro-crystalline cellulose (Avicel PH-200) particles (Bommireddy et al., 2019). MCC particles with diameters ranging from $52.85 - 296.34$ μm were characterized experimentally through diameteric compression using a micro-compression tester. It was discovered that loading MCC under large deformation results in major permanent plastic deformation and apparent strain-hardening effects at different strain values. The response of MCC particles was calibrated using the contact law to determine the hardening properties. The hardening properties were then used to estimate the response of MCC particles under die and hydrostatic loading configurations. The results are presented in Figure 3.9.

The calibrated results showed that MCC particles have a hardening exponent $1/m = 0.6585$ and strength coefficient $\kappa = 6.0272$ MPa. A large value of hardening exponent is expected as MCC exhibit observable strain-hardening effects in compression testing. The response using similarity contact law with these hardening properties is also shown in Figure 3.9. It is evident that the similarity contact law is unable to capture the increase in pressure at large deformation, unlike our developed contact law.

Contact radius cannot be experimentally measured for MCC, however, the estimated hardening properties and the contact law can be used to predict contact radius evolution under simple, die, and hydrostatic loading configurations. These results are presented in Figure 3.10.

3.7 Conclusion

We built a semi-mechanistic contact law for rigid-plastic particles with power-law hardening deformed under simple compression, die compaction, and hydrostatic compaction. We began with the rigid-plastic limit of the semi-mechanistic contact law for elastic-ideally plastic particles which was modified to consider strain-hardening effects through exponential relationships with the hardening exponents. We utilized a total of 60 single-particle finite element simulations, 20 for each of the loading configurations (simple, die, and hydrostatic). In the contact radius formulation, the dependency on hardening exponent was adopted from

the three-term curvature-correction solution of the contact radius-displacement relationship from the similarity contact law. We observed that the third term in the contact radius equation required a different relationship with hardening exponent which was calibrated using the FE simulations. In the normalized contact pressure formulation, the plastic deformation regime and low compressibility regime for confined loading configurations were modified based on observation and analysis of the FE simulations. We verified the contact law by comparing the produced responses for normalized contact radius, contact pressure, and contact force with the FE simulations. Finally, we tested the contact law with experimental data of simple compression of micro-crystalline cellulose particles to determine hardening properties and estimated the response for die and hydrostating loading conditions.

4. SUMMARY AND FUTURE WORK

4.1 Summary

In this thesis, predictive contact law formulations for spherical particles with elastic-ideally plastic and plastic with power-law hardening behaviors under unconfined and confined loading configuration are presented. Verification of these contact law formulations is presented by comparing their results with finite element simulations. Calibration of experimental data from simple compression of micro-crystalline cellulose particles predicting hardening properties and stress response under alternate loading conditions is presented. Additionally, prediction of contact radius evolution for micro-crystalline cellulose particles using the contact law is presented.

In chapter 2, a semi-mechanistic contact formulation for material and loading condition dependent contact behavior of elastic-ideally plastic spherical particles is developed. Space-filling design with the fast-flexible filling algorithm is used to generate material properties for 51 finite element simulations. Formulation for contact radius is determined by applying the method of curvature-correction to the small-deformation similarity contact law to obtain three-terms nonlinear function of displacement. Formulation for normalized contact pressure is built as a piecewise differentiable function and is split into five deformation regimes. The results of the proposed contact law are verified by showing excellent agreement with the finite element simulations. Finally, small-deformation and large-deformation regimes are properly predicted for the lateral walls (secondary contacts) of die loading condition, creating a foundation for building a semi-mechanistic contact law for secondary contacts.

In chapter 3, the semi-mechanistic contact law for elastic-ideally plastic formulation is extended to consider power-law hardening behavior of plastic particles. The formulation begins by taking the rigid-plastic limit of the ideally plastic contact law, neglecting elastic and elastic-plastic regimes. Space-filling design with the fast-flexible filling algorithm is used to obtain hardening properties for 60 finite element simulations. The contact radius formulation is modified by adopting the dependency on hardening exponent from the curvature-correction solution of the similarity contact law. The contact pressure formulation is modified to consider hardening by analyzing the results of the finite element simulations. The contact law is verified

by showing good agreement with the finite element simulations. Finally, simple compression experimental data of micro-crystalline cellulose particles and the proposed contact law are used to estimate hardening properties, evolution of contact radius, and stress responses in die and hydrostatic loading configuration of micro-crystalline cellulose particles.

4.2 Future Work

The developed contact laws neglect gravitational forces, adhesion, friction, and alternate particle shapes. Gradually, these assumptions can be relaxed to produce a general contact law. Additionally, the contact laws assume independent contacts neglecting the nonlocal effects present in particle compaction. The next step is introducing nonlocal effects (see M. Gonzalez and Cuitiño, 2012, 2016 and Agarwal and Gonzalez, 2018) and relaxing the limitation on loading condition dependence in the contact laws as only three symmetric loading configurations are considered. A closed-form nonlocal contact formulations for plastically deforming particles will be developed which is capable of predict contact behavior under any general loading configuration.

REFERENCES

Agarwal, A., & Gonzalez, M. [Marcial]. (2018). Contact radius and curvature corrections to the nonlocal contact formulation accounting for multi-particle interactions in elastic confined granular systems. *International Journal of Engineering Science*, *133*, 26–46. doi:10.1016/j.ijengsci.2018.08.006

Agarwal, A., Shahin, M., & Gonzalez, M. (2021). Semi-mechanistic contact laws for large deformation unconfined and confined compression of elasto-plastic particles. *To be determined.*

Aurenhammer, F. (1987). Power diagrams: Properties, algorithms and applications. *SIAM Journal on Computing*, *16*(1), 78–96. doi:10.1137/0216006

Bakhshiani, A. [A.], Khoei, A. R., & Mofid, M. (2004). A density-dependent endochronic plasticity for powder compaction processes. *Computational Mechanics*, *34*(1), 53–66. doi:10.1007/s00466-004-0553-5

Bakhshiani, A., Khoei, A., & Mofid, M. (2002). An endochronic plasticity model for powder compaction processes. *Journal of Materials Processing Technology*, *125*, 138–143. doi:10.1016/S0924-0136(02)00360-6

Belheine, N., Plassiard, J.-P., Donzé, F.-V., Darve, F., & Seridi, A. (2009). Numerical simulation of drained triaxial test using 3D discrete element modeling. *Computers and Geotechnics*, *36*(1), 320–331. doi:10.1016/j.compgeo.2008.02.003

Biwa, S., & Storåkers, B. [Bertil]. (1995). An analysis of fully plastic Brinell indentation. *Journal of the Mechanics and Physics of Solids*, *43*(8), 1303–1333. doi:10.1016/0022-5096(95)00031-D

Bommireddy, Y., Agarwal, A., Yettella, V., Tomar, V., & Gonzalez, M. (2019). Loading-unloading contact law for micro-crystalline cellulose particles under large deformations. *Mechanics Research Communications*, *99*, 22–31. doi:https://doi.org/10.1016/j.mechrescom.2019.06.004

Chen, Y., Imbault, D., & Dorémus, P. (2007). Numerical simulation of cold compaction of 3D granular packings. In *Progress in powder metallurgy* (Vol. 534-536, pp. 301–304). Materials Science Forum. doi:10.4028/www.scientific.net/MSF.534-536.301

Chtourou, H., Guillot, M., & Gakwaya, A. (2002). Modeling of the metal powder compaction process using the cap model. Part I. Experimental material characterization and validation. *International Journal of Solids and Structures*, *39*(4), 1059–1075. doi:10.1016/S0020-7683(01)00255-4

Cundall, P. A., & Strack, O. D. L. (1979). A discrete numerical model for granular assemblies. *Géotechnique*, *29*(1), 47–65. doi:10.1680/geot.1979.29.1.47

Cunningham, J. C., Sinka, I. C., & Zavaliangos, A. (2004). Analysis of tablet compaction. I. Characterization of mechanical behavior of powder and powder/tooling friction. *Journal of Pharmaceutical Sciences*, *93*(8), 2022–2039. doi:10.1002/jps.20110

DiMaggio, F. L., & Sandler, I. S. (1971). Material model for granular soils. *Journal of the Engineering Mechanics Division, ASCE*, *97*(3), 935–951.

Dummit, D. S. (1991). Solving solvable quintics. *Mathematics of Computation*, *57*(195), 387–401. doi:10.1090/S0025-5718-1991-1079014-X

Frenning, G. (2013). Towards a mechanistic model for the interaction between plastically deforming particles under confined conditions: A numerical and analytical analysis. *Materials Letters*, *92*, 365–368. doi:10.1016/j.matlet.2012.10.118

Frenning, G. (2015). Towards a mechanistic contact model for elastoplastic particles at high relative densities. *Finite Elements in Analysis and Design*, *104*, 56–60. doi:10.1016/j.finel.2015.06.002

Gao, X.-L., Jing, X., & Subhash, G. (2006). Two new expanding cavity models for indentation deformations of elastic strain-hardening materials. *International Journal of Solids and Structures*, *43*(7), 2193–2208. doi:10.1016/j.ijsolstr.2005.03.062

Gellatly, B., & Finney, J. (1982). Characterisation of models of multicomponent amorphous metals: The radical alternative to the voronoi polyhedron. *Journal of Non Crystalline Solids*, *50*(3), 313–329. doi:https://doi.org/10.1016/0022-3093(82)90093-X

Ghaednia, H., Wang, X., Saha, S., Xu, Y., Sharma, A., & Jackson, R. L. (2017). A review of elastic-plastic contact mechanics. *Applied Mechanics Reviews*, *69:060804*(6). doi:10.1115/1.4038187

Gonzalez, M. [M.], & Cuitiño, A. M. (2012). A nonlocal contact formulation for confined granular systems. *Journal of the Mechanics and Physics of Solids*, *60*(2), 333–350. doi:10.1016/j.jmps.2011.10.004

Gonzalez, M. [M.], & Cuitiño, A. M. (2016). Microstructure evolution of compressible granular systems under large deformations. *Journal of the Mechanics and Physics of Solids*, *93*, 44–56. doi:10.1016/j.jmps.2016.03.024

Gonzalez, M. [Marcial]. (2019). Generalized loading-unloading contact laws for elasto-plastic spheres with bonding strength. *Journal of the Mechanics and Physics of Solids*, *122*, 633–656. doi:doi.org/10.1016/j.jmps.2018.09.023

Gonzalez, M. [Marcial], Poorsolhjouy, P., Thomas, A., Liu, J., & Balakrishnan, K. (2018). Statistical characterization of microstructure evolution during compaction of granular systems composed of spheres with hardening plastic behavior. *Mechanics Research Communications*, *92*, 131–136. doi:10.1016/j.mechrescom.2018.08.010

Han, L. H., Elliott, J. A., Bentham, A. C., Mills, A., Amidon, G. E., & Hancock, B. C. (2008). A modified Drucker-Prager Cap model for die compaction simulation of pharmaceutical powders. *International Journal of Solids and Structures*, *45*(10), 3088–3106. doi:10.1016/j.ijsolstr.2008.01.024

Hardy, C., Baronet, C. N., & Tordion, G. V. (1971). The elasto-plastic indentation of a half-space by a rigid sphere. *International Journal for Numerical Methods in Engineering*, *3*(4), 451–462. doi:10.1002/nme.1620030402

Harthong, B., Jérier, J.-F., Dorémus, P., Imbault, D., & Donzé, F.-V. (2009). Modeling of high-density compaction of granular materials by the discrete element method. *International Journal of Solids and Structures*, *46*(18), 3357–3364. doi:10.1016/j.ijsolstr.2009.05.008

Harthong, B., Jérier, J.-F., Richefeu, V., Chareyre, B., Dorémus, P., Imbault, D., & Donzé, F.-V. (2012). Contact impingement in packings of elastic–plastic spheres, application to powder compaction. *International Journal of Mechanical Sciences*, *61*(1), 32–43. doi:https://doi.org/10.1016/j.ijmecsci.2012.04.013

Hertz, H. (1882). Ueber die berührung fester elastischer körper. *Journal für die Reine und Angewandte Mathematik*, *92*, 156–171. Retrieved from http://eudml.org/doc/148490

Hill, R., Storåkers, B., & Zdunek, A. B. (1989). A theoretical study of the brinell hardness test. *Proceedings of the Royal Society of London. A. Mathematical and Physical Sciences*, *423*(1865), 301–330. doi:10.1098/rspa.1989.0056

Hollomon, J. H. (1945). Tensile deformation. *Transactions of American Institute of Mining and Metallurgical Engineers*, *162*, 268–290.

Jackson, R. L., & Green, I. (2005). A finite element study of elasto-plastic hemispherical contact against a rigid flat. *Journal of Tribology*, *127*(2), 343–354. doi:10.1115/1.1866166

Jackson, R. L., & Green, I. (2006). A statistical model of elasto-plastic asperity contact between rough surfaces. *Tribology International*, *39*(9), 906–914. doi:10.1016/j.triboint.2005.09.001

Jerier, J.-F., Hathong, B., Richefeu, V., Chareyre, B., Imbault, D., Donze, F.-V., & Doremus, P. (2011). Study of cold powder compaction by using the discrete element method. *Powder Technology*, *208*(2), 537–541. doi:10.1016/j.powtec.2010.08.056

SAS Institute Inc. (2018). JMP® Design of Experiments Guide. Cary, NC.

SAS Institute Inc. (2018). JMP®, Version 14.

Johnson, K. L. (1987). *Contact mechanics.* doi:10.1017/CBO9781139171731

Johnson, K. (1970). The correlation of indentation experiments. *Journal of the Mechanics and Physics of Solids*, *18*(2), 115–126. doi:10.1016/0022-5096(70)90029-3

Jonsson, H., Gråsjö, J., & Frenning, G. (2017). Mechanical behaviour of ideal elastic-plastic particles subjected to different triaxial loading conditions. *Powder Technology*, *315*, 347–355. doi:10.1016/j.powtec.2017.04.005

Joseph, V. R., Gul, E., & Ba, S. (2015). Maximum projection designs for computer experiments. *Biometrika*, *102*(2), 371–380. doi:10.1093/biomet/asv002

Khoei, A., Mofid, M., & Bakhshiani, A. (2002). Modelling of powder compaction process using an endochronic plasticity model. *Journal of Materials Processing Technology*, *130-131*, 175–180. AFDM 2002 S.I. doi:10.1016/S0924-0136(02)00708-2

Lekivetz, R., & Jones, B. (2015). Fast flexible space-filling designs for nonrectangular regions. *Quality and Reliability Engineering International*, *31*(5), 829–837.

Liu, L., Jia, Z., Ma, X., Fan, Y., Li, W., & Liu, H. (2014). A spherical cavity expansion model of large elastic deformation and its application to ballistic gelatin penetration problems. *International Journal of Impact Engineering*, *71*, 106–116. doi:10.1016/j.ijimpeng.2014.04.007

Ludwik, P. (1909). *Elemente der technologischen mechanik*. doi:10.1007/978-3-662-40293-1

Majmudar, T. S., & Behringer, R. P. (2005). Contact force measurements and stress-induced anisotropy in granular materials. *Nature*, *435*(7045), 1079. doi:10.1038/nature03805

Martin, C. [C.L.], & Bouvard, D. (2003). Study of the cold compaction of composite powders by the discrete element method. *Acta Materialia*, *51*(2), 373–386. doi:10.1016/S1359-6454(02)00402-0

Martin, C. [C.L], Bouvard, D., & Shima, S. (2003). Study of particle rearrangement during powder compaction by the discrete element method. *Journal of the Mechanics and Physics of Solids*, *51*(4), 667–693. doi:10.1016/S0022-5096(02)00101-1

Martin, C. L., Bouvard, D., & Delette, G. (2006). Discrete element simulations of the compaction of aggregated ceramic powders. *Journal of the American Ceramic Society*, *89*(11), 3379–3387. doi:10.1111/j.1551-2916.2006.01249.x

Mata, M., Casals, O., & Alcalá, J. (2006). The plastic zone size in indentation experiments: The analogy with the expansion of a spherical cavity. *International Journal of Solids and Structures*, *43*(20), 5994–6013. doi:10.1016/j.ijsolstr.2005.07.002

Wolfram Research, Inc. (2019). Champaign, IL.

Mesarovic, S. D., & Fleck, N. A. (2000). Frictionless indentation of dissimilar elastic-plastic spheres. *International Journal of Solids and Structures*, *37*(46), 7071–7091. doi:10.1016/S0020-7683(99)00328-5

Olsson, E. [E.], & Larsson, P.-L. [P.-L.]. (2016). A unified model for the contact behaviour between equal and dissimilar elastic–plastic spherical bodies. *International Journal of Solids and Structures*, *81*, 23–32. doi:10.1016/j.ijsolstr.2015.10.004

Olsson, E. [Erik], & Larsson, P.-L. (2013a). On force–displacement relations at contact between elastic–plastic adhesive bodies. *Journal of the Mechanics and Physics of Solids*, *61*(5), 1185–1201. doi:10.1016/j.jmps.2013.01.004

Olsson, E. [Erik], & Larsson, P.-L. (2013b). On the appropriate use of representative stress quantities at correlation of spherical contact problems. *Tribology Letters*, *50*, 221–232. doi:10.1007/s11249-013-0114-1

Poorsolhjouy, P., & Gonzalez, M. [Marcial]. (2018). Connecting discrete particle mechanics to continuum granular micromechanics: Anisotropic continuum properties under compaction. *Mechanics Research Communications*, *92*, 21–27. doi:10.1016/j.mechrescom.2018.07.001

Puri, V. M., Tripodi, M. A., Manbeck, H., & Messing, G. L. (1995). Constitutive model for dry cohesive powders with application to powder compaction. *KONA Powder and Particle Journal*, *13*, 135–150. doi:10.14356/kona.1995018

Quicksall, J. J., Jackson, R. L., & Green, I. (2004). Elasto-plastic hemispherical contact models for various mechanical properties. *Proceedings of the Institution of Mechanical Engineers, Part J: Journal of Engineering Tribology*, *218*(4), 313–322. doi:10.1243/1350650041762604

Rojek, J., Nosewicz, S., Jurczak, K., Chmielewski, M., Bochenek, K., & Pietrzak, K. (2016). Discrete element simulation of powder compaction in cold uniaxial pressing with low pressure. *Computational Particle Mechanics*, *3*(4), 513–524. doi:10.1007/s40571-015-0093-0

Santner, T. J., Williams, B. J., & Notz, W. I. (2013). *The design and analysis of computer experiments.* doi:10.1007/978-1-4757-3799-8

Shahin, M., Agarwal, A., & Gonzalez, M. (2021). Semi-mechanistic contact laws for large deformation unconfined and confined compression of plastic particles with power-law hardening. *To be determined.*

Sheng, Y., Lawrence, C. J., Briscoe, B. J., & Thornton, C. (2002). 3D DEM simulations of powder compaction. In *Discrete element methods: Numerical modeling of discontinua* (pp. 305–310). Geotechnical special publication. doi:10.1061/40647(259)54

Sinha, T., Curtis, J. S., Hancock, B. C., & Wassgren, C. (2010). A study on the sensitivity of Drucker-Prager Cap model parameters during the decompression phase of powder compaction simulations. *Powder Technology*, *198*(3), 315–324. doi:10.1016/j.powtec.2009.10.025

Sinka, I. C., Cunningham, J. C., & Zavaliangos, A. (2004). Analysis of tablet compaction. II. Finite element analysis of density distributions in convex tablets. *Journal of Pharmaceutical Sciences*, *93*(8), 2040–2053. doi:10.1002/jps.20111

Skrinjar, O., & Larsson, P.-L. [Per-Lennart]. (2004). On discrete element modelling of compaction of powders with size ratio. *Computational Materials Science*, *31*(1), 131–146. doi:10.1016/j.commatsci.2004.02.005

Storåkers, B. [B.], Biwa, S., & Larsson, P.-L. (1997). Similarity analysis of inelastic contact. *International Journal of Solids and Structures*, *34*(24), 3061–3083. doi:10.1016/S0020-7683(96)00176-X

Storåkers, B. [Bertil], & Larsson, P.-L. [Per-Lennart]. (1994). On brinell and boussinesq indentation of creeping solids. *Journal of the Mechanics and Physics of Solids*, *42*(2), 307–332. doi:10.1016/0022-5096(94)90012-4

Stronge, W. J. (2018). *Impact mechanics* (2nd). doi:10.1017/9781139050227

Studman, C. J., Moore, M. A., & Jones, S. E. (1977). On the correlation of indentation experiments. *Journal of Physics D: Applied Physics*, *10*(6), 949. doi:10.1088/0022-3727/10/6/019

Sun, X.-K., & Kim, K.-T. (1997). Simulation of cold die compaction densification behaviour of iron and copper powders by cam—clay model. *Powder Metallurgy*, *40*(3), 193–195. doi:10.1179/pom.1997.40.3.193

Sundstrom, B., & Fischmeister, H. F. (1973). Continuum mechanical model for hot and cold compaction. *Powder Metallurgy International*, *5*(4), 171–174.

Tabor, D. (1951). *The hardness of metals.* Clarendine Press, Oxford.

Trott, M., & Adamchik, V. (2001). Solving the qunitic with mathematica. Wolfram Library Archive, https://library.wolfram.com/infocenter/TechNotes/158. Accessed: 2020-03-13.

Tsigginos, C., Strong, J., & Zavaliangos, A. (2015). On the force-displacement law of contacts between spheres pressed to high relative densities. *International Journal of Solids and Structures*, *60-61*, 17–27. doi:10.1016/j.ijsolstr.2015.01.024

Ward Jr., J. H. (1963). Hierarchical grouping to optimize an objective function. *Journal of the American Statistical Association*, *58*(301), 236–244. doi:10.1080/01621459.1963.10500845

Yohannes, B., Gonzalez, M., Abebe, A., Sprockel, O., Nikfar, F., Kiang, S., & Cuitiño, A. M. (2016). Evolution of the microstructure during the process of consolidation and bonding in soft granular solids. *International Journal of Pharmaceutics*, *503*(1), 68–77. doi:10.1016/j.ijpharm.2016.02.032

Yohannes, B., Gonzalez, M., Abebe, A., Sprockel, O., Nikfar, F., Kiang, S., & Cuitiño, A. (2017). Discrete particle modeling and micromechanical characterization of bilayer tablet compaction. *International Journal of Pharmaceutics*, *529*(1), 597–607. doi:10.1016/j.ijpharm.2017.07.032

A. TABLE OF MECHANICAL PROPERTIES FOR ELASTIC-IDEALLY PLASTIC FINITE ELEMENT SIMULATIONS OBTAINED FROM THE SPACE-FILLING DESIGN

Table A.1. List of mechanical properties, arranged in the increasing order of the values of parameter $E/(1-\nu^2)\sigma_y$, and corresponding loading configurations obtained from the solution of the space-filling design problem.

Loading Condition	E (MPa)	ν	σ_y (MPa)	$E/(1-\nu^2)\sigma_y$
Simple	36961.79	0.4130	361.11	123.41
	20639.45	0.2993	148.54	152.62
	84752.72	0.3524	452.13	214.03
	172086.58	0.2115	472.34	381.38
	150500.27	0.4739	499.21	388.78
	101785.47	0.2643	225.81	484.61
	190003.52	0.2939	304.09	683.89
	75517.00	0.4019	92.86	969.91
	196617.68	0.4270	178.85	1344.55
	161529.29	0.2046	123.92	1360.40
	114577.91	0.3579	76.34	1721.55
	88565.10	0.4709	42.09	2703.51
	139990.73	0.2161	54.84	2677.75
	52841.85	0.2003	13.95	3945.19
	178811.38	0.2582	45.49	4211.18
	16555.89	0.4328	3.48	5852.93
	193549.09	0.4078	39.13	5933.40

Continued on next page

Table A.1 – *Continued from previous page*

Loading Condition	E (MPa)	ν	σ_y (MPa)	$E/(1-\nu^2)\sigma_y$
Die	49200.85	0.2251	317.80	163.08
	57221.17	0.3899	176.03	383.32
	146900.23	0.3247	424.97	386.40
	199028.86	0.4392	480.79	512.87
	180937.93	0.2001	341.00	552.74
	41573.92	0.3058	71.21	644.05
	141078.40	0.4640	234.62	766.29
	118951.98	0.2124	156.49	796.02
	184270.83	0.3440	199.86	1045.79
	199785.29	0.2841	129.76	1674.78
	21959.27	0.4749	16.08	1762.96
	190786.67	0.3829	78.68	2841.34
	5314.12	0.2933	2.01	2892.22
	78547.20	0.4264	28.38	3382.67
	160754.07	0.3213	37.41	4791.88
	198038.19	0.4772	51.91	4940.24
	110376.78	0.2204	23.42	4954.40
Hydro	2958.14	0.2099	26.39	117.24
	57840.71	0.4623	483.90	152.02
	65157.56	0.2831	283.64	249.74
	135501.57	0.3973	345.15	466.17
	194137.98	0.2418	413.75	498.35
	79402.31	0.4792	164.35	627.17
	198495.80	0.3652	256.71	892.25
	143839.36	0.3178	138.24	1157.36
	61598.96	0.3370	47.86	1451.86

Continued on next page

Table A.1 – *Continued from previous page*

Loading Condition	E (MPa)	ν	σ_y (MPa)	$E/(1-\nu^2)\sigma_y$
	187812.04	0.4654	114.89	2086.77
	131429.64	0.4187	70.02	2275.87
	197086.03	0.2014	92.22	2227.45
	174002.47	0.2976	61.27	3115.82
	123218.19	0.2344	35.71	3651.55
	34338.87	0.4100	11.20	3684.75
	95689.98	0.3607	19.17	5739.00
	147336.69	0.4576	31.83	5854.69

B. DERIVATION OF A CURVATURE CORRECTED SIMILARITY CONTACT LAW

Fig. B.1 shows a magnified view of the contact between two spherical particles of radii R_1 and R_2, representative strengths κ_1 and κ_2, and hardening exponent m being pressed along the normal direction. A cartesian coordinate system $\mathbf{x_i}$ ($i = 1, 2, 3$) and a polar coordinate system $(\mathbf{z}, \mathbf{r})$ is adopted, where $(\mathbf{z}, \mathbf{x_3})$ is the normal direction that is positive downwards, and $\mathbf{x_1} - \mathbf{x_2}$ is the plane of contact with $r = \sqrt{x_1^2 + x_2^2}$. According to (B. Storåkers et al., 1997), the boundary condition at the contact region is given by

$$u_3^{(1)} + u_3^{(2)} = \gamma - f_1(r) - f_2(r) \tag{B.1}$$

where $u_3^{(1)}$ and $u_3^{(2)}$ are the local displacements of any two corresponding surface points on the spheres 1 and 2 at a distance r from the contact center, γ is the total displacement of the centers of mass of the two spheres, and $f_1(r)$ and $f_2(r)$ are the profile functions of the undeformed contacting surfaces, given by $f_1(r) = R_1 - \sqrt{R_1^2 - r^2}$ and $f_2(r) = R_2 - \sqrt{R_2^2 - r^2}$. To obtain the similarity solution, the profile functions are approximated by the first term of their Taylor series expansion about $r = 0$, i.e.

$$R_l - \sqrt{R_l^2 - r^2} = \frac{r^2}{2R_l} + \mathcal{O}\left(\frac{a^4}{R_l^3}\right) \simeq \frac{r^2}{2R_l} \qquad (l = 1, 2) \tag{B.2}$$

To control the error associated with this approximation, the profile curvature can be corrected by including higher order terms of the Taylor expansion. We consider a two term expansion to approximate the profile functions as

$$\begin{aligned} R_l - \sqrt{R_l^2 - r^2} &= \frac{r^2}{2R_l} + \frac{r^4}{8R_l^3} + \mathcal{O}\left(\frac{a^6}{R_l^5}\right) \quad (l = 1, 2) \\ &\simeq \frac{r^2}{2R_l} + \frac{r^4}{8R_l^3} \end{aligned} \tag{B.3}$$

With this correction, the boundary condition given by Eq. (B.1) becomes

$$u_3^{(1)} + u_3^{(2)} = \gamma - \frac{r^2 \mathbb{A}}{2} - \frac{r^4 \mathbb{B}}{8} \tag{B.4}$$

where

$$\mathbb{A} = \frac{1}{R_1} + \frac{1}{R_2} \quad \text{and} \quad \mathbb{B} = \frac{1}{R_1^3} + \frac{1}{R_2^3}$$
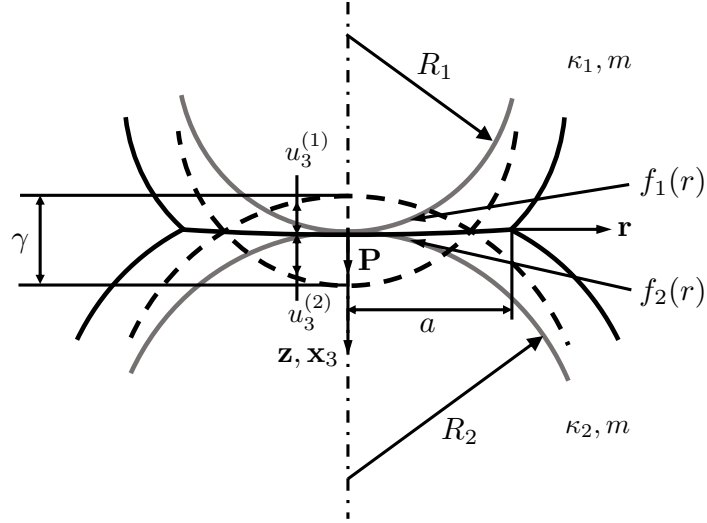
Fig.B.1. Schematic of the contact between two spherical particles of radii R_1 and R_2. The total displacement γ generates a radius of contact a between the two particles.

With consideration of small-strain kinematics, the field equations together with the boundary conditions can be summarized as:

$$\dot{\epsilon}_{ij}^{(l)} = \frac{1}{2} \left(\frac{\partial \dot{u}_i^{(l)}}{\partial x_j} + \frac{\partial \dot{u}_j^{(l)}}{\partial x_i} \right) \tag{B.5}$$

$$\frac{\partial \sigma_{ij}^{(l)}}{\partial x_j} = 0 \tag{B.6}$$

$$\sigma_e^{(l)} = \kappa_l \left(\epsilon_e^{(l)} \right)^{1/m} \tag{B.7}$$

$$\dot{u}_3^{(1)} + \dot{u}_3^{(2)} = \dot{\gamma}, \quad \sigma_{13}^{(l)} = \sigma_{23}^{(l)} = 0, \quad r \le a \tag{B.8}$$

$$\sigma_{13}^{(l)} = \sigma_{23}^{(l)} = \sigma_{33}^{(l)} = 0, \quad r > a \tag{B.9}$$

where $l = 1, 2$ and equations (B.5), (B.6) and (B.7) correspond to compatibility, equilibrium and constitutive law respectively.

The solution to this problem can be started by first taking a basic assumption that

$$\sigma_{ij}^{(l)}(x_k) = \sigma_{ij}^o(x_k) \qquad (l = 1, 2) \tag{B.10}$$

in order to ensure continuity of traction at the contact region. This in turn also satisfies the local equilibrium. In addition, scaling the displacements as

$$u_i^{(l)}(x_k) = \left(\frac{\bar{\kappa}}{\kappa_l}\right)^m u_i^o(x_k) \qquad (l = 1, 2) \tag{B.11}$$

where

$$\bar{\kappa} = \left(\frac{1}{\kappa_1^m} + \frac{1}{\kappa_2^m}\right)^{-1/m} \tag{B.12}$$

satisfies the complete field equations. With these assumptions, the boundary condition, Eq. (B.4) can be expressed as

$$u_3^o = \gamma - \frac{r^2 \mathbb{A}}{2} - \frac{r^4 \mathbb{B}}{8} \tag{B.13}$$

and the inhomogenous rate boundary conditions (Eqs. (B.8) and (B.9)) can be expressed as

$$\dot{u}_3^o = \dot{\gamma}, \quad \sigma_{13}^o = \sigma_{23}^o = 0, \quad r \le a \tag{B.14}$$

$$\sigma_{13}^o = \sigma_{23}^o = \sigma_{33}^o = 0, \quad r > a \tag{B.15}$$

The above moving boundary problem can now be converted to a stationary one by removing the dependence on indentation magnitude (contact radius) through appropriate transformations.

The kinematic variables, namely particle velocities and strain rates are transformed first and expressed as

$$x_k = a\tilde{x}_k \tag{B.16}$$

$$\dot{u}_i^o(x_k, a) = \dot{\gamma}\tilde{u}_i^o(\tilde{x}_k) \tag{B.17}$$

$$\dot{\epsilon}_{ij}^o(x_k, a) = \left(\frac{\dot{\gamma}}{a}\right)\tilde{\epsilon}_{ij}^o(\tilde{x}_k) \tag{B.18}$$

With the help of the above scaling, the inhomogeneous rate boundary condition, Eq. (B.14) now reduces to

$$\tilde{u}_3^o = 1, \quad \tilde{x}_3 = 0, \quad \tilde{r} \leq 1 \tag{B.19}$$

The vertical velocity field $\dot{u}_3^o$, when integrated over time, gives the total vertical displacement u_3^o which must satisfy the boundary condition given by Eq. (B.13). Using the transformation given by Eq. (B.17), we get

$$\int_0^t \tilde{u}_3^o \dot{\gamma} \, dt = \gamma - \frac{r^2 \mathbb{A}}{2} - \frac{r^4 \mathbb{B}}{8} \tag{B.20}$$

Variable transformation from t to a and the use of reduced rate boundary condition (Eq. (B.19)) yields a particular Volterra integral equation for $\gamma = \gamma(a)$ given by

$$\gamma(r) - \int_0^r \tilde{u}_3^o(r/s)\gamma(s) \, ds = \frac{r^2 \mathbb{A}}{2} + \frac{r^4 \mathbb{B}}{8}, \quad \gamma(a) = \frac{d\gamma}{da} \tag{B.21}$$

the solution to which is given as

$$\gamma(a) = \frac{1}{c^2}\left(\frac{a^2 \mathbb{A}}{2} + \frac{a^4 \mathbb{B}}{8}\right) \tag{B.22}$$

with the eigenfunction c^2 given by

$$c^2 = 1 - 2\int_1^\infty \frac{\tilde{u}_3^o}{\tilde{r}^3} \, d\tilde{r} \tag{B.23}$$

Eq. (B.22) is a quadratic equation in a^2, which can be solved algebraically to obtain the following $a - \gamma$ relationship

$$a = \left[\left(\frac{2}{\mathbb{B}} \right) \left\{ (\mathbb{A}^2 + 2\mathbb{B}c^2\gamma)^{1/2} - \mathbb{A} \right\} \right]^{1/2} \tag{B.24}$$

The above $a - \gamma$ relationship can be expressed as a Taylor series about $\gamma = 0$ as follows

$$a = \left(\frac{2c^2}{\mathbb{A}} \right)^{1/2} \gamma^{1/2} - \left(\frac{\mathbb{B}^{2/3}c^2}{2\mathbb{A}^{5/3}} \right)^{3/2} \gamma^{3/2} + \left(\frac{7^{2/5}\mathbb{B}^{4/5}c^2}{2^{9/5}\mathbb{A}^{9/5}} \right)^{5/2} \gamma^{5/2} + \mathcal{O}(\gamma^{7/2}) \tag{B.25}$$

where the first term of the series corresponds to the $a - \gamma$ relationship without curvature correction, proposed by (B. Storåkers et al., 1997), while the higher order terms correspond to the applied curvature correction. Equation (B.25) serves as the motivation behind formulation of the semi-mechanistic contact radius formulation proposed in Section 2.4 of this paper.

C. DERIVATION OF THE CONTACT DISPLACEMENT AT MINIMUM NORMALIZED HARDNESS FOR CONFINED PARTICLE LOADING CONDITIONS

According to the condition of minimum normalized hardness for confined loading configurations given by Eq. (2.28), expressions for various volume and surface quantities in the equation are provided in Table 2.3 for primary contacts under die and all contacts under hydrostatic loading configurations. The particle volume is given by $V_{\text{particle}} = (4/3)\pi R^3$ and the contact area is given by $S_{\text{contact}}^{\text{LC}} = \pi a^2$ where contact radius a is given by Eq. (2.13). We now proceed to derive Eq. (2.28) for the two confined loading cases in terms of the unknown contact displacement at the minimum.

Die Compaction (Primary Contacts):

$$
\begin{aligned}
\rho_V^{\text{DC,contact}} \times \rho_S^{\text{DC,contact}} &= \left(\frac{V_{\text{particle}}}{V_{\text{voro}}^{\text{DC}}}\right)\left(\frac{V_{\text{contact}}^{\text{DC}}}{V_{\text{voro}}^{\text{DC}}}\right)\left(\frac{S_{\text{contact}}^{\text{DC}}}{S_{\text{face}}^{\text{DC}}}\right) \\
&= \frac{\frac{4}{3}\pi R^3}{8R^2\left(R - \frac{\gamma}{2}\right)} \times \frac{\frac{4}{3}R^2\left(R - \frac{\gamma}{2}\right)}{8R^2\left(R - \frac{\gamma}{2}\right)} \times \frac{\pi a^2}{4R^2} \\
&= \frac{\pi^2 a^2}{144R\left(R - \frac{\gamma}{2}\right)} = \Gamma
\end{aligned}
\tag{C.1}
$$

Now, substituting a in terms of γ from Eq. (2.13) with $\mathbb{A} = 1/R_1 + 1/R_2 = 2/R$ and $\mathbb{B} = 1/R_1^3 + 1/R_2^3 = 2/R^3$, rearranging and simplifying the above equation, we finally get

$$
\begin{aligned}
&\left(\frac{\pi^2 \mathcal{D}_5^2}{32R^3}\right)\gamma^5 - \left(\frac{\pi^2 \mathcal{D}_3 \mathcal{D}_5}{8R^2}\right)\gamma^4 + \left(\frac{\pi^2 \mathcal{D}_3^2}{8R} + \frac{\pi^2 \mathcal{D}_1 \mathcal{D}_5}{4R}\right)\gamma^3 - \left(\frac{\pi^2 \mathcal{D}_1 \mathcal{D}_3}{2}\right)\gamma^2 \\
&+ \left(\frac{\pi^2 \mathcal{D}_1^2 R}{2} + 72R\Gamma\right)\gamma - 144R^2\Gamma = 0
\end{aligned}
\tag{C.2}
$$

Hydrostatic Compaction:

$$\rho_V^{\text{HC,contact}} \times \rho_S^{\text{HC,contact}} = \left(\frac{V_{\text{particle}}}{V_{\text{voro}}^{\text{HC}}}\right) \left(\frac{V_{\text{contact}}^{\text{HC}}}{V_{\text{voro}}^{\text{HC}}}\right) \left(\frac{S_{\text{contact}}^{\text{HC}}}{S_{\text{face}}^{\text{HC}}}\right)$$

$$= \frac{\frac{4}{3}\pi R^3}{8\left(R - \frac{\gamma}{2}\right)^3} \times \frac{\frac{4}{3}\left(R - \frac{\gamma}{2}\right)^3}{8\left(R - \frac{\gamma}{2}\right)^3} \times \frac{\pi a^2}{4\left(R - \frac{\gamma}{2}\right)^2} \qquad \text{(C.3)}$$

$$= \frac{\pi^2 R^3 a^2}{144\left(R - \frac{\gamma}{2}\right)^5} = \Gamma$$

Now, substituting a in terms of γ from Eq. (2.13) with $\mathbb{A} = 1/R_1 + 1/R_2 = 2/R$ and $\mathbb{B} = 1/R_1^3 + 1/R_2^3 = 2/R^3$, rearranging and simplifying the above equation, we finally get

$$\left(\frac{\pi^2 \mathcal{D}_5^2}{32} + \frac{9\Gamma}{2}\right)\gamma^5 - \left(\frac{\pi^2 \mathcal{D}_3 \mathcal{D}_5 R}{8} + 45R\Gamma\right)\gamma^4$$
$$+ \left(\frac{\pi^2 \mathcal{D}_3^2 R^2}{8} + \frac{\pi^2 \mathcal{D}_1 \mathcal{D}_5 R^2}{4} + 180R^2\Gamma\right)\gamma^3 - \left(\frac{\pi^2 \mathcal{D}_1 \mathcal{D}_3 R^3}{2} + 360R^3\Gamma\right)\gamma^2 \qquad \text{(C.4)}$$
$$+ \left(\frac{\pi^2 \mathcal{D}_1^2 R^4}{2} + 360R^4\Gamma\right)\gamma - 144R^5\Gamma = 0$$

The quintic equations in terms of the unknown γ, given by Eqs. (C.2) and (C.4), are solvable in radicals for given values of $\mathcal{D}_1$, $\mathcal{D}_3$, $\mathcal{D}_5$, R and Γ by the method proposed by (Dummit, 1991) (please ref. (Trott & Adamchik, 2001) for an implementation of the method in ("Wolfram Research, Inc", 2019)). Although the obtained quintic functions have five roots, there is only one positive real root, the proof of which is described below.

First, we immediately observe that the limits of the quintic functions in Eqs. (C.2) (denoted by $g(\gamma)$) and (C.4) (denoted by $h(\gamma)$) at $x \to -\infty$ and $x \to \infty$ are $-\infty$ and ∞ respectively, which means that the functions have at least one real root. Then, we calculate the derivative of the two polynomials with respect to γ to obtain

$$g(\gamma) = 72R\Gamma + \left[\frac{\pi^2}{32R^3}\left(\mathcal{D}_5\gamma^2 - 2R\mathcal{D}_3\gamma + 4R^2\mathcal{D}_1\right)\left(5\mathcal{D}_5\gamma^2 - 6R\mathcal{D}_3\gamma + 4R^2\mathcal{D}_1\right)\right] \qquad \text{(C.5)}$$

$$h(\gamma) = \frac{45}{2}\Gamma(\gamma - 2R)^4 + \left[\frac{\pi^2}{32}\left(\mathcal{D}_5\gamma^2 - 2R\mathcal{D}_3\gamma + 4R^2\mathcal{D}_1\right)\left(5\mathcal{D}_5\gamma^2 - 6R\mathcal{D}_3\gamma + 4R^2\mathcal{D}_1\right)\right] \quad \text{(C.6)}$$

If it is proved that $g(\gamma)$ and $h(\gamma)$ are positive in $\mathbb{R}$, then $g(\gamma)$ and $h(\gamma)$ are monotonic in $\mathbb{R}$, meaning that they have only one real root. Both $g(\gamma)$ and $h(\gamma)$ include an addition of two terms, where the first term in both functions is evidently positive, while the second term contains a product of two quadratic functions in γ, given by

$$F_1(\gamma) = \mathcal{D}_5\gamma^2 - 2R\mathcal{D}_3\gamma + 4R^2\mathcal{D}_1 \quad \text{(C.7)}$$

$$F_2(\gamma) = 5\mathcal{D}_5\gamma^2 - 6R\mathcal{D}_3\gamma + 4R^2\mathcal{D}_1 \quad \text{(C.8)}$$

If these quadratic functions are both positive or negative in $\mathbb{R}$, then the derivative functions $g(\gamma)$ and $h(\gamma)$ are positive in $\mathbb{R}$. We thus calculate the discriminants of the two quadratic functions, given by

$$\Delta_{F_1(\gamma)} = 4R^2(\mathcal{D}_3^2 - 4\mathcal{D}_1\mathcal{D}_5) \quad \text{(C.9)}$$

$$\Delta_{F_2(\gamma)} = 4R^2(9\mathcal{D}_3^2 - 20\mathcal{D}_1\mathcal{D}_5) \quad \text{(C.10)}$$

Fig. ?? presents the plots of $\Delta_{F_i(\gamma)}/4R^2$ (i = 1, 2) against material parameter λ for die (Fig. ??) and hydrostatic (Fig. ??) loading configurations. The plots evidently show that the discriminant values remain negative for $\lambda > 0$, with the limiting negative values at $\lambda \to \infty$ provided in Table C.1. This analysis proves that the quadratic functions $F_1(\gamma)$ and $F_2(\gamma)$ are positive in $\mathbb{R}$, and hence derivative functions $g(\gamma)$ and $h(\gamma)$ are monotonic in $\mathbb{R}$. Therefore, it is proved that the quintic functions $g(\gamma)$ and $h(\gamma)$ have only one real root.

Finally, we observe that $g(\gamma = 0) = -144R^2\Gamma$ and $h(\gamma = 0) = -144R^5\Gamma$. Hence, at $\gamma = 0$, both $g(\gamma)$ and $h(\gamma)$ are negative. Therefore, it is also proved that the real root of the qunitic functions is a positive value.

Table C.1. Limiting values of $\Delta_{F_i(\gamma)}/4R^2$ (i = 1, 2) at $\lambda \to \infty$ for die and hydrostatic loading configurations.

	DC	HC
$\lim\limits_{\lambda \to \infty} \Delta_{F_1(\gamma)}/4R^2$	-31.76	-300.49
$\lim\limits_{\lambda \to \infty} \Delta_{F_2(\gamma)}/4R^2$	-121.70	-1191.71

D. DETERMINATION OF THE INFLECTION POINT IN NORMALIZED HARDNESS VERSUS CONTACT DEFORMATION CURVES FOR PARTICLE COMPRESSION

From the observation of normalized hardness ($\bar{H}$) vs. contact deformation ($\gamma/2R$) curves obtained from FE simulations of simple (Fig. 2.9a), hydrostatic (Fig. 2.11a) and die (Fig. 2.10a) loading configurations, it is evident that the curves experience a change in curvature from *concave downward* to *concave upward* during the plastic deformation regime. The contact deformation at the inflection point, i.e., the point of curvature change, can be obtained by setting the second derivative of $\bar{H}$ with respect to contact deformation $\gamma/R_1 + R_2$ $(= \gamma/2R)$ equal to zero, and solving the resulting equation for the unknown deformation.

Using Eqs. (2.22) and (2.23) with $R_1 = R_2 = R$, the second derivative of $\bar{H}$ with respect to $\gamma/2R$ is given by

$$
\frac{\partial^2 \bar{H}}{\partial \left(\frac{\gamma}{2R}\right)^2} = -p^{\mathrm{LC}} r \left[\tanh(qx) \cos \left\{ x - s(\gamma^{\mathrm{LC}}|_{\bar{H}_{\min}}, q) \right\} \right]^r \left[4q^2 \mathrm{csch}^2(2qx) \left\{ r - \cosh(2qx) \right\} \right.
$$
$$
- 2qr \mathrm{csch}(qx) \mathrm{sech}(qx) \tan \left\{ x - s(\gamma^{\mathrm{LC}}|_{\bar{H}_{\min}}, q) \right\}
$$
$$
\left. + (r-1) \tan^2 \left\{ x - s(\gamma^{\mathrm{LC}}|_{\bar{H}_{\min}}, q) \right\} - 1 \right]
$$
(D.1)

where

$$
x = \frac{\gamma - \gamma|_{\bar{H}_{\max}}}{2R}
$$
(D.2)

Setting $\partial^2 \bar{H}/\partial \left(\frac{\gamma}{2R}\right)^2 = 0$ and simplifying the resulting equation, we get the following nonlinear equation in unknown x

$$
4q^2 \mathrm{csch}^2(2qx) \left\{ r - \cosh(2qx) \right\} + (r-1) \tan^2 \left\{ x - s(\gamma^{\mathrm{LC}}|_{\bar{H}_{\min}}, q) \right\}
$$
$$
- 2qr \, \mathrm{csch}(qx) \, \mathrm{sech}(qx) \tan \left\{ x - s(\gamma^{\mathrm{LC}}|_{\bar{H}_{\min}}, q) \right\} - 1 = 0
$$
(D.3)

Due to the high degree of non-linearity, the above equation cannot be solved analytically. However, an approximate solution for x can be obtained by reducing the equation to the first

term of its Taylor series expansion at $x = 0$ ($\gamma/2R = \gamma|_{\bar{H}_{\max}}/2R$). The resulting equation is given by

$$x^2 - \frac{6r \tan\left\{s(\gamma^{\mathrm{LC}}|_{\bar{H}_{\min}}, q)\right\}}{(2q^2 + 3)(2r + 1) + 3(r + 1)\tan^2\left\{s(\gamma^{\mathrm{LC}}|_{\bar{H}_{\min}}, q)\right\}} x$$
$$- \frac{3(r - 1)}{(2q^2 + 3)(2r + 1) + 3(r + 1)\tan^2\left\{s(\gamma^{\mathrm{LC}}|_{\bar{H}_{\min}}, q)\right\}} = 0 \tag{D.4}$$

The two solutions to the above equation are given by

$$x = \frac{3r \tan\left\{s(\gamma^{\mathrm{LC}}|_{\bar{H}_{\min}}, q)\right\} \pm \left[3(2q^2 + 3)(r - 1)(2r + 1) + 9(2r^2 - 1)\tan^2\left\{s(\gamma^{\mathrm{LC}}|_{\bar{H}_{\min}}, q)\right\}\right]^{1/2}}{(2q^2 + 3)(2r + 1) + 3(r + 1)\tan^2\left\{s(\gamma^{\mathrm{LC}}|_{\bar{H}_{\min}}, q)\right\}} \tag{D.5}$$

Among the two solutions, the solution involving a difference of the two terms in the numerator is always negative, since $(2r^2 - 1) \geq r^2$ and $3(2q^2 + 3)(r - 1)(2r + 1) > 0$. Therefore, x is given by the second, positive solution. Consequently, from Eq. (D.2), $\gamma/2R$ at the inflection point, denoted by $\gamma^{\mathrm{LC}}|_{\bar{H}=0}/2R$ is approximately given by

$$\frac{\gamma^{\mathrm{LC}}|_{\bar{H}=0}}{2R} \simeq \frac{\gamma|_{\bar{H}_{\max}}}{2R} + \frac{3r \tan\left\{s(\gamma^{\mathrm{LC}}|_{\bar{H}_{\min}}, q)\right\} + \left[3(2q^2 + 3)(r - 1)(2r + 1) + 9(2r^2 - 1)\tan^2\left\{s(\gamma^{\mathrm{LC}}|_{\bar{H}_{\min}}, q)\right\}\right]^{1/2}}{(2q^2 + 3)(2r + 1) + 3(r + 1)\tan^2\left\{s(\gamma^{\mathrm{LC}}|_{\bar{H}_{\min}}, q)\right\}} \tag{D.6}$$

E. TABLE OF HARDENING PROPERTIES FOR POWER-LAW HARDENING FINITE ELEMENT SIMULATIONS OBTAINED FROM THE SPACE-FILLING DESIGN

Table E.1. List of hardening properties arranged in increasing hardening exponent $1/m$

Loading Configuration	Hardening exponent $1/m$	Strength Coefficient κ (MPa)
Simple	0.01147	121.82
	0.06089	74.63
	0.12139	169.89
	0.13846	198.92
	0.15821	148.42
	0.25955	153.20
	0.32677	105.35
	0.34713	142.32
	0.39201	197.31
	0.48242	50.01
	0.55297	168.22
	0.57323	87.51
	0.64738	143.82
	0.66044	180.02
	0.74587	82.54
	0.78127	96.79
	0.80861	171.60
	0.89157	195.59
	0.96440	57.69
	0.98094	122.90

Continued on next page

129

Table E.1 - *Continued from previous page*

Loading Configuration	Hardening exponent $1/m$	Strength Coefficient κ (MPa)
Die	3.64464E-05	178.365
	0.13111	107.55
	0.17510	80.62
	0.19445	131.65
	0.20387	194.01
	0.21847	53.14
	0.24474	114.70
	0.28132	89.74
	0.37109	165.35
	0.50651	200.00
	0.51749	151.16
	0.53180	99.93
	0.58408	134.80
	0.60726	70.95
	0.68869	163.13
	0.76285	187.57
	0.82236	63.53
	0.84324	136.95
	0.95015	159.97
	0.99996	91.52
Hydro	0.03555	101.72
	0.05023	189.20
	0.08159	157.97
	0.10545	61.72
	0.23267	173.683
	0.30431	185.82

Continued on next page

Table E.1 - *Continued from previous page*

Loading Configuration	Hardening exponent $1/m$	Strength Coefficient κ (MPa)
	0.38207	65.80
	0.41687	93.75
	0.44579	124.48
	0.47216	182.98
	0.49573	138.75
	0.59780	190.80
	0.62424	117.38
	0.66875	54.55
	0.71140	127.75
	0.73621	155.10
	0.87834	111.59
	0.90813	146.76
	0.92019	76.88
	0.99223	176.68